Estimation of Ethanol Content and Control of Air-to-Fuel Ratio in Flex Fuel Vehicles

by

Kyung Ho Ahn

A dissertation submitted in partial fulfillment
of the requirements for the degree of
Doctor of Philosophy
(Mechanical Engineering)
in The University of Michigan
2011

Doctoral Committee:

Professor Anna G. Stefanopoulou, Chair
Professor Zoran S. Filipi
Professor Jing Sun
Professor Angela Violi
Mrdjan Janković, Ford Motor Company

© Kyung Ho Ahn

All Rights Reserved
2011

To Michael

Acknowledgments

During my graduate study at the University of Michigan, I have been helped and encouraged by many people in many different ways. Without the support, patience and guidance of the following people, this study would not have been completed. I owe my deepest gratitude to them.

- Professor Anna Stefanopoulou, my advisor, whose encouragement, supervision and support in every aspect enabled me to complete the graduate study
- Mrdjan Jankovic and Hakan Yilmaz, who provided valuable supports, comments and suggestions from industry
- Prof. Sun, Prof. Filipi, Prof. Violi and Prof. Sick, my other committee members, who contributed insightful comments and suggestions on this thesis
- Li, Alan, Julien and Donghoon, who have always heartily shared discussions with me and kindly helped me to do simulations and experiments.
- Kwanjeong Educational Foundation, who fully supported me financially during the early period of my graduate study.

Thank God for everything.

Table of Contents

List of Tables

Table

List of Figures

Figure

List of Appendices

Appendix

Abstract

Currently available flexible fuel vehicles (FFVs) can operate on a blend of gasoline and ethanol in any concentration of up to 85% ethanol (93% in Brazil). Accurate estimation of ethanol content is important to cope with potential problems caused by fuel variability. This thesis provides the first-ever comprehensive collection of models, model-based analysis and control design for ethanol estimation in FFVs. The common practice in ethanol content estimation exploits the differences in stoichiometric air-to-fuel ratios (SAFR) between gasoline and ethanol. In this approach, the online identification of SAFR depends on air and fuel metering during the closed-loop regulation of air-to-fuel ratio (AFR) to the stoichiometric value via the feedback of the exhaust gas oxygen sensor (EGO) measurement. In this thesis, first, we develop a simple phenomenological model of the AFR control process and a simple ethanol estimation law which represents the currently practiced system in FFVs. We then show that the SAFR-based ethanol estimation is sensitive to mass air flow (MAF) sensor drifts and/or fuel injector drifts. A physics-based control-oriented model for fuel puddle dynamics in port fuel injection (PFI) FFVs is then proposed. The transient fuel compensation (TFC) derived from this model allows faster ethanol estimation and improved AFR control. Since the conventional SAFR-based ethanol content estimation is sensitive to MAF sensor error, a method to correct MAF sensor error is next proposed. The correction is realized by using additional measurements of the intake manifold pressure to prevent mis-estimation of ethanol content during MAF sensor drifts. Finally, an integrated estimation scheme in direct injection (DI) FFVs is formulated. This process is able to estimate not only ethanol content but also fuel injector drift. Further, it exploits the difference in latent heat of vaporization (LHV) between gasoline and ethanol by using in-cylinder pressure measurements in addition to conventional SAFR-based estimation. The proposed algorithm and the associated parameter tuning method take the data-driven model errors into account. Feasibility of the integrated estimation scheme is validated by simulations and engine dynamometer tests.

Chapter 1
Introduction

1.1 Background

Petroleum-based fossil fuels are the dominant energy source for transportation. Recently, however, ethanol is being increasingly used as a fuel additive and is emerging as an alternative to carbon-neutral transportation. The advantage of ethanol, among others, is that it is a renewable fuel produced from biomass such as barley, corn, wheat, sugar cane, trees and grasses. As mandated by the US government Energy Policy Act of 2005 (EPACT2005), 7.5 billion gallons of bio-fuel will be produced in 2012 to reduce dependence on fossil fuels. Ethanol can be blended with conventional gasolines in varying percentages. The blend is denoted by the EXX nomenclature, where XX represents the volumetric percentage of ethanol in the blend. In the United States, E85 is commonly used as an alternative to normal gasoline fuel.[1] Vehicles that can operate on any blend of ethanol are called flex fuel vehicles (FFVs). These vehicles are designed to run on gasoline or a blend up to E85 in the U.S. and are currently being offered by many manufacturers.

The characteristics of ethanol differ from those of gasoline, as shown in Table. 1.1. results Various effects of ethanol fuel on a spark ignition engine, which are induced by the different properties from those of gasoline, are well reported in [42]. Engine modification, performance and emissions associated with ethanol fuel are also reported in [1, 15, 33]. Often ethanol fuel is associated with driveability and startability problems in cold and hot weather [17,56] and at high altitude [45]. Existing FFVs achieve lower range (miles driven per tank) when operating on higher ethanol content fuel due to its lower combustion heating value as compared to gasoline. However, as shown in Table. 1.1, ethanol has a higher octane ratio and therefore, a higher compression ratio and higher combustion efficiency can be obtained without knocking problems. Another advantage is that, the high vaporization heat can be used for charge cooling [16], which can further improve the knock

[1] In Brazil, however, a fuel blend called E100 is a blend of 93% ethanol and 7% of water [21]. Water-ethanol fuel blends are not considered in this research.

Table 1.1 Properties of ethanol compared with gasoline

Property	Gasoline	Ethanol
Research Octane Number (RON)	92	111
Density (kg/m^3)	747	789
Heat of combustion (MJ/kg)	42.4	26.8
Stoichiometric air-to-fuel ratio	14.6	9.0
Boiling point (°C)	20–300	78.5
Latent heat of vaporization (kJ/kg)	420	845
Dielectric constant	2.0	24.3

resistance and potentially fuel economy. Given the effect of fuel variation, FFVs embed engine calibration maps in their controllers and management systems to account for this variation. Calibration in an optimized flex-fuel strategy involves reliably estimating the ethanol percentage. Although this estimation is possible with the addition of a di-electric or electrochemical sensor in the fueling system, the reliability of these sensors has not yet been proven and the cost might be preventing their use. The principle of capacitance-based ethanol content sensing using the drastic difference in the dielectric constant between gasoline and ethanol in Table. 1.1 is found in [48,62]. Further, apart from the cost and reliability issues associated with such sensors, on-board diagnostic (OBD) requirements would require a redundant method for assessing the ethanol percent in order to diagnose the ethanol content sensor faults or degradation. Ethanol estimation should thus be established based on existing conventional sensors.

A potential method for ethanol content estimation involves measuring the air-to-fuel ratio (AFR) through an exhaust gas oxygen (EGO) sensor immediately after refueling is detected. This refueling event trigger is used to avoid misclassifying ethanol content variations as other faults such as actuator drifts or component aging. The ethanol detection period after the refueling event also needs to be as short as possible to reduce the probability of another (EGO or mass air flow (MAF) sensor, and/or injector) fault. Finally it is necessary to thoroughly understand and develop models to address how uncertainty, sensor and actuator drifts propagate through the detection process and affect the ethanol content estimation. Basic discussion regarding the robustness of the estimation using the exhaust oxygen sensor feedback is provided in [59].

Air-to-fuel ratio control around the stoichiometric ratio of a fuel blend is important as

well to meet stringent emission requirements for spark ignition (SI) engines. For a given air charge, the stoichiometric fuel is typically achieved by a combination of feedforward and feedback control on the fuel injection. Due to the long delays in the feedback loop, most engine controllers employ a feedforward fuel command which is primarily derived from the estimated cylinder air charge divided by the assumed stoichiometric ratio of the assumed fuel blend. The feedforward is usually designed to eliminate the transient effects of fuel puddle dynamics in port fuel injected (PFI) engines. Since the puddle dynamics and hence the fuel entering the cylinder depends on the ethanol content, transient fuel compensation (TFC) should be based on the gasoline-ethanol content and should retain the ability to be used in wide range of operating conditions. To this end, it is desirable to design a low-order model with a few tunable physical parameters.

A model for transient fuel compensation of gasoline in the form of a simple linear time invariant model for the fuel puddle dynamics was first introduced by Aquino in the early 1980s [8]. The four puddle model (FPM) was developed by Curtis *et al.* [19]. In this model, fuel films are distributed in four different locations in a PFI engine and the physics of fuel vaporization is well-exploited with use of multi-component fuel model. Locatelli *et al.* in [38] introduced a simple control-oriented wall-wetting model based on physical principles, where the port injected fuel dynamics is modeled as uniform droplet vaporization and exponential decay of the number of airborne droplets. An extended Kalman filter is used then to identify the physical parameters of the puddle dynamics for a gasoline fuel in [39]. In 2005, Batteh and Curtis introduced a fuel puddle dynamic model with alternative fuels [10]. They used the four puddle model, but unfortunately the fuel was modeled as a different combination of several fuel components for each fuel blend, i.e. indolene, E22 and E85 which does not allow a continuous variation within the E0-E85 range.

In many applications, controllers with fixed parameters may not maintain optimal performance over the life of products. Therefore, in the presence of system aging and faults, fault detection, isolation, and estimation (FDIE) plays a critical role in adaptive control algorithms [30, 31]. Specifically, FDIE during the mass air flow sensor bias/drift in conventional internal combustion engines can be performed as in [23, 36]. However, in FFVs, additional adaptation is required due to fuel blend changes between E0 and E85. Thus, conventional schemes cannot be directly applied. One way to cope with this increased dimension of unknown parameters is to use additional sensors suitable in various aspects such as cost, sensitivity, multi-purpose functionality and so on.

While the differences in stoichiometric air-to-fuel ratio (SAFR) and dielectric constant in Table. 1.1 are utilized in conventional ethanol content estimation and in capacitance-based ethanol concentration sensing, respectively, the drastic difference in latent heat of

vaporization (LHV) between gasoline and ethanol is a potential feature to realize ethanol content estimation independently of conventional methods. In direct injection engines, more cylinder charge cooling effects could be induced by ethanol fuel injection due to the higher latent heat of vaporization [16]. The charge cooling effects could be quantified if in-cylinder pressure measurement is available and could be correlated with the fuel ethanol content. The different charge cooling effects are characterized by vaporization process of different fuel blends. The heat exchange process associated with the charge cooling was modeled by Oliviero *et al.* in [44] using first principles for ethanol detection purpose. However, the model and the associated parameter tuning were not fully validated with a sufficient number of different operating conditions and it is doubtful if the model could actually alleviate calibration efforts with so many tuning parameters. The in-cylinder pressure drop induced by the charge cooling effects is a relatively tiny phenomenon compared with the in-cylinder pressure evolutions induced by engine cyclic strokes and other heat exchange processes. Therefore, it is difficult to model the process with first principles and to identify how different engine control variables may affect the charge cooling effects quantified by in-cylinder pressure measurements. There are few other modeling efforts associated with fuel vaporization [9, 60], but they do not fit to the charge cooling process for ethanol detection. It is desirable for the charge cooling effect or the in-cylinder pressure drop to be monotonically correlated with the ethanol content at certain operating conditions for ethanol detection purpose. However, it is known that mixing a small amount of a gasoline-ethanol blend with a large amount of gasoline can produce a mixture with a higher vapor pressure than either the gasoline or the blend alone [24, 25, 35]. This nonlinear vaporization characteristic could possibly result in undesired nonlinear correlations at certain conditions. This in turn can lead to potential difficulties in accurate estimation of ethanol content using the LHV-derived charge cooling feature.

1.2 Overview

In chapter 2, a simple ethanol estimation algorithm using an exhaust gas oxygen sensor is proposed, analyzed and discussed in light of AFR control. This law yields the estimated ethanol percentage in the fuel. Characteristics of the algorithm including sensitivity are quantified analytically and demonstrated via simulations [2]. Two main issues regarding the ethanol content estimation are then elucidated:

1. Transient AFR response constrains the ethanol content estimation gain, resulting in slow adaptation.

2. Mass air flow sensor error and/or fuel injection error propagate and influence the accuracy of the steady state ethanol estimation.

In chapter 3, we present a physics-based single puddle model using a multi-component model fuel for FFVs in order to design a transient fuel compensator which reduces transient AFR excursions caused by throttle modulation and consequently enables fast fuel adaptation [5]. The model is divided into two parts: a droplet evaporation model to generate the wall-impacting portion of the injected fuel and the single puddle vaporization model. To capture the characteristics of the physical vaporization process, a multi-component fuel model parameterized by the ethanol content is utilized. To verify the validity of the model, model simulation results are compared with the experimental data provided in [10] for E0, E22 and E85.

In chapter 4, a transient fuel compensator (TFC) using the proposed fuel puddle model is formulated. First, it is highlighted that it is far from straightforward to reproduce the X and τ pre-compensator of [40] based on the wall impacting factor X and the film vaporization time constant τ [8] because the multi-component model is nonlinear. Therefore, direct pole-zero cancelation similar to the pre-compensator is not possible. To address this difficulty, an approximation is used to invert the model to design a TFC. The approximation is demonstrated with a TFC simulation. The transient fuel compensator contributes to improvement in both performances of AFR control and ethanol content estimation. This performance enhancement is demonstrated by simulations. Robustness in AFR control and ethanol content estimation is elucidated as well by introducing modeling errors in the simulation of the fuel puddle observer used in TFC. Chapter 3 and 4 are based on our papers [5] and [3].

In chapter 5, a cylinder air flow estimation scheme is formulated. This scheme is able to compensate for the mass air flow (MAF) sensor drifts in the ethanol estimation by using additional manifold absolute pressure (MAP) measurements. The proposed scheme addresses the sensitivity of the ethanol estimation to MAF sensor error as shown in chapter 2. More reliable ethanol content estimation is realized here by performing enhanced cylinder air flow estimation via the MAF sensor error compensation. The proposed cylinder air flow estimation scheme is independent of the AFR-based ethanol content estimation loop. Hence, switching between the MAF sensor drift compensation and the ethanol content estimation is no longer necessary, and can eliminate potential estimation bias problems caused by the commonly used switching algorithms where two different estimations share one common exhaust gas oxygen sensor measurement. Simulations demonstrate air flow estimation with MAF sensor drift compensation using the MAP sensor and the ethanol

content estimation. Chapter 5 is based on our paper [4].

In chapter 6, an ethanol estimation scheme which is robust to fuel injector drifts in direct injection (DI) engines is presented. Since the AFR-based ethanol content estimation is sensitive to fuel injector error, an independent ethanol estimation scheme, which is insensitive to the fuel injector error, is proposed here. It is shown that under specially designed fuel injection sequences, the in-cylinder pressure measurements during the compression stroke capture the cylinder charge cooling effects of fuel with varying ethanol content. Specifically, the proposed methodology is based on the variations in the latent heats of vaporization (LHV) of different fuel types of varying ethanol content. The LHV-based detection feature is quantified experimentally by in-cylinder pressure measurements and is shown to be well-correlated with the ethanol content. The data driven model of the LHV-based detection feature is parameterized only by engine speed and load and the ethanol content but not parameterized by the fuel injection amount. Due to the closed-loop configuration of the AFR control around stoichiometry, the fuel injection amount is solely determined by the load (air amount) and the ethanol content even if there is fuel injection error. Hence, the LHV-based ethanol content estimation is insensitive to fuel injector drifts. However, the correlation between the LHV-based detection feature and the fuel ethanol content cannot be perfectly modeled, leading to various errors at various operating conditions. Therefore, the methodology employing the LHV-based detection feature is used to correct the AFR-based ethanol content estimation of chapter 2 in operating regions where certain confidence levels and accuracies are satisfied. This ethanol estimate correction enables more accurate fuel injector drift estimation after all in the switching configuration of ethanol content estimation and fuel injector drift estimation depending on the common EGO sensor measurement, when the ethanol content estimation is off and the fuel injector drift estimation is activated. The integrated AFR-based and LHV-based estimation algorithm is experimentally validated by an engine dynamometer test with the proposed algorithm implemented in the engine control unit (ECU) and the rapid prototyping. Chapter 6 is based on our papers [7], [6].

Fig. 1.1 summarizes the overview of this thesis.

1.3 Contributions

The work in this dissertation is summarized as follows.

- We analyzed the dynamic response of the ethanol content estimation using the stoichiometric air-to-fuel ratio (SAFR) features of different fuel types in the closed-loop

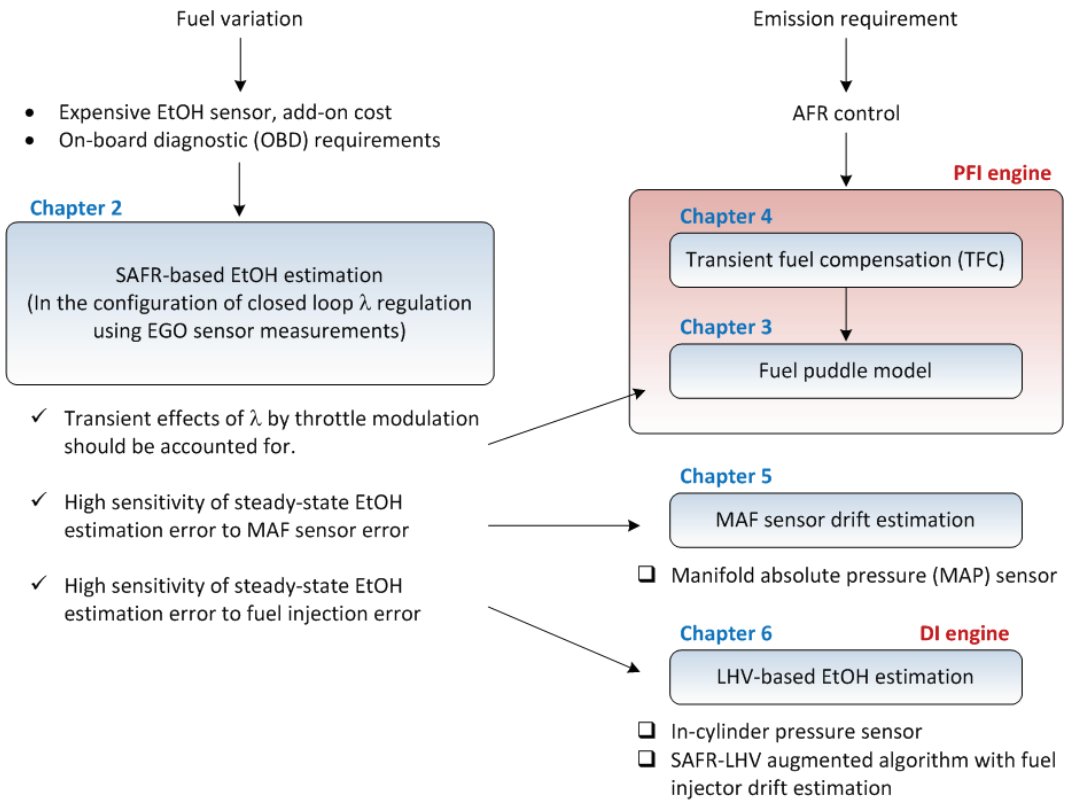

Figure 1.1 Overview of the thesis.

AFR control configuration with exhaust gas oxygen (EGO) sensor measurement in FFVs. We presented controller and estimator tuning with a phenomenological model and sensitivity analysis to various sensor, actuator, and model parameter errors.

- We developed and validated a physics-based control-oriented model of fuel puddle in port fuel injection (PFI) FFVs and designed a transient fuel compensation (TFC) algorithm using the model. The algorithm enables both better AFR control and faster estimation of ethanol content.
- We proposed a MAF sensor drift compensation algorithm using the MAP measurement for cylinder air charge estimation. The algorithm prevents severe misestimation of ethanol content in FFVs and obviates the need for other switching algorithms that depend on the detection of the fuel tank refueling event.
- We developed an ethanol content estimation scheme for direct injection (DI) FFVs based on the charge cooling features presented in [43] using the in-cylinder pressure measurements. The different charge cooling effects are associated with the different latent heats of vaporization (LHV) for different fuel types. An integrated algorithm

combining the LHV-based ethanol estimation scheme with the conventional SAFR-based estimation scheme was also developed. The fusion of the two estimation schemes addresses practical feasibility issues associated with LHV-based modeling error and the sensitivity of the SAFR-based estimation to fuel injector drifts. Experiments show that this integrated algorithm is indeed able to estimate fuel injector drift and accordingly detect a fuel injector fault.

Chapter 2
Estimation of Ethanol Content

2.1 Introduction

The characteristics of ethanol differ from those of gasoline, as shown in Table. 1.1. The Various effects of ethanol fuel on a spark ignition engine are well reported in [42]. Engine modification, performance and emissions associated with ethanol fuel are also reported in [1]. Often ethanol fuel is associated with driveability and startability problems in cold and hot weather [17,56] and at high altitude [45]. When operating on higher ethanol content fuel, current FFVs achieve lower range (miles driven per tank) due to the lower combustion heating value as compared to gasoline. However, as shown in Table. 1.1, ethanol has a higher octane ratio and therefore, a higher compression ratio, which lead to the advantage of higher combustion efficiency without knocking problems. Another advantage is that, the high vaporization heat can be used for charge cooling [16], thus further improving knock resistance and potentially fuel economy.

Given the effects of fuel variation, FFVs should embed engine calibration maps in their controllers and management systems to account for the variations. To accomplish this, the first task in a flex-fuel strategy is to estimate reliably the ethanol percentage. Although this estimation is possible with the addition of a di-electric or electrochemical sensor in the fueling system, the reliability and the cost of these sensors likely prevent their use. Apart from the cost and reliability issues associated with such sensors, on-board diagnostic (OBD) requirements would require a redundant method independent of the fuel sensor to assess the ethanol percent in order to diagnose the ethanol content sensor faults or degradation.

Ethanol estimation should thus be established based on existing conventional sensors if possible. Currently the ethanol content estimation depends on the AFR measurement through an exhaust gas oxygen (EGO) sensor immediately after refueling is detected. This refueling event trigger is used to avoid misclassifying ethanol content variations as other faults such as actuator drifts or component aging. The ethanol detection period also needs to be as short as possible to reduce the probability of the car stopping and cooling down

without a correct ethanol estimation having been established . This possibility is undesirable since a cold start depends heavily on correct ethanol estimation. Finally it is necessary to thoroughly understand and develop models to address how uncertainty, sensor and actuator drifts propagate through the detection process and affect the ethanol content estimation. Basic discussion regarding the robustness of the estimation using the exhaust oxygen sensor feedback is provided in [59].

In this chapter, a simple stoichiometric AFR estimation law using the exhaust gas oxygen sensor is proposed, analyzed and discussed in light of AFR control. This law yields the estimated ethanol percentage in the fuel. Characteristics of the algorithm including sensitivity are quantified via simulations. Two main issues regarding the ethanol content estimation are then elucidated:

1. Transient AFR response restricts increasing ethanol content estimation gain, hence resulting in slow adaptation.
2. Mass air flow sensor error and/or fuel injection error result in steady state ethanol content estimation error with high sensitivity.

2.2 Ethanol Content Estimation

Air-to-fuel ratio control around the stoichiometric ratio of a fuel blend is important to meet stringent emission requirements for spark ignition (SI) engines. For a given air charge, the stoichiometric fuel is typically achieved by a combination of feedforward and feedback control on the fuel injection. The feedback controller is based on the measured ratio (λ) of the actual air-to-fuel ratio (AFR) to the stoichiometric ratio (AFR_s) through an exhaust gas oxygen sensor. The λ ratio is compared to $\lambda^{des} = 1$ and the error is used by a proportional integral (PI) controller to adjust the feedback fuel command. Due to the long delays in the feedback loop, most engine controllers employ a feedforward fuel command which is primarily derived from the estimated cylinder air charge divided by the assumed stoichiometric ratio of the assumed fuel blend. Furthermore, the feedforward is usually designed to eliminate the transient effects of fuel puddle dynamics in port fuel injected (PFI) engines. Since the puddle dynamics is dependent on the ethanol content, estimation of ethanol content may also be used for the transient fuel compensation (TFC). A model of fuel puddle dynamics with alternative fuels is discussed in [10] where a fuel blend is modeled as a certain combination of organic compounds that mimics the distillation behavior of an actual fuel.

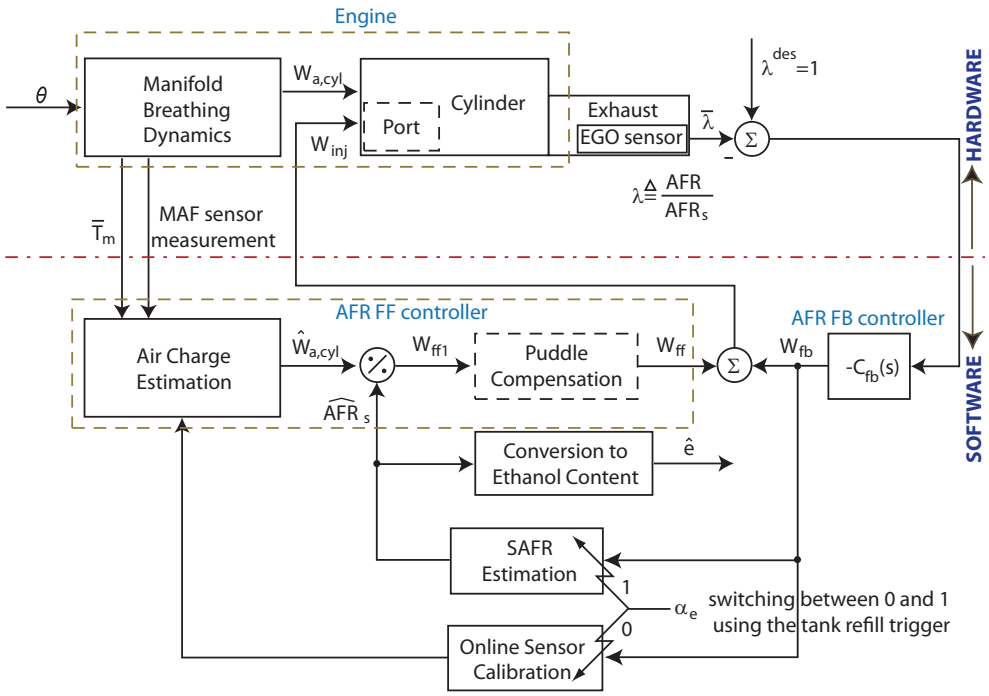

Figure 2.1 Block diagram of AFR control

When the assumed stoichiometric ratio is correct, and there are neither errors in the air charge and fuel puddle dynamics estimation, nor drifts or faults in the injector, the feedforward fuel command is then perfect and the feedback fuel compensation should be zero. An estimation algorithm can utilize a nonzero feedback fuel command to adapt and improve the feedforward fuel compensator so that the feedback converges back to its nominal zero value. Ideally, the adaptation will address the core problem in the feedforward path. In the case of an FFV, the adaptation of the assumed stoichiometric ratio or the adaptation for a miscalibrated air charge estimation cannot coexist. Namely, the engine management system will have to assume that the error arises from changes in the fuel blend or from component (sensor, actuator) aging.

Fig. 2.1 shows the block diagram of AFR control with flex fuel, where the diagram specifically corresponds to the configuration that the feedback control signal is used for the air path adaptation (online mass air flow (MAF) sensor calibration) against the MAF sensor drifts when the stoichiometric air-to-fuel ratio (SAFR) estimation, i.e., ethanol content estimation is deactivated. Let e denote the volume fraction of ethanol in gasoline-ethanol blend. And let e_m denote the mass fraction of ethanol. Then, e_m is expressed as:

$$e_m = \frac{e\rho_{eth}}{e\rho_{eth} + (1-e)\rho_{gsl}} = \frac{e}{e + (1-e)\rho_{gsl}/\rho_{eth}} = \frac{e}{e + (1-e)/1.056}, \tag{2.1}$$

where ρ_{eth} and ρ_{gsl} denote the density of ethanol and the density of gasoline respectively. Now, the stoichiometric air-to-fuel ratio for flex fuel is expressed as:

$$AFR_s = 9 \times e_m + 14.6 \times (1 - e_m). \tag{2.2}$$

Hence, if we want to calculate the volume fraction of ethanol, e, from an estimated stoichiometric AFR, $\widehat{AFR}_s$, the following equations are utilized:

$$\widehat{e}_m = \frac{14.6 - \widehat{AFR}_s}{5.6}, \tag{2.3}$$

$$\widehat{e} = \frac{\widehat{e}_m}{1.056 - 0.056 \times \widehat{e}_m}. \tag{2.4}$$

A simple adaptation law of ethanol content estimation can be expressed by the following update law of the estimated stoichiometric AFR, $\widehat{AFR}_s$, using the feedback fuel correction signal, W_{fb}. The adaptation law is triggered after a tank refill event is detected and the flag α_e is set to 1, otherwise ($\alpha_e = 0$) another adaptation loop is typically activated that corrects the engine maps, such as volumetric efficiency used for the air charge estimation, or drifts in sensors and actuators:

$$\dot{\widehat{AFR}}_s = \gamma_e (0 - W_{fb}) \alpha_e. \tag{2.5}$$

Assuming that there is a pre-defined logic associated with the activation/deactivation of the ethanol content estimation, i.e., setting α_e using the tank refill trigger, the feedforward fuel command is then determined as:

$$W_{ff1} = \widehat{W}_{a,cyl} / \widehat{AFR}_s, \tag{2.6}$$

where $\widehat{W}_{a,cyl}$ is the estimated air flow into the cylinder.

To analyze the dynamic and steady state ethanol estimation error using (2.3)-(2.6) for the ethanol estimation given the feedback control command W_{fb} in (2.5) and the feedforward fuel command W_{ff1}, which depends on the estimated cylinder air flow $\widehat{W}_{a,cyl}$ in (2.6), we employ a simple engine model in section 2.3 and a simple AFR controller in 2.4.

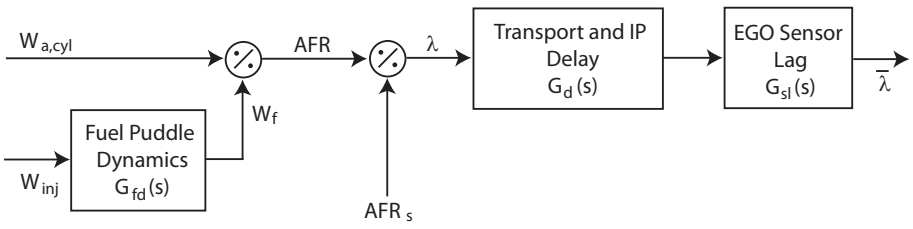

Figure 2.2 Path from injector command to EGO sensor output

2.3 Engine Dynamics

A simple dynamical model of the air and fuel engine behavior is described below.

Fig. 2.2 shows the process considered once the fuel command W_{inj} is issued to the injectors all the way until λ is measured by the EGO sensor. We assume that the fuel puddle dynamic behavior is expressed as a linear time invariant (LTI) transfer function in the neighborhood of the chosen equilibrium point given by:

$$G_{fd}(s) = \frac{(1-X)\tau s + 1}{\tau s + 1}, \tag{2.7}$$

where X and τ denote the wall-impacting portion of the injected fuel and the vaporization time constant of the fuel puddle, respectively [8]. The cylinder input λ is by definition:

$$\lambda \triangleq \left(\frac{W_{a,cyl}}{W_f}\right) / AFR_s, \tag{2.8}$$

where $W_{a,cyl}$ denotes the air flow rate into the cylinder, W_f the fuel flow rate into the cylinder and AFR_s the stoichiometric air-to-fuel ratio. The quantity W_f is the fuel flow rate that effectively enters the cylinder related with the fuel injection rate, W_{inj}, by the fuel dynamics such that

$$W_f = G_{fd}(s) W_{inj}. \tag{2.9}$$

Let the Padé approximation of the transport and induction-to-power (IP) delay from the cylinder input λ to the exhaust λ be:

$$G_d(s) = \frac{1 - \frac{\tau_d}{2}s}{1 + \frac{\tau_d}{2}s}, \tag{2.10}$$

where τ_d is the delay time which depends on engine speed. And let us express the λ sensor lag as:

$$G_{sl}(s) = \frac{1}{1 + \tau_s s}, \tag{2.11}$$

where τ_s is the time constant which lumps the chemical, the electrical and the communication delays of the EGO sensor dynamics. The measured λ is then expressed as:

$$\bar{\lambda} = G_{sl}(s)G_d(s)\lambda. \tag{2.12}$$

2.4 AFR Control and SAFR Estimation Law

The control law without the feedforward compensation of the fuel dynamics ($W_{ff} \equiv W_{ff1}$) can be summarized as:

$$W_{inj} = W_{ff} + W_{fb}, \tag{2.13}$$
$$W_{ff} = \widehat{W}_{a,cyl}/\widehat{AFR}_s, \tag{2.14}$$
$$W_{fb} = -C_{fb}(s)(1-\bar{\lambda}), \tag{2.15}$$

where the feedback controller, $C_{fb}(s)$, is assumed to be a PI controller:

$$C_{fb}(s) = k_{PI}\frac{\tau_{PI}s+1}{s}. \tag{2.16}$$

When the ethanol content estimation is activated, i.e., $\alpha_e = 1$, the SAFR estimation law in (2.5) is expressed as:

$$\dot{\widehat{AFR}}_s = -\gamma_e W_{fb}. \tag{2.17}$$

If the assumed SAFR is larger than the actual, i.e., smaller ethanol content is assumed, the feedforward signal W_{ff} in (2.14) will be less than the desired. The feedback W_{fb} will then compensate for the shortage as the measurement $\bar{\lambda}$ should detect the lean condition ($\bar{\lambda} > 1$) in (2.15). The estimated SAFR, $\widehat{AFR}_s$, will then decrease by integrating the positive feedback signal W_{fb} in (2.17), hence increasing the ethanol content estimate. By this way, the estimated ethanol content will eventually converge to the actual value in steady state.

2.5 Closed-Loop Dynamics

Let us consider the linearized dynamics of the system with the simple AFR estimation law about a fixed stoichiometry and a fixed cylinder air flow associated with a specific load (manifold pressure) and engine speed. Note that here the air flow rate into the cylinder is assumed to be exactly estimated, $\widehat{W}_{a,cyl} \equiv W_{a,cyl}$, for the PI gain tuning analysis in C_{fb}

(2.16). The closed-loop system is expressed by the set of equations of (2.8), (2.9), (2.12) and (2.13)-(2.17). We use the superscript ^{0} to express a nominal value at equilibrium and use δ to express the deviation from the equilibrium. Equation (2.8) is then linearized into:

$$\begin{aligned}\delta\lambda &= \frac{1}{W^0_{a,cyl}}\delta W_{a,cyl} - \frac{1}{W^0_f}\delta W_f - \frac{1}{AFR^0_s}\delta AFR_s \\ &= \frac{1}{W^0_{a,cyl}}\delta W_{a,cyl} - \frac{1}{W^0_f}G_{fd}(s)\delta W_{inj} - \frac{1}{AFR^0_s}\delta AFR_s. \end{aligned} \tag{2.18}$$

From (2.13)-(2.17), we obtain:

$$\delta W_{inj} = \delta W_{ff} + \delta W_{fb}, \tag{2.19}$$

$$\delta W_{ff} = \frac{1}{AFR^0_s}\delta W_{a,cyl} - \frac{W^0_f}{AFR^0_s}\delta\widehat{AFR}_s, \tag{2.20}$$

$$\delta W_{fb} = C_{fb}(s)\delta\bar{\lambda}, \tag{2.21}$$

$$\delta\widehat{AFR}_s = -\frac{\gamma_e}{s}\delta W_{fb}. \tag{2.22}$$

Using (2.21), (2.22) and (2.12), δW_{ff} in (2.20) is expressed as:

$$\delta W_{ff} = \frac{1}{AFR^0_s}\delta W_{a,cyl} + \gamma_e\frac{W^0_f}{AFR^0_s}\cdot\frac{1}{s}\cdot C_{fb}(s)G_{sl}(s)G_d(s)\delta\lambda. \tag{2.23}$$

The total injection signal is then expressed as:

$$\delta W_{inj} = \frac{1}{AFR^0_s}\delta W_{a,cyl} + \left(\gamma_e\frac{W^0_f}{AFR^0_s}\cdot\frac{1}{s}+1\right)C_{fb}(s)G_{sl}(s)G_d(s)\delta\lambda. \tag{2.24}$$

Equation (2.24) is substituted into the equation (2.18) to obtain the closed loop transfer functions.

$$R(s)\delta\lambda = \frac{1}{W^0_{a,cyl}}\left(1-G_{fd}(s)\right)\delta W_{a,cyl} - \frac{1}{AFR^0_s}\delta AFR_s,$$

where $R(s)$ is defined as:

$$R(s) \triangleq 1 + \frac{1}{W^0_f}\left(\gamma_e\frac{W^0_f}{AFR^0_s}\cdot\frac{1}{s}+1\right)G(s)C_{fb}(s), \tag{2.25}$$

with $G(s) \triangleq G_{fd}(s)G_d(s)G_{sl}(s)$. The linearized disturbance input–output relation is expressed as the following closed-loop system:

$$\delta\lambda = T_1(s)\delta W_{a,cyl} + T_2(s)\delta AFR_s, \tag{2.26}$$

where the closed-loop transfer functions, $T_1(s)$ and $T_2(s)$, are defined as:

$$T_1(s) \triangleq \frac{1}{W^0_{a,cyl}} \cdot \frac{1 - G_{fd}(s)}{R(s)}, \tag{2.27}$$

$$T_2(s) \triangleq -\frac{1}{AFR^0_s} \cdot \frac{1}{R(s)}. \tag{2.28}$$

The closed-loop transfer functions are expressed as:

$$T_1(s) = \frac{1}{W^0_{a,cyl}} \cdot \frac{X\tau s^3(1+\tau_s s)(1+\frac{\tau_d}{2}s)}{D(s)}, \tag{2.29}$$

$$T_2(s) = -\frac{1}{AFR^0_s} \cdot \frac{s^2(1+\tau_s s)(\tau s+1)(1+\frac{\tau_d}{2}s)}{D(s)}, \tag{2.30}$$

where

$$\begin{aligned} D(s) &\triangleq s^2(1+\frac{\tau_d}{2}s)(1+\tau_s s)(\tau s+1)R(s) \\ &= s^2\left(1+\frac{\tau_d}{2}s\right)(1+\tau_s s)(\tau s+1) \\ &+ k_{PI} \cdot \left(\frac{\gamma_e}{AFR^0_s} + \frac{1}{W^0_f} \cdot s\right)((1-X)\tau s+1)\left(1-\frac{\tau_d}{2}s\right)(\tau_{PI}s+1). \end{aligned} \tag{2.31}$$

Since we want the estimated stoichiometric AFR, $\widehat{AFR}_s$, to track the actual stoichiometric AFR, AFR_s, we consider the closed-loop linearized error dynamics also. First, we define the estimation error variable, $\varepsilon_{AFR_s} \triangleq AFR_s - \widehat{AFR}_s$. We can then find the linearized

disturbance input–estimation error relation:

$$\begin{aligned}
\delta\varepsilon_{AFR_s} &= \delta AFR_s - \delta\widehat{AFR}_s \\
&= \delta AFR_s + \frac{\gamma_e}{s}\delta W_{fb} \\
&= \delta AFR_s + \frac{\gamma_e}{s}C_{fb}(s)G_{sl}(s)G_d(s)\delta\lambda \\
&= \delta AFR_s + \frac{\gamma_e}{s}C_{fb}(s)G_{sl}(s)G_d(s)\left(T_1(s)\delta W_{a,cyl} + T_2(s)\delta AFR_s\right) \\
&= \frac{\gamma_e}{s}C_{fb}(s)G_{sl}(s)G_d(s)T_1(s)\delta W_{a,cyl} + \left(1 + \frac{\gamma_e}{s}C_{fb}(s)G_{sl}(s)G_d(s)T_2(s)\right)\delta AFR_s \\
&\triangleq T_3(s)\delta W_{a,cyl} + T_4(s)\delta AFR_s, \qquad (2.32)
\end{aligned}$$

where the closed-loop transfer functions, $T_3(s)$ and $T_4(s)$, are expressed as:

$$T_3(s) = \frac{1}{W^0_{a,cyl}} \cdot \frac{\gamma_e k_{PI} X \tau s(\tau_{PI}s+1)(1-\frac{\tau_d}{2}s)}{D(s)}, \qquad (2.33)$$

$$T_4(s) = 1 - \frac{1}{AFR^0_s} \cdot \frac{\gamma_e k_{PI}(\tau_{PI}s+1)(\tau s+1)(1-\frac{\tau_d}{2}s)}{D(s)}. \qquad (2.34)$$

In summary, the augmented closed-loop system is expressed as:

$$\begin{bmatrix} \delta\lambda \\ \delta\varepsilon_{AFR_s} \end{bmatrix} = \begin{bmatrix} T_1(s) & T_2(s) \\ T_3(s) & T_4(s) \end{bmatrix} \begin{bmatrix} \delta W_{a,cyl} \\ \delta AFR_s \end{bmatrix}. \qquad (2.35)$$

It is easy to check that the DC gains of the closed-loop transfer functions, $T_1(s)$, $T_2(s)$, $T_3(s)$ and $T_4(s)$ are all zero with positive gains, which implies the disturbance rejection characteristic for the output AFR regulation ($\delta\lambda$) and for the estimation error $\delta\varepsilon_{AFR_s}$. Therefore, the λ output is asymptotically regulated to unity, ensuring stoichiometric operation, and the estimation of stoichiometric AFR asymptotically converges to the actual stoichiometric AFR if positive gains can be found that guarantee stability and good performance for all the four transfer functions in (2.35).

2.6 Controller Tuning

2.6.1 PI Gain Tuning of the λ Feedback Controller

For the gain tuning of the feedback PI controller, consider the system of a fixed stoichiometry without the stoichiometric AFR estimation. This is equivalent to setting $\gamma_e \equiv 0$ and

$\delta AFR_s \equiv 0$ in the closed-loop dynamics equation (2.26). The closed-loop dynamic behavior is then expressed as:

$$\delta\lambda = \frac{1}{W^0_{a,cyl}} \cdot \frac{1 - G_{fd}(s)}{1 + \frac{1}{W^0_f} G(s) C_{fb}(s)} \delta W_{a,cyl}. \tag{2.36}$$

The variable τ_{PI} in the PI feedback controller can be determined by placing the controller zero to cancel the slowest stable pole of $G(s)$. If the slowest pole is associated with the fuel dynamics, we can set $\tau_{PI} = \tau$. The root locus with variation of k_{PI} can then be utilized to tune the gain, k_{PI}.

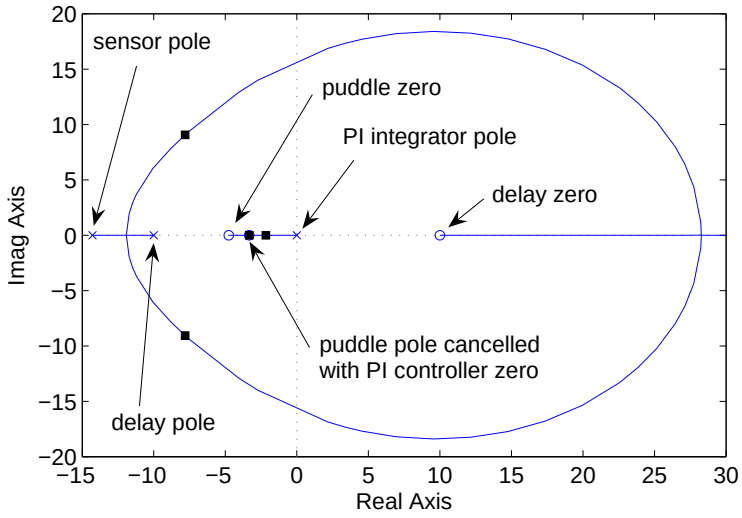

Figure 2.3 Root locus with the variation of k_{PI}

Fig. 2.3 shows the root locus of the closed-loop transfer function with the variation of k_{PI} for a fixed τ_{PI}. To obtain the locus in Fig. 2.3, the engine parameters were chosen as:

- $X = 0.3$, $\tau = 0.3$ sec, $\tau_d = 0.2$ sec, $\tau_s = 0.07$ sec .

And the PI control gains were tuned to:

- $\tau_{PI} = 0.3$, $k_{PI} = 0.0015$.

2.6.2 Ethanol Estimator Gain Tuning

First, the root locus is applied for the $D(s)$ in (2.31) for a set of fixed feedback gains, τ_{PI} and k_{PI}, determined by the method of the previous section.

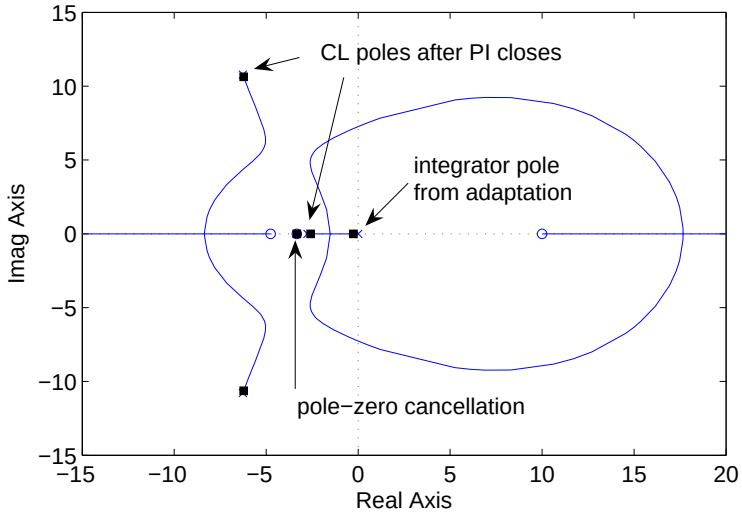

Figure 2.4 Root locus with the variation of γ_e

Fig. 2.4 shows the root locus of the original closed-loop transfer functions with the variation of γ_e for a set of fixed feedback gains previously tuned. The estimator gain γ_e affects the numerator of both transfer functions, $T_3(s)$ and $T_4(s)$, and hence tuning the gain is not clearly explained only with the root locus. However, the estimator gain where the roots cross the imaginary axis in the locus (Fig. 2.4) is $\gamma_e = 1.7 \times 10^5$, which determines the range of γ_e for stability. The estimator gain was chosen after a few simulations as:

- $\gamma_e = 5000$,

which is much smaller than the stability bound. Smaller gains may result in slower ethanol adaptations but reducing undesirable transient responses. Implication of different estimator gains will be addressed in section 5.2.

2.7 Simulation Results

Simulations were performed to see the disturbance rejection characteristic under perturbations in the cylinder air flow induced by tip-ins and tip-outs and a perturbation in the

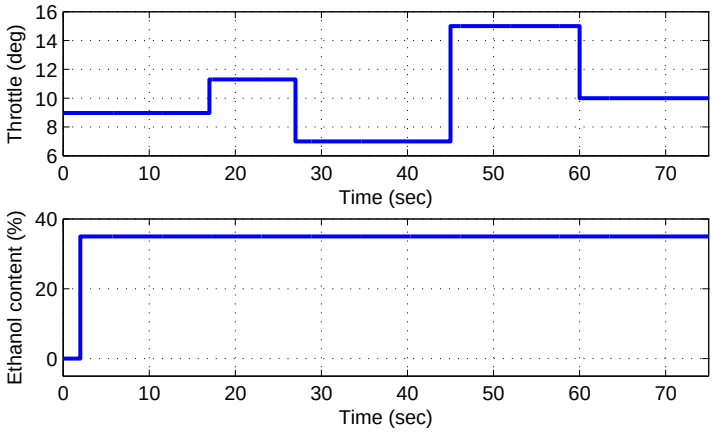

Figure 2.5 Simulation input

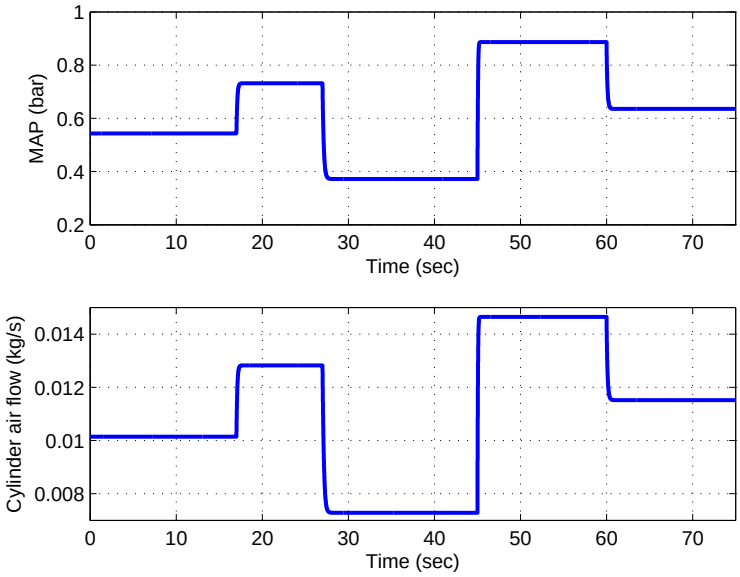

Figure 2.6 Manifold absolute pressure and air flow rate into the cylinder induced by throttle input

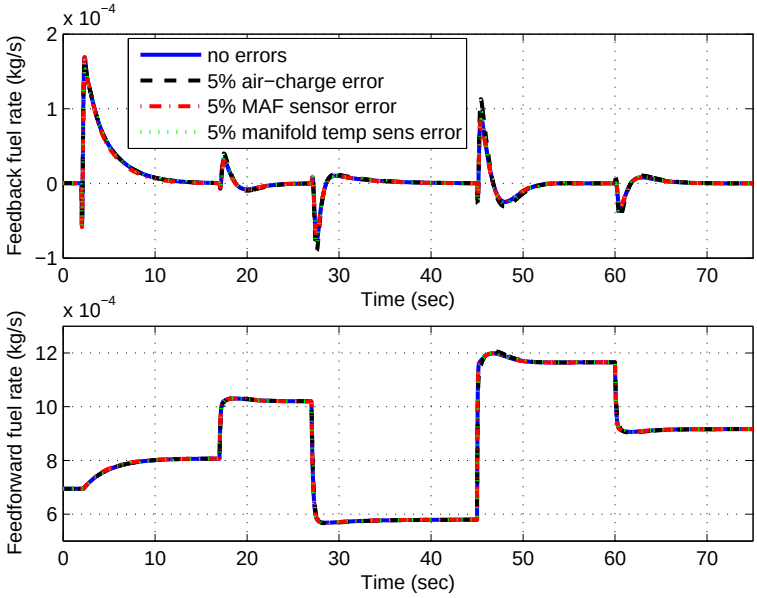

Figure 2.7 Simulated feedback fuel signal and feedforward fuel signal

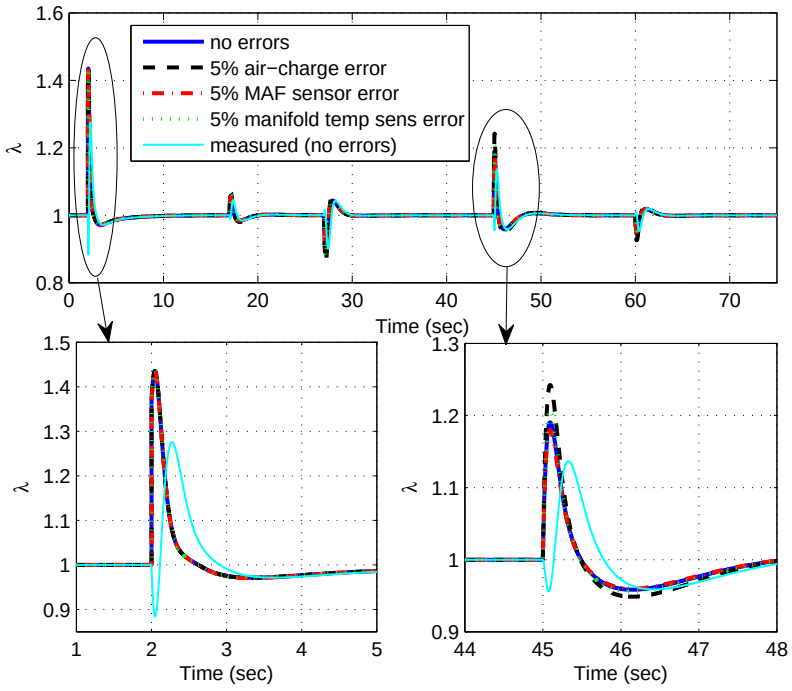

Figure 2.8 Simulated λ

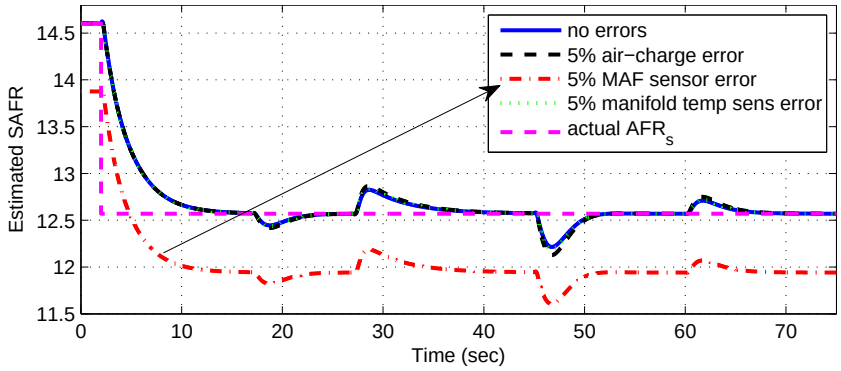

Figure 2.9 Simulated stoichiometric AFR estimation

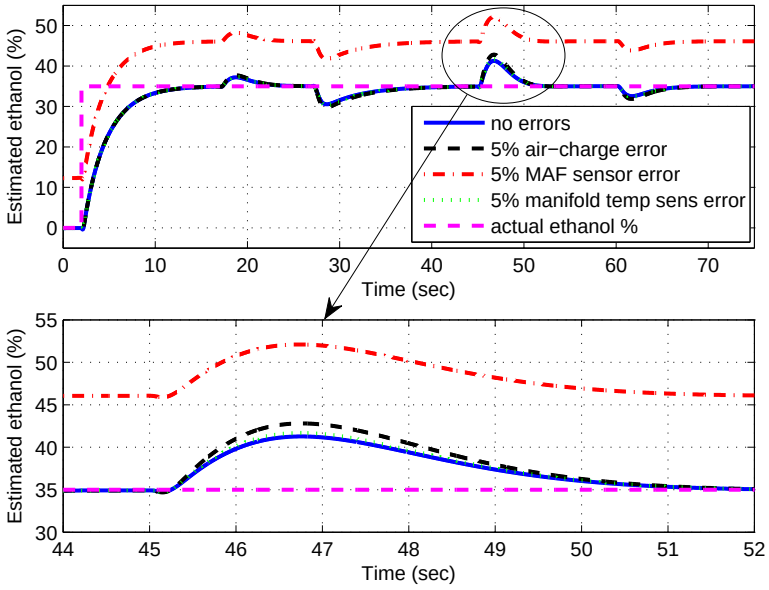

Figure 2.10 Simulated ethanol content estimation

stoichiometric AFR emulating a tank refill with unknown ethanol content fuel. Errors in air-charge estimation, mass air flow (MAF) sensor and manifold temperature sensor were also introduced with an error factor of 5% at a time to check the sensitivity of the ethanol estimation. The engine model introduced by Crossley and Cook [18] was utilized while maintaining the engine speed at 2000 RPM for throttle-to-cylinder air flow dynamics assuming that the rotational dynamics are much slower than the mass air flow and pressure dynamics.

The PI control gains and the estimator gain were determined as previously discussed: $\tau_{PI} = 0.3$, $k_{PI} = 0.0015$ and $\gamma_e = 5000$. The poles corresponding to the selected gains are marked as points on the root loci of Fig. 2.3 and Fig. 2.4. Fig. 2.5 shows the simulation in-

put. Throttle angles were modulated with a sequence of step changes and also a step change of actual ethanol content was applied. Initially the fuel used is E0 and then it is changed to E35. Because of this fuel change, different fuel dynamics parameters were used during the time span of E35 to account for the dynamic dependency on the fuel composition:

- $X_{E35} = 0.361$
- $\tau_{E35} = 0.4287$

Fig. 2.6 shows the change in the manifold absolute pressure and the air flow rate into the cylinder induced by the throttle change.

Fig. 2.7-2.10 show the simulation results. The relative air-to-fuel ratio λ and the estimated ethanol content asymptotically track their desired values. The λ error is very sensitive to an air-charge error. It is also moderately sensitive to manifold temperature sensor error, whereas, it is insensitive to MAF sensor error. The estimated stoichiometric AFR or the estimated ethanol content converges to the actual value except for the case of MAF sensor error where the steady-state ethanol percent estimation shows a 30% sensitivity. Hence, errors in the conventional sensors used in AFR control should be taken into account and ideally corrected by other means. In some sense the "sensorless estimation of ethanol content" typically for the AFR-based ethanol estimation is a misnomer and rigorous model-based engineering analysis should be pursued to minimize sensitivities using the combination of many sensors.

2.8 Steady-State Error Analysis

It is rather straightforward to analytically calculate how various modeling errors or sensor/actuator drifts propagate to cause steady-state errors in the ethanol estimation. Since the simulations in the previous sections indicate a high error sensitivity to MAF sensor drift, an analytical steady-state error calculation is provided below. Although possible injector drifts have not been considered in the previous simulation study, the following analysis considers injector drift as well as MAF sensor drift. Let f_{ea} be the MAF sensor error fraction so that the estimated air flow rate into the cylinder in the steady state be expressed as

$$\widehat{W}_{a,cyl} = (1 + f_{ea}) W_{a,cyl}. \tag{2.37}$$

Likewise, let f_{ef} be the fuel injection error fraction so that the actual fuel flow into the cylinder be expressed as

$$W_f = (1+f_{ef})W_{inj}. \tag{2.38}$$

Due to the λ PI-based feedback loop, λ is regulated at unity, and consequently, the actual steady-state AFR is regulated at the stoichiometric value independently of the fuel, i.e., $\lambda \equiv 1$ or $AFR \equiv AFR_s$ in steady state. From (2.5), the feedback signal W_{fb} should be zero in steady state with $\alpha_e \equiv 1$. Hence, the fuel injection control signal (issued fuel flow) is solely determined by the feedforward in steady state:

$$W_{inj} = \frac{\widehat{W}_{a,cyl}}{\widehat{AFR}_s}. \tag{2.39}$$

Therefore, the following equation holds in steady state:

$$AFR_s = AFR = \frac{W_{a,cyl}}{W_f} = \frac{1}{1+f_{ef}} \cdot \frac{W_{a,cyl}}{W_{inj}} = \frac{1}{1+f_{ef}} \cdot \frac{W_{a,cyl}}{\widehat{W}_{a,cyl}} \cdot \widehat{AFR}_s = \frac{\widehat{AFR}_s}{(1+f_{ea})(1+f_{ef})},$$

or,

$$\frac{\widehat{AFR}_s}{AFR_s} = (1+f_{ea})(1+f_{ef}). \tag{2.40}$$

Equation (2.40) describes how the MAF sensor error and fuel injection error propagate to error in estimation of SAFR. If the stoichiometric air-to-fuel ratio is expressed by the mass fraction of ethanol as in (2.2), the following equation is obtained:

$$\frac{9 \times \hat{e}_m + 14.6 \times (1-\hat{e}_m)}{9 \times e_m + 14.6 \times (1-e_m)} = (1+f_{ea})(1+f_{ef}), \tag{2.41}$$

where e_m and $\hat{e}_m$ are the actual mass fraction of ethanol and the estimated mass fraction of ethanol, respectively. The estimated mass fraction of ethanol, $\hat{e}_m$, is then expressed as a function of f_{ea}, f_{ef} and e_m in steady state:

$$\hat{e}_{m,ss,SAFR}(e_m, f_{ea}, f_{ef}) = e_m - f_e(f_{ea}, f_{ef})\,(2.6 - e_m)\,, \tag{2.42}$$

where the subscripts *ss* and *SAFR* are used to specify the 'steady state' and the 'SAFR-based' estimation realized by (2.2), and f_e is defined as:

$$f_e(f_{ea}, f_{ef}) \triangleq f_{ea} + f_{ef} + f_{ea}f_{ef}. \tag{2.43}$$

The steady-state estimation error $\tilde{e}_{m,ss,SAFR} \triangleq e_m - \hat{e}_{m,ss,SAFR}$ is then expressed as:

$$\tilde{e}_{m,ss,SAFR}(e_m, f_{ea}, f_{ef}) = f_e(f_{ea}, f_{ef})(2.6 - e_m). \tag{2.44}$$

The estimated volume fraction of ethanol, $\hat{e}_{ss,SAFR}$ can be then calculated by (2.4). The high sensitivity problem in ethanol content estimation under MAF sensor error and/or fuel injector error in steady state is obvious from (2.44). Either MAF sensor error fraction or fuel injector error fraction is amplified to ethanol content estimation error by factor of about 2.6 for E0 and of about 1.8 for E85, respectively. Fig. 2.11 shows the volumetric ethanol content estimation with 5% MAF sensor or fuel injector error ($f_e = \pm 0.05$).

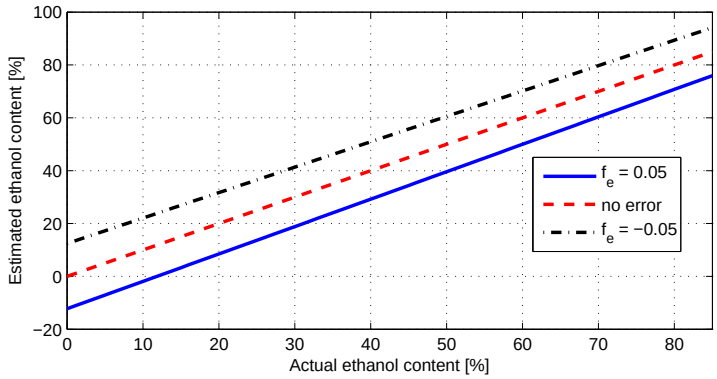

Figure 2.11 Ethanol content estimation in the steady state with 5% MAF sensor or fuel injector error

2.9 Conclusion

In this chapter, ethanol content estimation in flex-fuel vehicles is demonstrated with a model. Tuning and sensitivity are also studied. The linearized closed-loop dynamics are derived to present the disturbance rejection characteristic for λ and the ethanol estimation error. PI gain tuning for the fuel feedback control and the ethanol estimation gain tuning are shown with root loci. Two main issues regarding the ethanol content estimation are then elucidated by simulations and steady-state analysis:

1. Transient AFR response constrains the ethanol content estimation gain, resulting in slow adaptation.
2. The AFR-based ethanol content estimation is very sensitive on mass air flow sensor

error and/or fuel injector error.

These two issues motivate the remaining work in this dissertation.

1. Fast feedforward compensation of fuel puddle dynamics in PFI engines with an invertible puddle dynamics model for flex-fuel is necessary to minimize transient AFR excursions caused by throttle modulation during load demands.
2. A robust cylinder air flow estimation under MAF sensor drifts for robust SAFR-based ethanol content estimation is needed.
3. A robust fuel injector drift estimation for robust SAFR-based ethanol content estimation or ethanol content estimation independent of SAFR-based method is needed.

Chapters 3 and 4 address need (1). Chapter 5 addresses need (2) and chapter 6 proposes a methodology for addressing (3).

Chapter 3
Fuel Puddle Model

3.1 Introduction

To meet stringent emission requirements for spark ignition (SI) engines, air-to-fuel ratio control around the stoichiometric ratio of a fuel blend is important . For a given air charge, the stoichiometric fuel is typically achieved by a combination of feedforward and feedback fuel injection control. The feedback controller is based on the measured ratio (λ) of the actual air-to-fuel ratio (AFR) to the stoichiometric ratio (AFR_s) through an exhaust gas oxygen sensor. The λ ratio is compared to $\lambda^{des} = 1$ and the error is used by a proportional-integral (PI) controller to adjust the fuel command. Due to the long delays in the feedback loop, most engine controllers employ a feedforward fuel command which is primarily derived from the estimated cylinder air charge divided by the assumed stoichiometric ratio of the assumed fuel blend. Furthermore, the feedforward is usually designed to eliminate the transient effects of fuel puddle dynamics in port fuel injected (PFI) engines.

Since the puddle dynamics and hence the fuel entering the cylinder depend on the ethanol content, transient fuel compensation (TFC) should be based on the gasoline-ethanol content and should retain the ability to be used in wide range of operating conditions. To this end, it is desirable to design a low-order model with a few tunable physical parameters.

A model for transient fuel compensation of gasoline in the form of a simple linear time invariant model for the fuel puddle dynamics was first introduced by Aquino in the early 1980s [8]. The four puddle model (FPM) was developed by Curtis *et al.* in which fuel films are distributed in four different locations in a PFI engine and the physics of fuel vaporization is well-exploited with use of multi-component fuel model [19]. Locatelli *et al.* in [38] introduced a simple control-oriented wall-wetting model based on physical principles, where the port injected fuel dynamics is modeled as uniform droplet vaporization and exponential decay of the number of airborne droplets. An extended Kalman filter is used then to identify the physical parameters of the puddle dynamics for a gasoline fuel in [39]. The proposed model in this chapter has the same basic structure as that of the

model by Locatelli *et al.* [38] but extended to account for the vaporization of the various primitive chemical components that comprise gasoline-ethanol blends. Adapting [38] for an aggregate gasoline-ethanol fuel blend by interpolation between the gasoline and ethanol volatility curves was found inadequate for two reasons. First, the volatility curves obtained at standard atmospheric pressure do not account for the strong vaporization dependency on manifold pressure [42]. Second, the volatility curve of E85 is very steep at the boiling temperature of ethanol. As a result, there should be then huge uncertainty in obtaining the vaporized mass fraction in the model at liquid fuel temperature near the boiling temperature. Almost no vaporization is obtained below the boiling temperature and almost all vaporization is obtained above the boiling temperature. The second issue actually arises from a misinterpretation in the fuel volatility experiments used primarily for the classification of fuels [26]. Fuel volatility curves are obtained by a distillation process in which a volume of liquid fuel, whose exposed surface area is relatively small, is boiled by applying heat to the liquid. However, in the injected fuel spray and the fuel film on the intake wall, both the total volume of liquid fuel and the ratio of volume to the exposed surface area are small, thus causing a greater chance of evaporation before the liquid reaches the boiling point. In addition, the volatility curve cannot be utilized to evaluate certain property instantaneously since the vaporized fraction obtained by the volatility curve is a cumulative sum over a certain heating period.

Batteh and Curtis introduced a fuel puddle dynamic model with alternative fuels in 2005 [10]. They used the four puddle model but unfortunately the fuel was modeled as a different combination of several fuel components for each fuel blend, i.e. indolene, E22 and E85 not allowing a continuous variation within the E0-E85 range. Their model is actually not an invertible model, which was not fundamentally developed for transient compensator design.

In this chapter, we present a physics-based single puddle model using multi-component model fuel for FFVs. The model consists of two parts: a droplet evaporation model to generate the wall-impacting portion of the injected fuel and a single puddle vaporization model[1]. To capture the characteristics of the physical vaporization process, a multi-component fuel model parameterized by the ethanol content is utilized. To verify the validity of the model, model simulation results are compared with the experimental data provided in [10] for E0, E22 and E85.

[1]This structure is the same as that of the model by Locatelli *et al* [38].

3.2 Study with a Simple Fuel Puddle Model for a Specific Fuel Blend

In this section, we introduce a simple fuel puddle model for a specific fuel blend with a fixed volume fraction of ethanol, e, in the fuel blend based on the puddle model introduced in [32] which is adapted from Aquino's $X-\tau$ model [8]. The purpose of this section is to demonstrate the nonlinear variation of model parameters with change of the ethanol content, which are identified from experimental data, and hence to justify the need for the proposed model. The parameter calibration of X and τ is not a simple procedure in general because these two parameters depend on many engine variables such as pressure, flow and temperature [11,32,41]. Adding fuel composition variability increases further the complexity of the parameterization. Moreover, we show below that **parameterizing the puddle dynamics using Aquino's model structure for the two extreme ethanol concentrations, namely E0 and E85, does not allow interpolation for capturing the puddle behavior for intermediate ethanol blends**.

The mass of the fuel puddle at intake valve opening, m_p^{IVO}, is equal to the sum of the previous-cycle fuel puddle mass, m_p, and the fraction of the newly injected fuel m_{inj} that hits the puddle. The mass of fuel at intake valve closing, m_p, is reduced by the amount of evaporated fuel during the intake stroke, m_{evap}:

$$m_p(k) = m_p(k-1) + X(k)m_{inj}(k) - m_{evap}(k), \tag{3.1}$$

$$m_{f,cyl}(k) = (1-X(k))m_{inj}(k) + m_{evap}(k), \tag{3.2}$$

where $m_{f,cyl}(k)$ is the fuel mass inducted into the cylinder at step k, X is a time-varying parameter which is the fraction of injected fuel that hits the puddle and $m_p^{IVO}(k)$ is expressed by:

$$m_p^{IVO}(k) = m_p(k-1) + X(k)m_{inj}(k). \tag{3.3}$$

This model, (3.1) and (3.2), has exactly the same structure as introduced in [32]. To simplify the evaporation model, we introduce another time-varying parameter a in place of τ so that the evaporated mass at step k is expressed as $m_{evap}(k) = a(k)m_p^{IVO}(k)$. The parameter a is the evaporated mass fraction during the intake valve opening phase from the puddle mass at intake valve opening. The fuel puddle model is then expressed as:

$$m_p^{IVO}(k) = (1-a(k-1))m_p^{IVO}(k-1) + X(k)m_{inj}(k), \tag{3.4}$$

$$m_{f,cyl}(k) = (1-X(k))m_{inj}(k) + a(k)m_p^{IVO}(k). \tag{3.5}$$

For the parameter identification using the experimental data for each fuel blend, we include m_{inj} and $m_{f,cyl}$ in our observations since m_{inj} can be obtained by the commanded injection amount and $m_{f,cyl}$ can be calculated by using the measured (and approximated) cylinder air charge, measured universal exhaust gas oxygen (UEGO) data (λ) and appropriate transport delay and a time lag associated with the engine/sensor process. Let us define the following two variables for convenience:

$$\bar{a}(k) \triangleq 1 - a(k), \quad \bar{X}(k) \triangleq 1 - X(k). \tag{3.6}$$

From (3.5), $m_p^{IVO}(k)$ is expressed as:

$$m_p^{IVO}(k) = \frac{1}{a(k)}(m_{f,cyl}(k) - \bar{X}(k)m_{inj}(k)). \tag{3.7}$$

By eliminating m_p^{IVO} in (3.4) using (3.7), we obtain:

$$\begin{aligned} &m_{f,cyl}(k) - m_{inj}(k) = \\ &\qquad \frac{a(k)}{a(k-1)}\bar{a}(k-1)\left(m_{f,cyl}(k-1) - \bar{X}(k-1)m_{inj}(k-1)\right) - \bar{a}(k)X(k)m_{inj}(k). \end{aligned}$$

Assume that a is approximately the same between two consecutive cycles. By applying $a(k)/a(k-1) = 1$, the above equation is simplified to:

$$\begin{aligned} &m_{f,cyl}(k) - m_{inj}(k) = \bar{a}(k-1)m_{f,cyl}(k-1) \\ &- \bar{a}(k-1)\bar{X}(k-1)m_{inj}(k-1) - \bar{a}(k)X(k)m_{inj}(k). \end{aligned} \tag{3.8}$$

By introducing $\bar{b}(k) \triangleq \bar{a}(k)\bar{X}(k)$, (3.8) is expressed in a convenient form for regression:

$$\begin{aligned} &m_{f,cyl}(k) - m_{inj}(k) = m_{f,cyl}(k-1)\bar{a}(k-1) \\ &- m_{inj}(k)\bar{a}(k) - m_{inj}(k-1)\bar{b}(k-1) + m_{inj}(k)\bar{b}(k). \end{aligned} \tag{3.9}$$

We used each experimental data set of E0, E22 and E85 as shown in Fig. 3.6 and Fig. 3.8 for E0 fuel case, for parameter identification of $\bar{a}$ and $\bar{b}$ and hence X and a for each fuel blend. For the limited test data available, one engine speed and two manifold pressures and associated air and fuel flows during the warm-up phase for three fuels were available. The parameters X and a were, hence, only modeled as functions of engine coolant temperature. Parameters $\bar{a}$ and $\bar{b}$ were actually regressed as second order polynomials of engine coolant temperature, ECT, with coefficients identified by standard least squares technique. Data

from the very early phase of the engine start period were eliminated since engine RPM steeply increases. Half of the remaining data was utilized for the least squares fit and the other half was used for validation involving comparison of the experimental data and the identified model output.

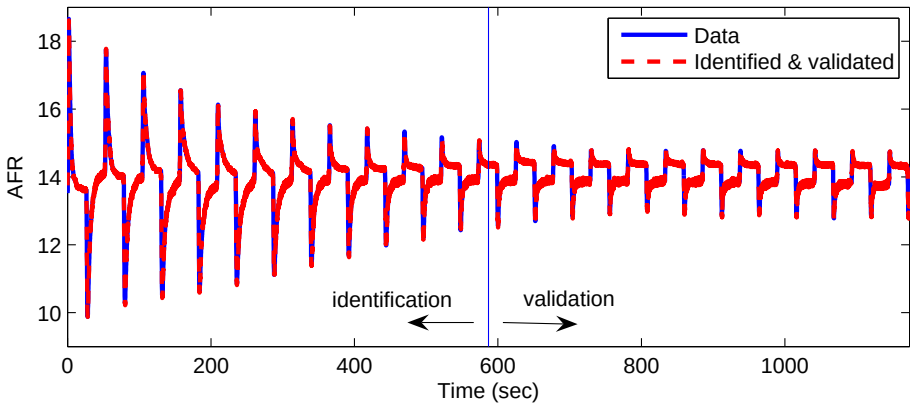

Figure 3.1 Air-to-fuel ratio comparison between the experimental data and the identified model output for E0

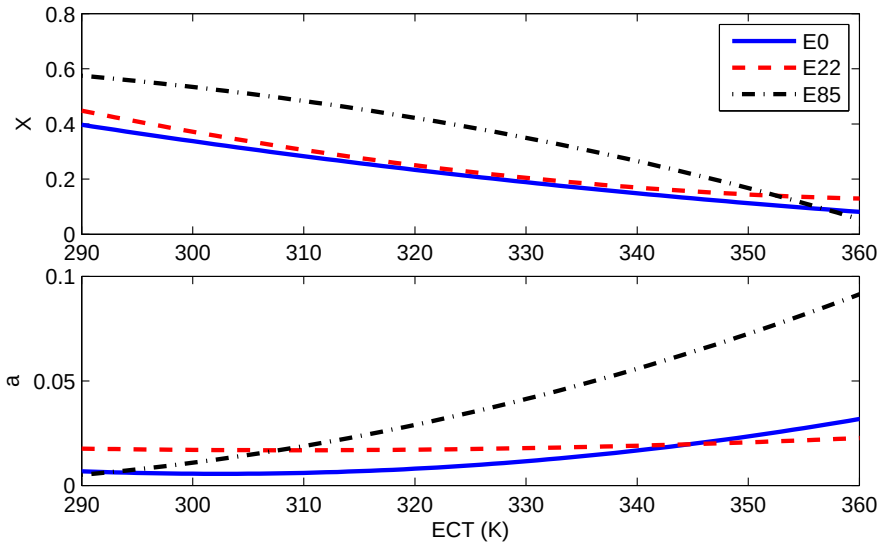

Figure 3.2 Identified fuel puddle model parameters for E0, E22 and E85

Fig. 3.1 depicts the air-to-fuel ratio comparison between the data and the model output for the data set of E0, showing good parameter fitting result. Fig. 3.2 shows the identified fuel puddle model parameters for each fuel blend versus the engine coolant temperature. It is observed that the parameters for E0, E22 and E85 are different and neither parameter

Table 3.1 Model fuel for gasoline

Component/ Mass fraction	Molecular Formula	Molecular Weight	Normal Boiling Point (K)	SAE 982519 [20]	SAE 982724 [26]	SAE 2005-01-1127 [10]	This Study
n-butane	C_4H_{10}	58.123	272.7	-	-	0.04	-
iso-pentane	C_5H_{12}	72.151	301.0	0.1618	0.1330	0.16	-
cyclo-hexane	C_6H_{12}	84.162	353.8	0.2091	0.1893	-	0.65
n-hexane	C_6H_{14}	86.177	341.9	-	-	0.025	-
iso-octane	C_8H_{18}	114.232	372.4	0.1670	0.1493	0.32	-
toluene	C_7H_8	92.141	383.8	0.1535	0.1824	0.255	-
ethyl-benzene	C_8H_{10}	106.168	409.3	0.1559	0.1462	-	0.20
123 trimethyl-benzene	C_9H_{12}	120.194	449.3	-	-	0.18	-
n-decane	$C_{10}H_{22}$	142.286	447.3	0.1171	0.1210	-	0.11
naphthalene	$C_{10}H_8$	128.174	491.1	0.0355	0.0319	-	0.04
n-tridecane	$C_{13}H_{28}$	184.365	508.6	-	-	0.02	-
ethanol	C_2H_6O	46.069	351.4	-	0.0469	-	-

for E22 can be uniformly interpolated between the E0 and E85 parameters. Based on this observation, it is not clear how many fuel blends one needs to test in order to identify and adequately interpolate the puddle parameters in addition to the fuel specific parameterizations for engine coolant temperature, manifold absolute pressure and engine RPM [32]. Note that on-line identification of the X and a parameters [54] is very challenging due to the fast changes in the parameters space (RPM, MAP, ECT) during typical driving scenarios. Therefore, even though fuel puddle dynamics seems to be a fairly simple dynamic process, a certain level of complexity introduced by a physics-based model may be inevitable to appropriately capture the different dynamic characteristics for different fuel blends.

3.3 Multi-Component Model Fuel

The multi-component model fuel for gasoline can be constructed by selecting a combination of several fuel compounds which mimics the volatility of real fuel as in [26]. Table 3.1 shows such specific combinations for gasoline model listed in [20], [26] and [10] and the combination used in this study. The mass fractions used in this research were determined

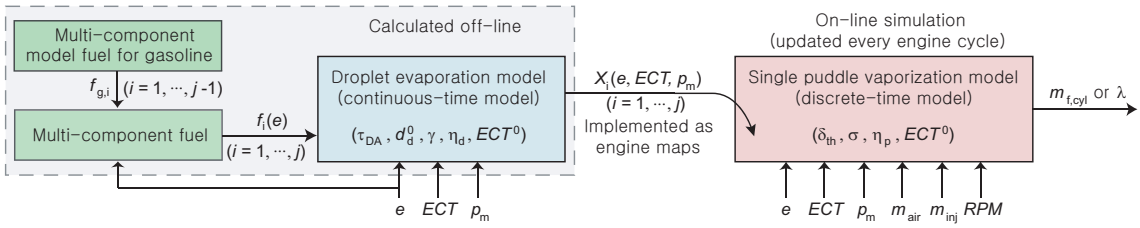

Figure 3.3 Schematic of fuel puddle dynamic model for gasoline-ethanol E0-E85 blend

by reducing fuel components and adjusting mass fractions from the combination of mass fractions of [20] until the error between the modeled and measured [10] λ converged to a small value after the model tuning constants were fixed to match the experimental data for the model fuel of [20]. The experimental data targeted to provide the model tuning are the λ responses from the engine warm-up tests with several tip-ins and tip-outs as described in [10] and shown in section 3.6 where simulations are discussed.

A gasoline-ethanol blend is then modeled as a combination of 5 chemical compounds including ethanol. Let e and e_m denote the volume fraction and the mass fraction of ethanol in a gasoline-ethanol blend, respectively. The mass fraction e_m is calculated by:

$$e_m = \frac{e}{e + (1-e)/1.056} \tag{3.10}$$

from (2.1). Let $f_{g,i}$ denote the mass fraction of each component for the gasoline model fuel where $i = 1, \cdots, 4$ is the index representing each component, which is directly read from the last column in Table 3.1. The mass fraction of each component in the fuel blend is then expressed as:

$$f_i = f_{g,i} \times (1 - e_m), \quad i = 1, \cdots, 4,$$
$$f_5 = e_m.$$

3.4 Droplet Evaporation Model

It is assumed that spherical shape droplets of the same size are formed right after fuel injection. The total number of airborne droplets are modeled as an exponential decaying process [38]. The number of droplets is reduced by hitting the port wall. Droplets vaporize while they are airborne. The total mass of vaporization from droplets is regarded as the fuel mass inducted into the cylinder. A mathematical model for this process is constructed as follows. All fuel is injected as droplets of initial diameter d_d^0 with resulting initial droplet

mass $m_d^0 = \frac{\pi}{6}\rho^0 (d_d^0)^3$ and initial mass of each component in a droplet $m_{d,i}^0 = f_i \cdot m_d^0$, where ρ^0 denotes the initial density of mixture. Each droplet is then reduced by the droplet evaporation. Assuming stagnant air surrounding a droplet[2] and fuel vapors far from the droplet surface being zero, the evolution of each droplet mass m_d and its individual component masses $m_{d,i}$ are dictated by the droplet evaporation rate $\dot{m}_{EV,d}$ as in [50, 51, 63]:

$$\frac{d}{dt} m_d = -\dot{m}_{EV,d}, \tag{3.11}$$

$$\frac{d}{dt} m_{d,i} = -Y_{s,i} \cdot \frac{1 + B_d}{B_d} \cdot \dot{m}_{EV,d} \tag{3.12}$$

$$\dot{m}_{EV,d} = 2\pi \cdot d_d \cdot \rho \cdot D \cdot \ln(B_d + 1) \tag{3.13}$$

where the droplet diameter follows the droplet mass reduction $d_d = \left(\frac{6 m_d}{\pi \rho}\right)^{1/3}$, $Y_{s,i}$ denotes the mass fraction of each fuel component above the droplet, B_d is the transfer number, D is diffusion coefficient of the fuel vapor, and the specific volume $1/\rho$ is calculated as mass-weighted average of specific volumes of each fuel component. Although the experimentally observed vapor pressure for gasoline-ethanol blends deviates from the one expected from ideal mixtures as shown in [35], we neglect this complexity and use Raoult's law to our control-oriented model. According to Raoult's law [58], the mass fraction of each fuel component above the droplet is expressed as:

$$Y_{s,i} = \frac{VP_i \times f_{d,i}}{\sum_i (VP_i \times f_{d,i}) + PP_{air} \cdot M_{air} \cdot \sum_i f_{d,i}/M_i}. \tag{3.14}$$

The transfer number B_d is calculated as follows [10, 55, 58]:

$$B_d = \frac{\sum_i VP_i \times f_{d,i}}{PP_{air} \times M_{air} \times \sum_i f_{d,i}/M_i}, \tag{3.15}$$

with the partial pressure of air calculated from

$$PP_{air} = p_m - \frac{\sum_i VP_i \times f_{d,i}/M_i}{\sum_i f_{d,i}/M_i}, \tag{3.16}$$

where summation $\sum_i$ is performed over all fuel components, VP_i denotes the normal vapor pressure of the i-th fuel component, M_i is the molecular weight of the i-th fuel component, M_{air} is the molecular weight of air (28.97 g/mol), p_m denotes the manifold absolute pressure (MAP) and $f_{d,i}$ is defined as the mass fraction of the i-th fuel component in the

[2] Although restrictive, this assumption is reasonable because fuel is injected before the intake stroke, hence, before any significant air flow surrounds the droplets.

droplet:

$$f_{d,i} \triangleq \frac{m_{d,i}}{\sum_i m_{d,i}} = \frac{m_{d,i}}{m_d}. \tag{3.17}$$

The diffusion coefficient, D, and the normal vapor pressures, VP_i, should be evaluated at the droplet surface temperature. However, it is hard to exactly predict the temperature. Instead, we use an apparent temperature which is parameterized by the ethanol content, e, and the engine coolant temperature, ECT:

$$T_{app,d} = ECT - (e+\gamma)\cdot\eta_d\cdot(ECT - ECT^0), \tag{3.18}$$

where γ, η_d and ECT^0 are three tuning constants. There are publications of fuel puddle dynamic models which include temperature dynamics of explicit states, i.e. differential equations for some temperatures, e.g. valve, cylinder and port temperatures [10, 38]. The purpose of a dynamic temperature model is to explicitly evaluate a physical property at the temperature of a designated location. However, it is still difficult to establish a simple dynamic model to predict the droplet surface temperature and a dynamic temperature model usually needs several tuning constants in the equations. A dynamic temperature model may be introduced to our model in future study. Nevertheless, in this research, we regard a temperature change approximately as a static process parameterized by the engine coolant temperature, ECT, which is measured on-line. The apparent temperature does not play a role of approximating a specific temperature at a designated location. It serves as a reference temperature which gives relative distance of thermophysical properties relevant to the physical process. Using (3.14) and (3.15), (3.12) is expressed as:

$$\frac{d}{dt}m_{d,i} = -\frac{VP_i(T_{app,d})\times f_{d,i}}{\sum_i VP_i(T_{app,d})\times f_{d,i}}\cdot\dot{m}_{EV,d}. \tag{3.19}$$

Calculation of diffusion coefficient, D, for multi-component fuel is approximated here by mass-weighted average of diffusion coefficients of each fuel component and each coefficient may be looked up from [64] which gives functional expression in temperature. The following relation that kinetic theory would pose under ideal gas behavior assumption is also utilized [28, 29]:

$$D \sim \frac{T_{app,d}^{3/2}}{p_m}. \tag{3.20}$$

Calculation of normal vapor pressures, VP_i, can be also done by the functional expression in temperature provided in [64].

Let X_i denote the ratio of the wall-impacting mass of i-th component to the total injected mass of fuel, which is the output of the droplet evaporation model and is the input to the

single puddle vaporization model which will be discussed in the following section. The mass balance is then expressed as:

$$f_i - X_i = \frac{1}{m_d^0} \int_0^{t_{ev}} \dot{m}_{EV,d,i} \cdot e^{-\frac{t}{\tau_{DA}}} dt. \tag{3.21}$$

where τ_{DA} is the time constant of the decay of the number of airborne droplets, t_{ev} is the time for complete vaporization of single droplet, i.e. $m_d|_{t=t_{ev}} = 0$. The time constant τ_{DA} is a universal tuning constant over the whole range of ethanol content, which should be significantly smaller than one engine cycle duration.

According to the model from (3.11)-(3.21), X_i is varying in accordance with the variation of engine coolant temperature, ECT, manifold absolute pressure, p_m, and also with the variation of the ethanol content, e, i.e., $X_i = X_i(e, ECT, p_m)$. If we consider the effect of flow of air, then Reynolds number and Schmidt number should be involved in the formulation; in this case, X_i may be also dependent on the air charge mass, engine RPM, and the port diameter as in [50] or [38]. Nevertheless, the stagnant air assumption may well capture the whole process of droplet evaporation or the spray injection process in port fuel injection (PFI) engines considering the usual timing of the fuel injection to the intake port before the intake valves open.

Fig. 3.4 shows the wall-impacting fraction for the four gasoline components X_i, $i = 1, \cdots, 4$ for E0 and E43, and ethanol X_5 for E100 and E43 as an example of the wall impacting fractions after the model calibration and the fuel simplification discussed in Section 3.6. The last subplot of Fig. 3.4 shows the wall-impacting fraction for ethanol. Fig. 3.4 depicts that lighter fuel components have relatively small X_i among gasoline components since more droplet mass is evaporated before hitting the port wall, e.g., cyclo-hexane has very small number of X_i even though its nominal mass fraction in gasoline is the highest, i.e., 0.65 in Table 3.1.

The evolution of the droplet evaporation and the resulting wall impacting mass fractions can be computed off-line and produce a five (5) three-dimensional (e, ECT, p_m) look-up table which can be used in the fuel puddle evaporation process. By observing the trends of the computed X_i for the different blends (after the tuning and the fuel composition reduction discussed later in Section 3.6) in Fig. 3.4, one can see that for example, cyclohexane shows that at $ECT = 290\,\mathrm{K}$ and $p_m = 0.8\,\mathrm{bar}$ the computed impact factor for E43 is $0.1897 = X_1(0.43, 290, 0.8) \approx (1 - 0.43) X_1(0, 290, 0.8) = 0.1780$. This motivated the

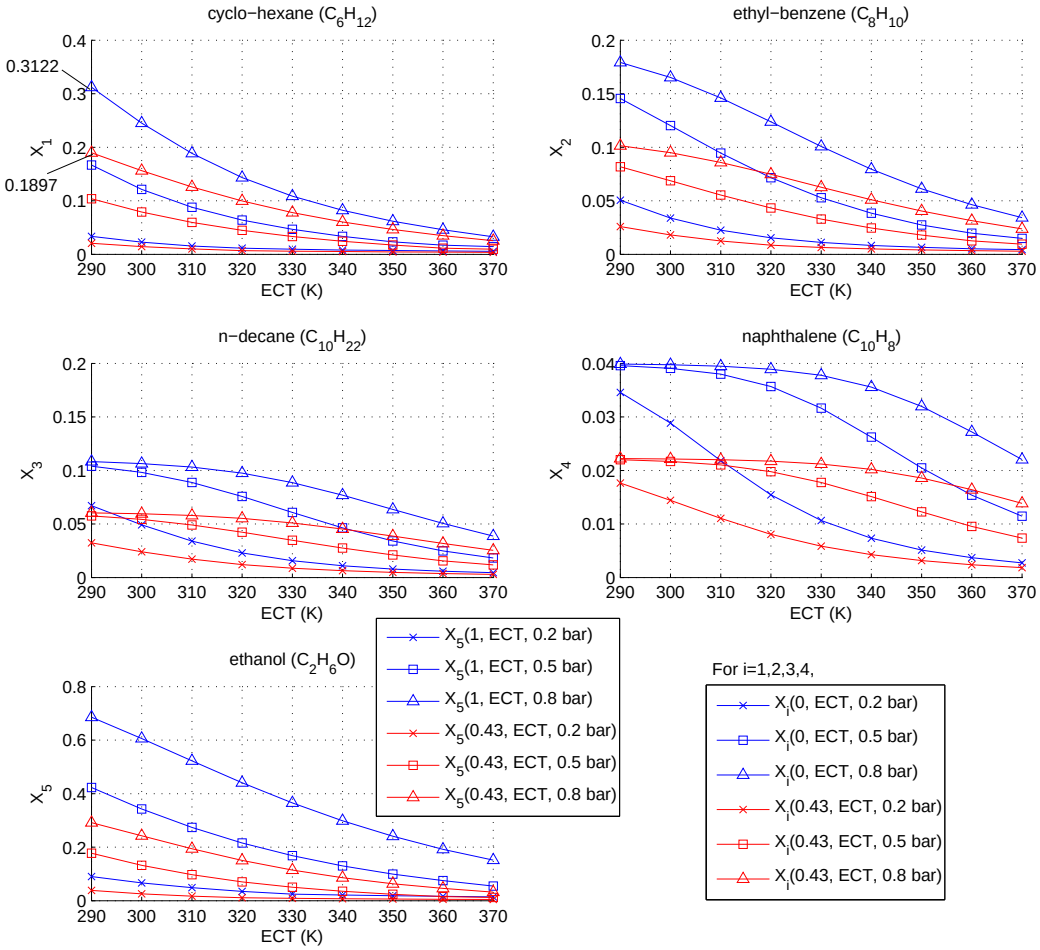

Figure 3.4 Wall-impacting factor of gasoline fuel component ($X_i(0,ECT,p_m)$ and $X_i(0.43,ECT,p_m)$ $i = 1,\cdots,4$) and ethanol ($X_5(1,ECT,p_m)$ and $X_5(0.43,ECT,p_m)$) at $p_m = 0.2, 0.5, 0.8$ bar

computation of

$$\hat{e}_i = 1 - \frac{X_i(e,ECT,p_m)}{X_i(0,ECT,p_m)} \quad \text{for } i = 1,\cdots,4,$$
$$\hat{e}_5 = \frac{X_5(e,ECT,p_m)}{X_5(1,ECT,p_m)}.$$

shown in bars in Fig. 3.5. Fig. 3.5 shows that the computed values of $\hat{e}_i$ were approximately equal to the fuel ethanol content, $\hat{e}_i \approx e$ for all $i = 1,\cdots,5$ leading to linear interpolation with respect to ethanol concentration for the impacting factor of each fuel component without loss of accuracy. The multi-component fuel wall impacting factors can then be stored

as five (5) two-dimensional (ECT, p_m) look-up tables:

$$X_i(e, ECT, p_m) = (1-e)X_i(0, ECT, p_m) \quad \text{for } i = 1, \cdots, 4, \tag{3.22}$$

$$X_5(e, ECT, p_m) = eX_5(1, ECT, p_m). \tag{3.23}$$

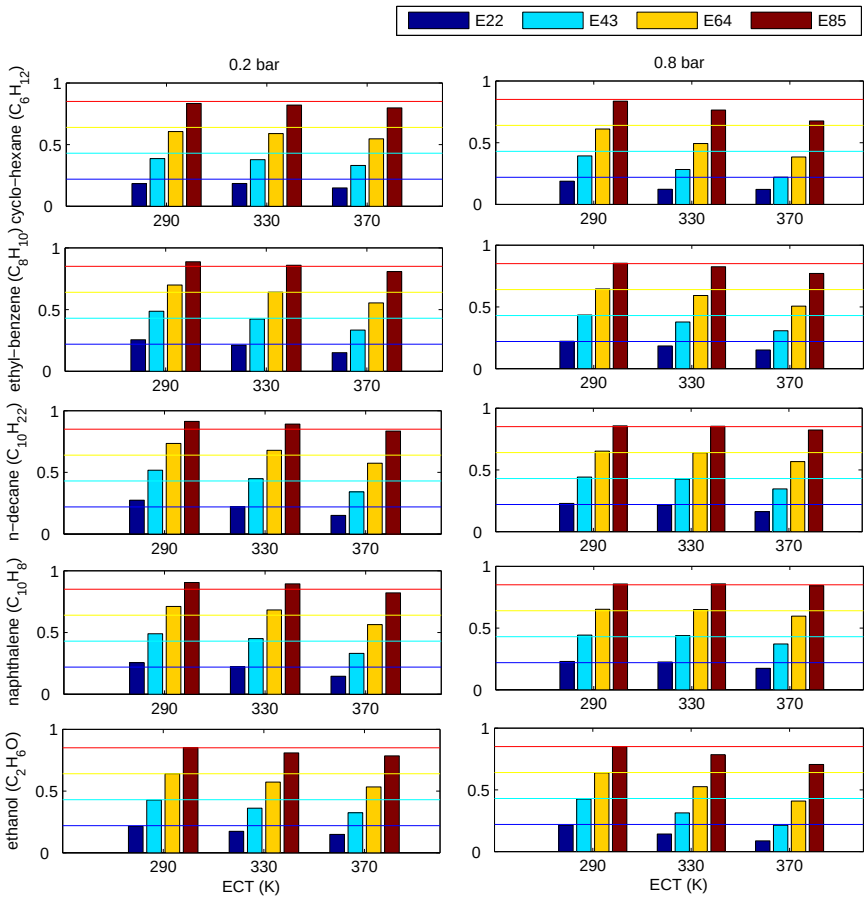

Figure 3.5 Effective ethanol fraction $\hat{e}_i$ in linear interpolation of X_i for each fuel component

Specifically, Fig. 3.5 shows the computed $\hat{e}_i$ for different gasoline-ethanol mixtures (22%, 45%, 64%, and 85%) in bars of blue, cyan, yellow, and red colors and at three different coolant temperatures (ECT) and two manifold pressures. Fig. 3.5 suggests that the linear interpolation, (3.22) and (3.23), is especially a good approximation in low engine coolant temperature range, where the wall-impacting mass fraction is relatively high as shown in Fig. 3.4 and hence more accuracy is necessary. For better accuracy, the 5 wall impacting factors $X_i(e, ECT, p_m)$ could be stored as three dimensional maps as a function of finer fuel volumetric ethanol content than the one suggested from (3.22)-(3.23) based on the two end compositions, namely E0 and E100.

Note that the total wall-impacting mass fraction of the injected fuel is the sum of each X_i over all fuel components, $X = \sum_i X_i$. The total wall-impacting mass fraction, X, may be compared with certain reference values, e.g., X obtained by the least squares fit from section 3.2, for initial rough calibration. However, X alone cannot capture the vaporization process of fuel puddle and both of the wall-impacting mass fraction of each fuel component, X_i, and aggregate factor X are finally implemented in the single puddle vaporization model which will be discussed in the next section.

3.5 Single Puddle Vaporization Model

Some droplets of the injected fuel hit the port wall before their complete evaporation. That mass forms a fuel puddle on the port wall and some portion of the puddle also vaporizes from the puddle. The mass of each component in the fuel puddle at intake valve opening (IVO) is equal to the sum of the previous-cycle mass and the portion of the newly injected fuel that hits the puddle. The total puddle mass at IVO is equal to the sum of masses of each component:

$$m_{p,i}^{IVO}(k) = m_{p,i}(k-1) + X_i(e, ECT, p_m) \times m_{inj}(k), \quad i = 1, \cdots, j, \tag{3.24}$$

$$m_p^{IVO}(k) = \sum_{i=1}^{j} m_{p,i}^{IVO}(k), \tag{3.25}$$

where k denotes the event or cycle number, i is index for fuel component and j is the total number of fuel components ($j = 5$). It is assumed that the rest of injected fuel is evaporated and enter the cylinder on the intake stroke. The puddle mass at intake valve closing (IVC), m_p, is derived from Locatelli's model [38]. Assuming a cylindrical fuel puddle along the port wall, let δ_{th} be the thickness of the puddle which is assumed constant along the height of the fuel puddle. The height of the puddle is varying according to the mass variation of the puddle. The vaporization rate is expressed as:

$$\dot{m}_{EV,p} = \frac{\rho \cdot A_p}{d_{in}} \cdot D_p \cdot Sh_p \cdot \ln(1 + B_p), \tag{3.26}$$

$$= \frac{\breve{m}_p}{d_{in} \cdot \delta_{th}} \cdot D_p \cdot Sh_p \cdot \ln(1 + B_p), \tag{3.27}$$

where ρ is the density of the fuel puddle, A_p is the surface area of the puddle exposed to air flow, d_{in} is the port diameter, D_p is the diffusion coefficient, Sh_p is the Sherwood number, B_p is the transfer number and $\breve{m}_p$ is the instantaneous puddle mass such that $\dot{m}_{EV,p} = -\dot{\breve{m}}_p$.

The fuel puddle mass at IVC, $m_p(k)$, is then obtained by integrating (3.27), for one cycle duration:

$$m_p(k) = m_p^{IVO}(k)(1+B_p)^{-\alpha}, \tag{3.28}$$

where

$$\alpha \triangleq C(e) \cdot \frac{120}{N} \cdot \frac{D_p \cdot Sh_p}{d_{in} \cdot \delta_{th}}. \tag{3.29}$$

In the above equation, N denotes the engine RPM and a correction factor, C, parameterized by the ethanol content, e, is introduced to correct the effect of variation of fuel film thickness according to the ethanol content variation. The correction factor is modeled as a linear variation with the change of the ethanol content:

$$C(e) = 1 - \sigma e, \tag{3.30}$$

where σ is a tuning constant. The evaporated mass is expressed as:

$$\begin{aligned} m_{evap}(k) &\triangleq m_p^{IVO}(k) - m_p(k) \\ &= m_p^{IVO}(k)\left[1-(1+B_p)^{-\alpha}\right] \\ &= \bar{\alpha} \cdot m_p^{IVO}(k), \end{aligned} \tag{3.31}$$

where the mass fraction of evaporation from the mass at IVO is defined as $\bar{\alpha} \triangleq 1-(1+B_p)^{-\alpha}$. Sherwood number is computed as follows [61]:

$$\begin{aligned} u_{A\infty} &= \frac{m_{air} \cdot N}{120} \cdot \frac{4}{\rho_A \cdot \pi \cdot d_{in}^2}, \\ Re_p &= \frac{u_{A\infty} \cdot d_{in}}{\nu_A}, \\ Sc_p &= \frac{\nu_A}{D_p}, \\ Sh_p &= 0.023 \cdot Re_p^{0.83} Sc_p^{0.44}, \end{aligned} \tag{3.32}$$

where ρ_A denotes density of air, ν_A denotes kinematic viscosity of air, and m_{air} denotes air charge mass per cycle. Let us define the mass fraction of each component in the puddle at IVO:

$$f_{p,i}(k) \triangleq \frac{m_{p,i}^{IVO}(k)}{m_p^{IVO}(k)}. \tag{3.33}$$

Let VP_i denote the normal vapor pressure of each fuel component as used in the droplet evaporation model. The diffusion coefficient, D_p, and the normal vapor pressures, VP_i are

evaluated at another apparent temperature for the fuel puddle vaporization:

$$T_{app,p} = ECT - e \cdot \eta_p \cdot (ECT - ECT^0), \tag{3.34}$$

where η_p is another tuning constant and ECT^0 is the same tuning constant used in the droplet evaporation model. Calculation of D_p is similarly performed to the droplet evaporation model (3.20) as $D_p \sim T_{app,p}^{3/2}/p_m$. The variable B_p is computed similar to the droplet evaporation model as follows:

$$PP_{air}(k) = p_m(k) - \frac{\sum_i VP_i \times f_{p,i}(k)/M_i}{\sum_i f_{p,i}(k)/M_i}, \tag{3.35}$$

$$B_p(k) = \frac{\sum_i VP_i \times f_{p,i}(k)}{PP_{air}(k) \times M_{air} \times \sum_i f_{p,i}(k)/M_i}. \tag{3.36}$$

The computation at the step k is completed by updating the masses of each fuel component at the end of the intake stroke accounting for the evaporated fuel:

$$m_{evap,i}(k) = \min \left\{ m_{p,i}^{IVO}(k),\ m_{evap}(k) \times \frac{VP_i(T_{app,p}) \times m_{p,i}^{IVO}(k)}{\sum_i VP_i(T_{app,p}) \times m_{p,i}^{IVO}(k)} \right\}, \tag{3.37}$$

$$m_{p,i}(k) = m_{p,i}^{IVO}(k) - m_{evap,i}(k). \tag{3.38}$$

Finally, the mass of fuel inducted into the cylinder is:

$$m_{f,cyl}(k) = (1 - X(e, ECT, p_m)) \times m_{inj}(k) + \sum_{i=1}^{j} m_{evap,i}(k). \tag{3.39}$$

We can compute air-to-fuel ratio, AFR and λ at each step as follows:

$$AFR(k) = \frac{m_{air}(k)}{m_{f,cyl}(k)}, \tag{3.40}$$

$$\lambda(k) = \frac{AFR(k)}{AFR_s(k)}, \tag{3.41}$$

where the stoichiometric air-to-fuel ratio is computed by:

$$AFR_s = 9 \times e_m + 14.6 \times (1 - e_m). \tag{3.42}$$

Fig. 3.3 depicts the model summary where inputs to each submodel and tuning constants associated with each submodel are shown. In the droplet evaporation model, the parameter d_d^0 indicates the initial droplet diameter right after injection. The droplet evaporation model

passes X_i over to the single-puddle vaporization model as inputs. Since X_i is an integration result according to (3.21), the internal states during the droplet evaporation simulation for implementation at every numerical computation time step do not have to be known. Therefore, to avoid unnecessary increase of on-line computation time, which might be caused by computing X_i at every engine cycle, the droplet evaporation model is simulated off-line to generate X_i and the results are implemented as engine maps in the single-puddle vaporization model which updates its states every engine cycle.

3.6 Simulation

The resulting model takes 6 inputs, e, ECT, p_m, m_{air}, m_{inj}, RPM, and uses 8 parameters, τ_{DA}, d_d^0, γ, η_d, ECT^0, δ_{th}, σ, η_p to produce the fuel amount inducted into the cylinder and λ as shown in Fig. 3.3. The effect and topology of the 8 parameters in the model structure is physically motivated. The droplet evaporation model depends on two parameters: the droplet decay time constant τ_{DA} introduced in the model in [38] and the droplet diameter d_d^0 which is physically necessary and is tuned according to the τ_{DA} setting. The puddle vaporization model depends on two physically motivated parameters: the puddle thickness δ_{th} and σ introduced to consider actual variation of δ_{th} on ethanol content. The vaporization process depends on, and at the same time, influences temperature through 4 parameters, γ, η_d, η_p and ECT^0. These 4 parameters (two for the droplet and two for the film) are used to account for the vaporization effect on surface temperature approximated as apparent temperature. This number of parameters in the ethanol-temperature relationship is not actually too high if one considers using an affine fit for each fuel blend we used for calibration. For parameter tuning and the model validation, the three different experiments of [10] have been obtained.

The experimental data show the λ traces measured by a universal exhaust gas oxygen (UEGO) sensor for different fuel blends of E0, E22 and E85, respectively, while the 4.6L 2V engine operates from cold start till full warm-up for each blend and several steps of tip-ins and tip-outs are applied.

As stated in section 3.3, the multi-component model fuel for gasoline was first taken from the mass fractions in [20]. The 8 parameters associated with our model were then tuned for that model fuel which uses 8 chemical compounds including ethanol. The tuning of the model parameters is explained below. First, the initial droplet diameter, d_d^0, was chosen and the time constant, τ_{DA}, was tuned so that the whole droplet evaporation process around the engine coolant temperature range (290-370 K) and the manifold absolute pres-

sure range (0.1-0.8 bar) yielded a reasonable range of the wall impacting factors, X_i. The value for ECT^0 was determined to be close to ambient temperature. The product of γ and η_d, $\gamma \cdot \eta_d$ was tuned to yield proper shapes of λ excursions for E0, and then each parameter was determined by matching the λ excursions for E85. Likewise, the film thickness, δ_{th}, was tuned to match the film vaporization rate for E0; σ and η_p were tuned to match the data for E85. In this way, true validation is obtained through the comparison between simulation and experiments for E22.

Table 3.2 Tuned parameters of simulation

Parameter	Value	Unit	Model
τ_{DA}	8.0×10^{-5}	[s]	Droplet evaporation
d_d^0	6.0×10^{-5}	[m]	
γ	0.80	-	
η_d	0.31	-	
ECT^0	290	[K]	Droplet evaporation and single-puddle vaporization
σ	0.60	-	Single-puddle vaporization
η_p	0.75	-	
δ_{th}	3.0×10^{-3}	[m]	

Table 3.2 summarizes the tuned parameters and their values. The port diameter, d_{in} is 0.045 m. Using these parameters, the gasoline fuel components were then reduced to yield similar model simulation results to those of the previously used gasoline fuel components of [20]. Table 3.1 summarizes the optimized fuel fractions in the last column and the following simulations used those fuel fractions associated with a 4-component gasoline instead of the original 7 components in [20]. As previously discussed in section 3.4, X_i for gasoline components ($i = 1, \cdots, 4$) and X_5 for ethanol are calibrated for E0 and E100 cases, respectively, and all the intermediate X_i's for intermediate fuel blends are interpolated by (3.22) and (3.23)[3]. Further work is needed for establishing a further simplification and/or automated parameter calibration technique. A detailed analysis of the model sensitivity on small fuel variability, such as summer and winter grade gasoline, is also required in the future.

[3]Calibration for X_5 with respect to E85 data is first performed and X_5 for E100 is then obtained using the calibrated parameters.

Fig. 3.6 shows the inputs to the (puddle vaporization) model for E0, based on the warm-up tests performed in [10]. Similar inputs obtained from the tests performed in [10] were used for E22 and E85, although not shown here. The air charge associated with the six inputs was estimated using the methodology of [27] and [57] and Ford proprietary calibration of the manifold filling dynamic model and the cylinder pumping.

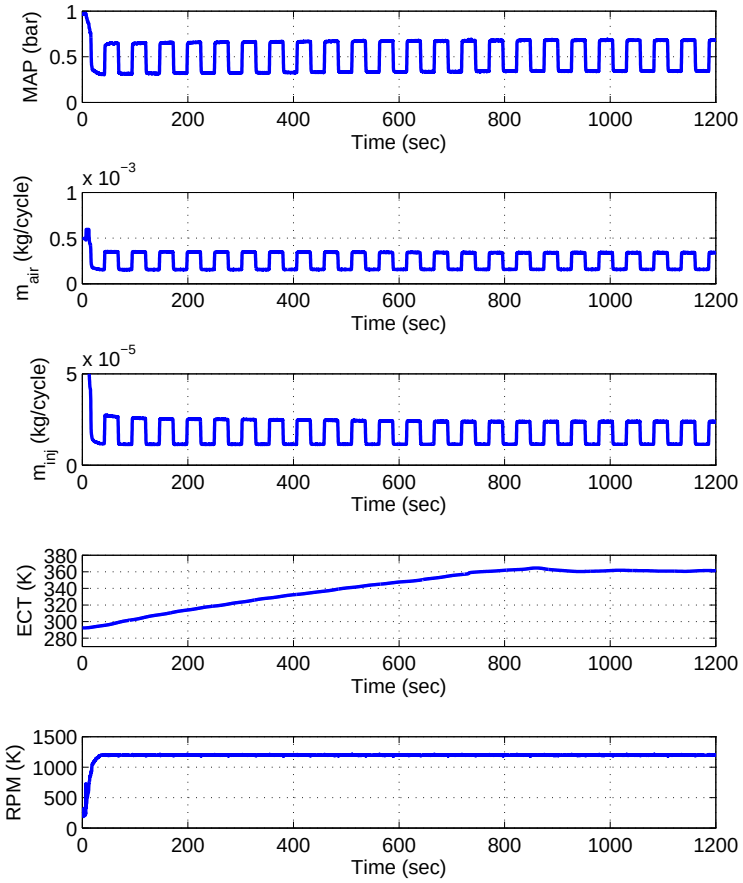

Figure 3.6 Fuel injected and other measurements from [10] used for the model inputs (E0)

Fig. 3.7 shows the simulated fuel puddle mass and ethanol mass fraction in the puddle for each fuel case. The lighter fuel components would vaporize faster than the heavier, so the puddle mass and composition would evolve in time. Fig. 3.7 shows that the model predicts different fuel puddle composition from the injected fuel.

Fig. 3.8-Fig. 3.10 show the simulated λ responses using the proposed model for E0, E22 and E85, respectively, compared with the experimental data measured by a UEGO sensor. The agreement between the simulations and the experimental data is quite reasonable. Model matching is especially very good for sufficiently warmed-up operations. The

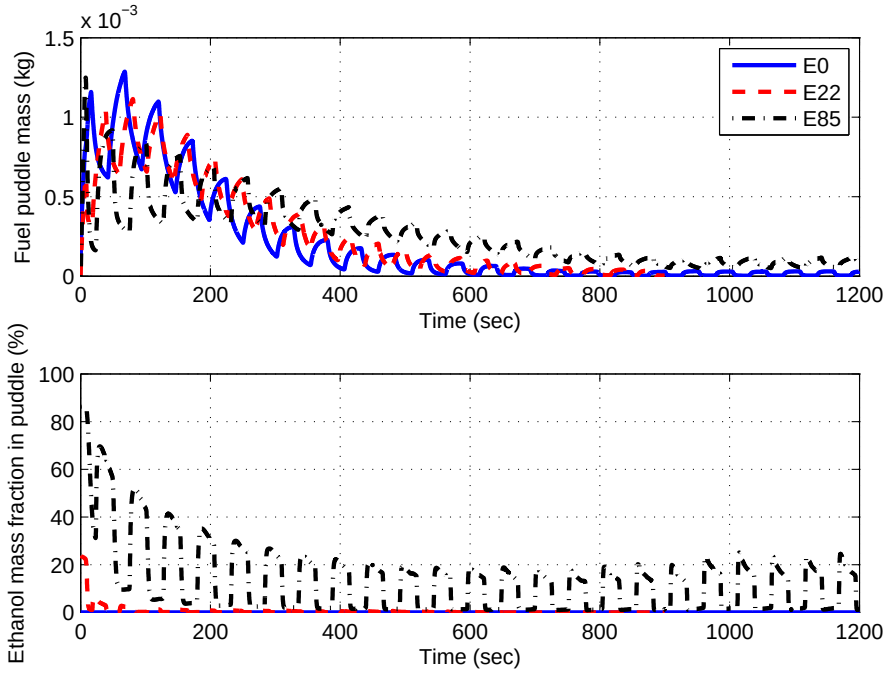

Figure 3.7 Simulated puddle mass and ethanol mass fraction in puddle for each fuel

model also predicts the overall decrease in magnitude of the λ excursions well. It also captures the asymmetric excursions due to tip-ins and tip-outs observed in the experimental data. The verification needs to be confirmed at more operating points to evaluate the model accuracy. However, the provided simulation and experimental results reasonably support the validity of the proposed model for at least some operating conditions.

3.7 Conclusion

In this chapter, a physics-based fuel puddle model that can be applied to any ethanol-gasoline mixture is developed. This model may be used for air-to-fuel ratio control in FFVs with engines equipped with port fuel injection. First, a multi-component fuel comprised of five chemical compounds is parameterized by ethanol content and is utilized to characterize gasoline-ethanol blends. The model consists of a droplet evaporation model and a single-puddle vaporization model. The droplet evaporation model is pre-simulated off-line to generate port wall-impacting factors of the injected multi-component fuel to be used in single-puddle. A single-puddle vaporization model is then utilized as a cycle-based model that may be simulated on-line to characterize the fuel puddle dynamics in port fuel injected engines. To verify the validity of the model, simulation results are compared with a limited number of experimental data.

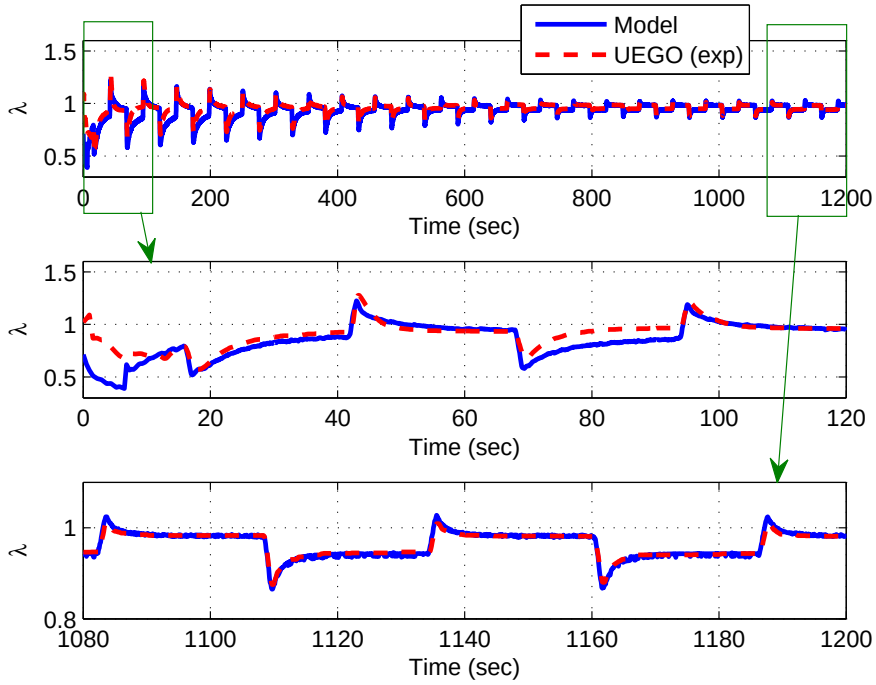

Figure 3.8 Simulated and experimental λ response for E0

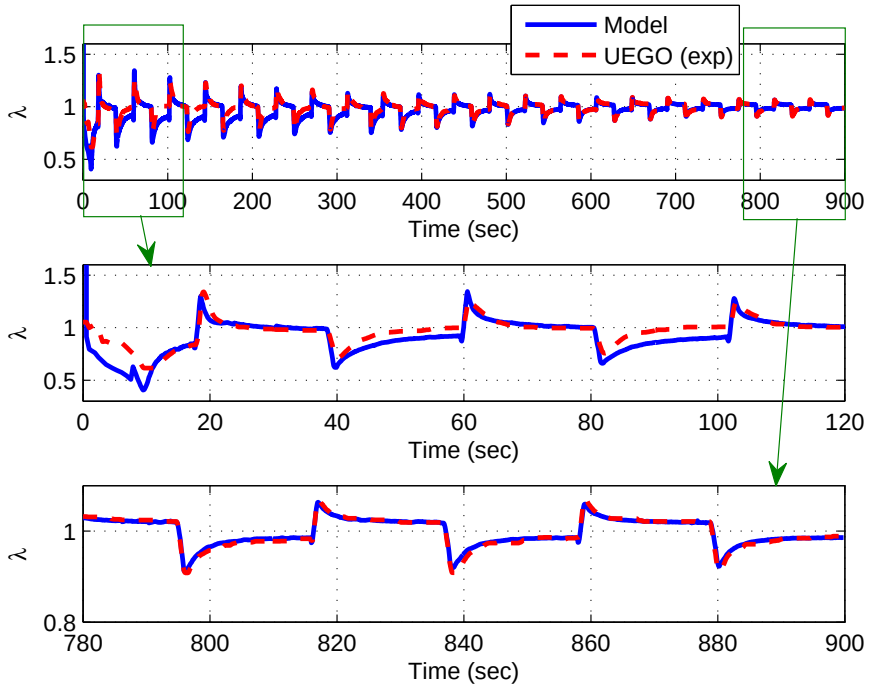

Figure 3.9 Simulated and experimental λ response for E22

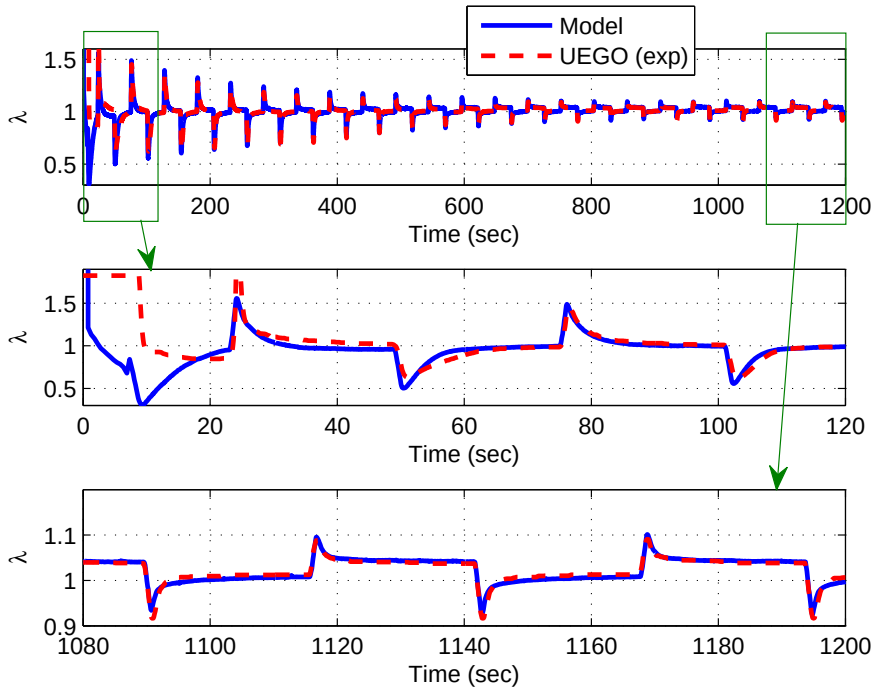

Figure 3.10 Simulated and experimental λ response for E85

Chapter 4
Transient Fuel Compensation

4.1 Introduction

The coupling between ethanol estimation and AFR regulation shown in chapter 2 demonstrated that the need for fast transient AFR response constrains ethanol content estimation gain, which then imposes slow ethanol adaptation. This creates a need for feedforward compensation of fuel puddle dynamics with an invertible puddle dynamics model for flex-fuel to minimize transient AFR excursions caused by throttle modulation. In chapter 3, we have developed a fuel puddle model that may be utilized to design a transient fuel compensator that improves transient performance of air-to-fuel ratio control around stoichiometry. In this chapter, a transient fuel compensator based on the fuel puddle model developed in chapter 3 is proposed. The compensator improves both performances of AFR regulation and ethanol content estimation.

Transient fuel compensation is realized by inverting the dynamics of the fuel film and injection. This means, for a linear fuel puddle model, cancellation of pole and zero in fuel puddle dynamics with zero and pole in TFC transfer function [8, 40]. However, direct inversion of pole-zero cancellation as in a linear model is not available for the nonlinear model developed in chapter 3. The transient fuel compensator in this chapter, therefore, utilizes a reasonable approximation to invert the model and consequently enable TFC. The TFC approximation is demonstrated with a simulation.

This chapter also provides various simulation results of AFR control and ethanol content estimation equipped with the transient fuel compensator designed in this chapter and the ethanol content estimator introduced in chapter 2. Simulation demonstrates that TFC actually enables faster fuel adaptation. Simulations are also performed with modeling errors in the fuel puddle model to show the robustness of AFR control and ethanol content estimation.

4.2 Transient Fuel Compensator

Transient fuel compensation is realized by inverting the dynamics of the fuel film and injection. This means, for a linear fuel puddle model, cancelation of pole and zero in fuel puddle dynamics with zero and pole in TFC transfer function [8, 40]. However, direct inversion of pole-zero cancelation as in a linear model is not possible for our fuel puddle model. To design a transient fuel compensator, the current fuel injection, $m_{inj}(k)$, should be expressed as a function of previous states, current output and other current inputs since current states are not available. To this end, (3.39) can be utilized. However, the term $\sum_{i=1}^{j} m_{evap,i}(k)$ is expressed involving complicated nonlinearity in $m_{inj}(k)$, hence causing difficulty in getting the inverted expression of $m_{inj}(k)$ given a desired fuel in the cylinder, $m_{f,cyl}^{des}(k)$. A reasonable approximation can be utilized to remedy this problem. First, let us express $m_{evap,i}(k)$ as follows using (3.37) and (3.31):

$$m_{evap,i}(k) = g_i(k) \cdot m_{p,i}^{IVO}(k), \tag{4.1}$$

where

$$g_i(k) \triangleq \min \left\{ 1,\ \bar{\alpha}(k) \frac{VP_i(k) \times m_p^{IVO}(k)}{\sum_i VP_i(k) \times m_{p,i}^{IVO}(k)} \right\}. \tag{4.2}$$

The normal vapor pressure of i-th component at the current step k, $VP_i(k)$, can be calculated using the current engine coolant temperature, $ECT(k)$, and the current ethanol content, $e(k)$. Using (4.1) and (3.24), (3.39) is then expressed as:

$$\begin{aligned} m_{f,cyl}(k) &= (1 - X(k)) \cdot m_{inj}(k) + \sum_{i=1}^{j} g_i(k) \cdot m_{p,i}^{IVO}(k) \\ &= \left(1 - X(k) + \sum_i g_i(k) \cdot X_i(k) \right) \cdot m_{inj}(k) \\ &\quad + \sum_i g_i(k) \cdot m_{p,i}(k-1), \end{aligned} \tag{4.3}$$

where the current total wall impacting fraction, $X(k)$, and the current wall impacting factor for each fuel component, $X_i(k)$, are obtained using the current ethanol content, $e(k)$, the current engine coolant temperature, $ECT(k)$, and the current manifold absolute pressure, $p_m(k)$. To eliminate dependency of $g_i(k)$ on $m_{inj}(k)$ in (4.3), we use a simplifying assumption that the composition of the fuel puddle is not affected significantly by the difference between the current injection, $m_{inj}(k)$, and the previous injection, $m_{inj}(k-1)$. This assumption is reasonable for a large puddle mass, when higher accuracy of a transient fuel

compensation is required. We can then approximate $g_i(k)$ in (4.2) as:

$$\hat{g}_i(k) = \min\left\{1,\ \hat{\tilde{\alpha}}(k)\frac{VP_i(k)\times \hat{m}_p^{IVO}(k)}{\sum_i VP_i(k)\times \hat{m}_{p,i}^{IVO}(k)}\right\}, \tag{4.4}$$

where

$$\hat{m}_{p,i}^{IVO}(k) = m_{p,i}(k-1) + X_i(k)\times m_{inj}(k-1), \tag{4.5}$$

$$\hat{m}_p^{IVO}(k) = \sum_{i=1}^{j} \hat{m}_{p,i}^{IVO}(k). \tag{4.6}$$

and

$$\hat{\tilde{\alpha}}(k) = 1-(1+\hat{B}_p(k))^{-\alpha(k)}. \tag{4.7}$$

In (4.7), $\alpha(k)$ can be calculated using the current inputs according to (3.29) and the approximation of the transfer number at the current step k, $\hat{B}_p(k)$, can be computed as:

$$\hat{B}_p(k) = \frac{\sum_i VP_i(k)\times \hat{f}_{p,i}(k)}{\widehat{PP}_{air}(k)\times M_{air}\times \sum_i \hat{f}_{p,i}(k)/M_i}, \tag{4.8}$$

where

$$\hat{f}_{p,i}(k) = \frac{\hat{m}_{p,i}^{IVO}(k)}{\hat{m}_p^{IVO}(k)}, \tag{4.9}$$

$$\widehat{PP}_{air}(k) = p_m(k) - \frac{\sum_i VP_i(k)\times \hat{f}_{p,i}(k)/M_i}{\sum_i \hat{f}_{p,i}(k)/M_i}. \tag{4.10}$$

Using the approximation, (4.4), the transient fuel compensation is then calculated from (4.3) as:

$$m_{inj}^{TFC}(k) = \frac{m_{f,cyl}^{des}(k) - \sum_i \hat{g}_i(k)\cdot m_{p,i}(k-1)}{1-X(k)+\sum_i \hat{g}_i(k)\cdot X_i(k)}, \tag{4.11}$$

where

$$m_{f,cyl}^{des}(k) \triangleq \frac{m_{air}(k)}{AFR_s(k)}. \tag{4.12}$$

One easier way to approximate $g_i(k)$ is to use previously calculated g_i in the puddle model so that $\hat{g}_i(k) = g_i(k-1)$ without recalculation of $\hat{g}_i(k)$ as above. This simpler approximation, however, results in poorer TFC performance. Fig. 4.1 shows the TFC simulation result to demonstrate the accuracy of our assumption and the approximation using (4.4)–(4.12). The simulation was done under the assumption that the plant follows the model perfectly and the states are known. A simulation using the model for E22 with inputs p_m, m_{air}, ECT

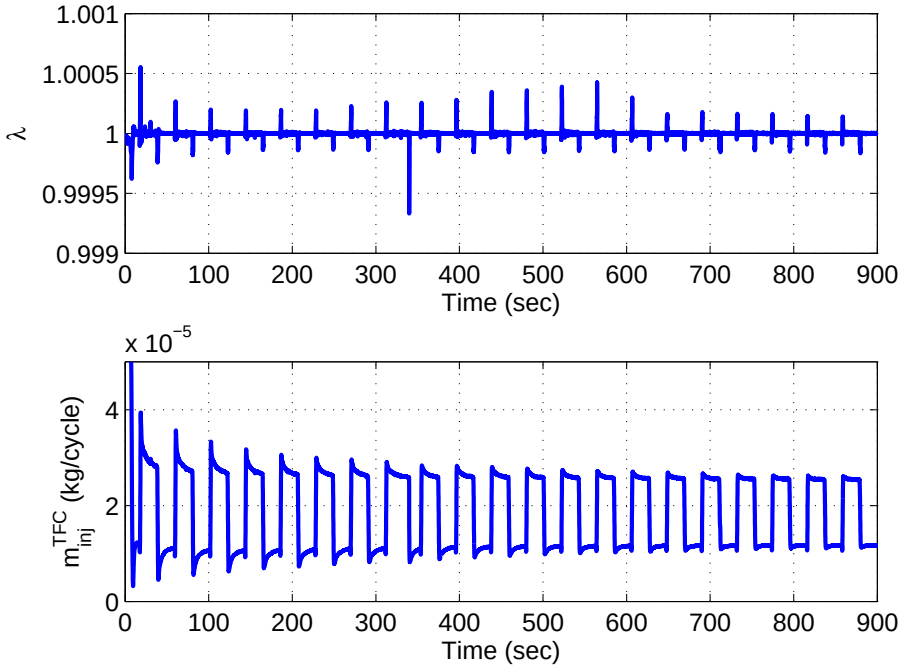

Figure 4.1 Simulation of the transient fuel compensation for E22

and N as prescribed in the experimental data used in section 3.6, and m_{inj} as prescribed from the proposed TFC in (4.4)–(4.12) tuned for E22 is shown in Fig. 4.1. The simulated λ trace shows several spikes due to the errors caused by the approximation but their amplitudes are negligible. This AFR accuracy is of course achieved only with very well tuned fuel puddle model parameters and known ethanol percentage.

4.3 Simulation

Simulations were performed to demonstrate performance enhancement of AFR control and ethanol content estimation by transient fuel compensation. Robustness is also demonstrated by introducing modeling errors in fuel puddle model used in TFC. Fig. 4.2 and Fig. 4.3 show two different system configurations used for simulations. Fig. 4.2 corresponds to the system of AFR control and ethanol content estimation without transient fuel compensator and Fig. 4.3 to the system with transient fuel compensator. Plant was simulated by the same manifold dynamics introduced by Crossley and Cook [18], which was used in previous simulation of chapter 2, together with fuel puddle model developed in chapter 3 with the same tuning values listed in Table 3.2 and the same wall-impacting factors used in chapter 3. Among the six inputs to the fuel puddle model, actual ethanol content e will be shown later, manifold absolute pressure p_m and air charge m_{air} are outputs of manifold dynamics

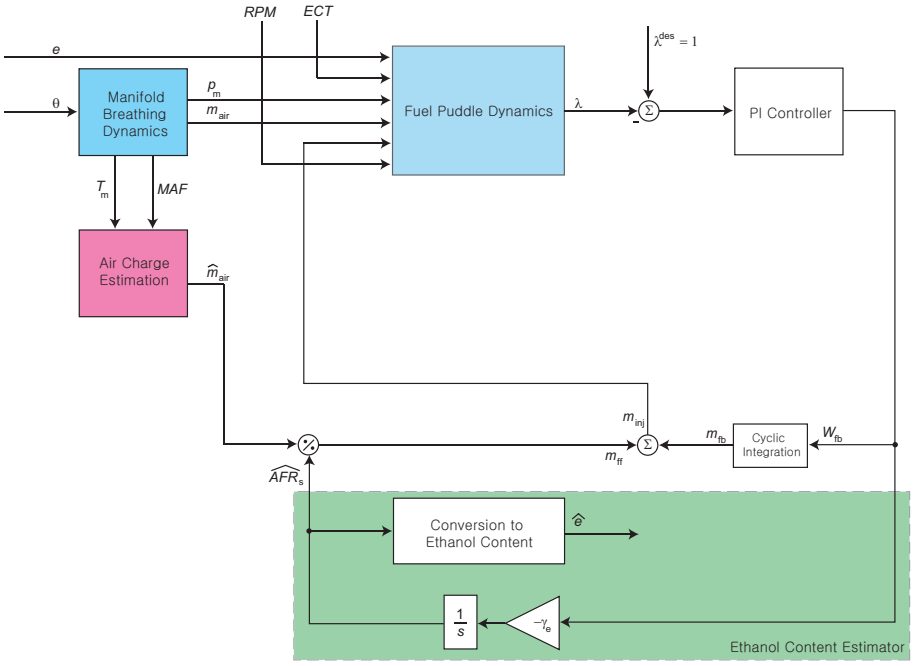

Figure 4.2 System configuration of AFR control and ethanol content estimation without transient fuel compensator

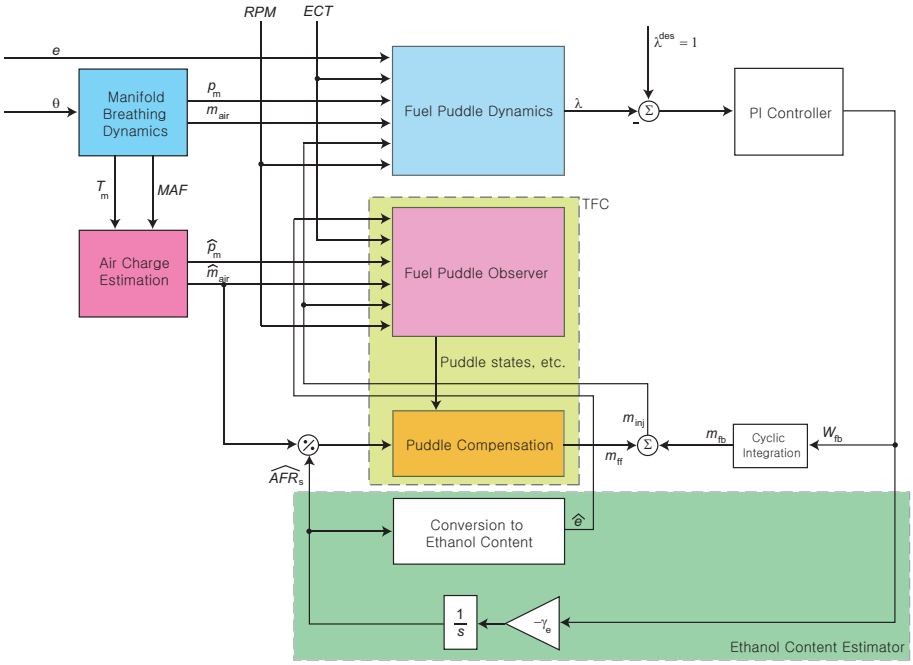

Figure 4.3 System configuration of AFR control and ethanol content estimation with transient fuel compensator

whose input is throttle angle which will be also shown later, the fuel injection m_{inj} is the controller output, and ECT and RPM are fixed to be:

- $ECT = 360\,\mathrm{K}$, $RPM = 2000$.

For a set of simulation with model errors, 10% error in tuning parameters and wall-impacting factors was simultaneously applied by multiplying 0.90 to ECT^0, σ, η_p, δ_{th} and X_i for all fuel component i for the fuel puddle model used as an open-loop fuel puddle observer in transient fuel compensator. For the λ feedback controller, a PI control with the same control gains as in chapter 2 is used:

- $\tau_{PI} = 0.3$, $k_{PI} = 0.0015$.

The ethanol content estimation gain is first chosen as the same value as used in chapter 2:

- $\gamma_e = 5000$.

If transient fuel compensator is used, the estimation gain can be increased because TFC improves λ regulation. Therefore, to show the improvement in ethanol content estimation, another ethanol content gain was also selected:

- $\gamma_e = 40000$.

In the following simulation result plots, the legend is marked with 'w/ high gain' if this high gain is associated with the simulation to distinguish the corresponding result from the result with the low gain. Simulations are done with no errors in air charge estimation and manifold pressure estimation.

Fig. 4.4 shows the simulation input. Throttle angles were modulated with a sequence of step changes and a ramp profile of real ethanol content change was applied. Initially the fuel used is gasoline and then it is changed to E85. Fig. 4.5 shows the change in the manifold absolute pressure and the air flow rate into the cylinder induced by the throttle modulation.

Fig. 4.6 and Fig. 4.7 show simulation results of ethanol content estimation and λ output. In Fig. 4.6, the transient excursions of ethanol content estimation caused by throttle modulation are observed when TFC is not activated ('w/o TFC w/o model error'). These excursions are eliminated when TFC is applied ('w/ TFC w/o model error'). The slow fuel adaptation changing from E0 to E85 is then overcome by increasing the estimator gain by virtue of TFC. The estimation plot associated with the high gain shows faster fuel adaptation. This case was also simulated with previously explained fuel puddle model error and shows several excursions in estimation affected by tip-ins and tip-outs. The excursions are,

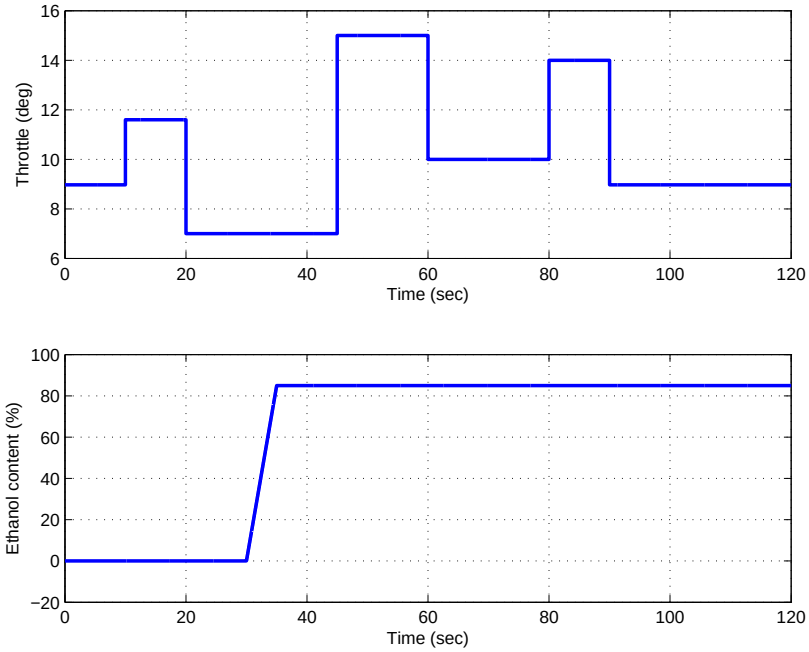

Figure 4.4 Simulation input

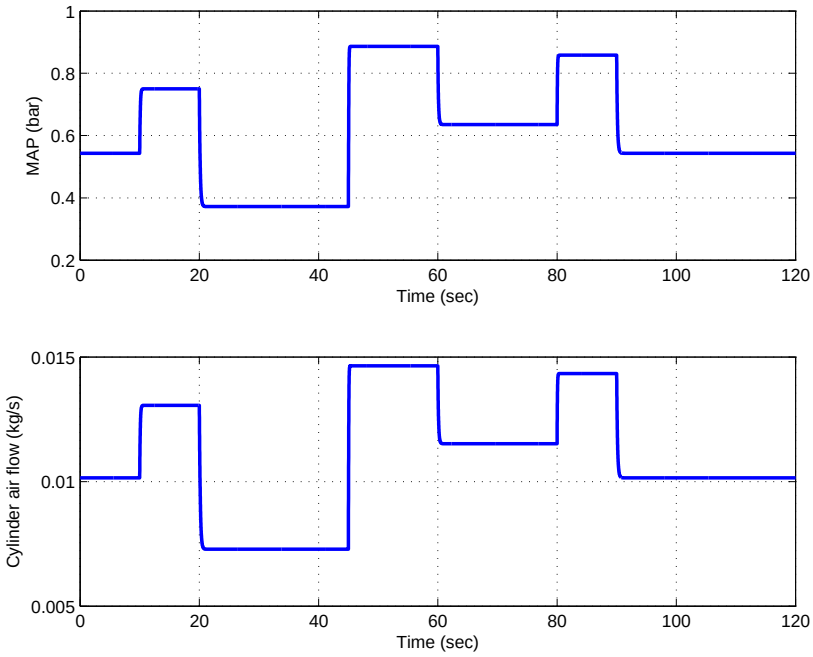

Figure 4.5 Manifold absolute pressure and air flow rate into the cylinder induced by throttle input

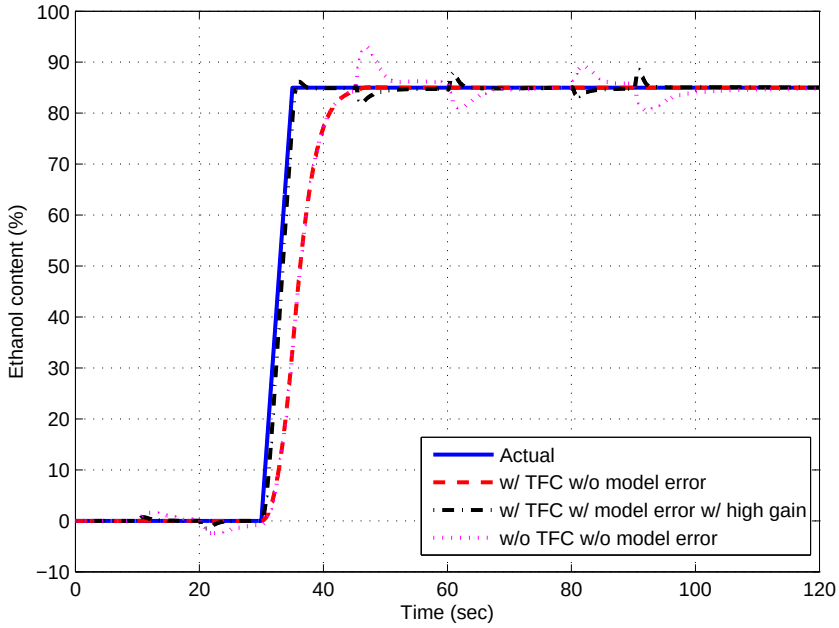

(a) Ethanol content estimation for the whole time span of the simulation

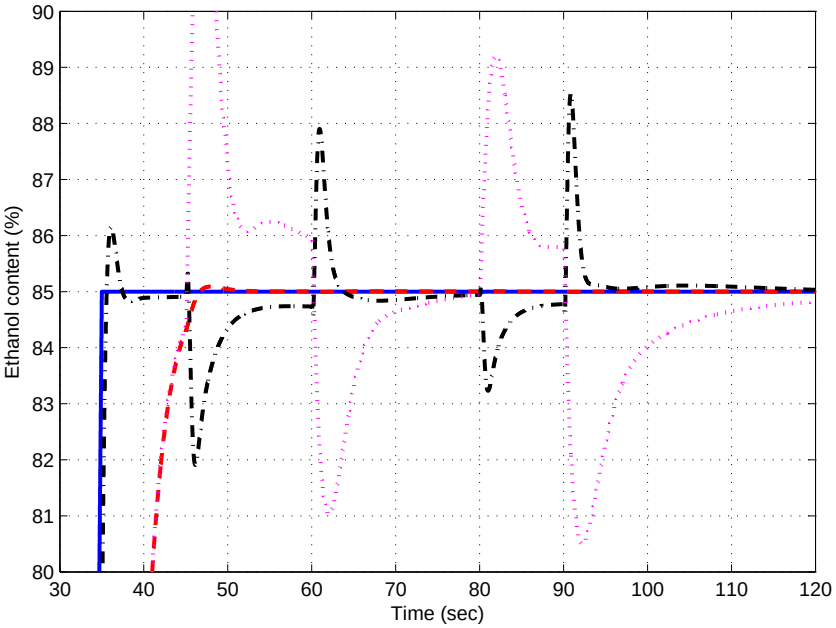

(b) Ethanol content estimation during 30-120 seconds

Figure 4.6 Simulated ethanol content estimation

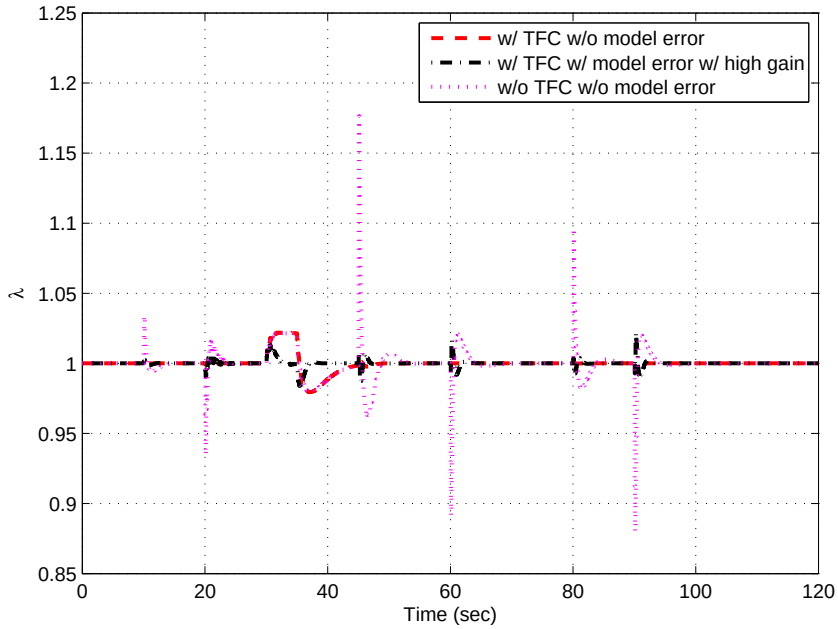

Figure 4.7 Simulated λ with TFC

however, reasonably small, hence demonstrating robustness in ethanol content estimation. In Fig. 4.7, λ excursions are drastically reduced by transient fuel compensation. Similarly to ethanol content estimation response, λ excursions caused by throttle modulation are completely removed by TFC when no modeling error is introduced. Even with modeling error, λ excursions are reasonably small, hence demonstrating robustness in AFR control. It is also observed that the transient λ response caused by change of ethanol content is improved when faster fuel adaptation is realized by the high estimator gain.

4.4 Conclusion

A transient fuel compensator using the fuel puddle model developed in chapter 3 is formulated. Since direct pole-zero cancelation is not available for the nonlinear model, an approximation is used to invert the model to design a TFC. The TFC approximation is demonstrated with a simulation. The transient fuel compensator improves the performance of both AFR control and ethanol content estimation. This performance enhancement is demonstrated by simulations. Robustness in AFR control and ethanol content estimation is also demonstrated by simulation with model error in the fuel puddle observer used in TFC.

Chapter 5

Ethanol Content Estimation during MAF Sensor Drifts

5.1 Introduction

Typically ethanol content estimation is initiated after detection of refueling. This estimation is achieved using an exhaust gas oxygen (EGO) sensor which calculates the air-to-fuel ratio (AFR) under the assumption of stoichiometric conditions given the closed loop control of fuel injection with the feedback of λ measurements. For example, an increased fuel ethanol content, hence decreased stoichiometric air-to-fuel ratio (SAFR) according to Table 1.1 would cause lean ($\lambda > 1$) EGO sensor measurement. Due to the feedback control, the fuel injection amount increases to reach again the stoichiometric condition ($\lambda = 1$). Because of the increased fuel amount, the AFR is calculated so that it is decreased. This decrease is recognized as decreased SAFR and hence interpreted as increased fuel ethanol content. The refueling event trigger is used to avoid misclassifying ethanol content variations as actuator faults (drifts) or component aging. The ethanol detection period needs to be as short as possible to reduce the probability of stopping the car and letting it cool down without a correct ethanol estimation having been established. This possibility is undesirable since the cold start depends heavily on correct ethanol estimation.

Since the ethanol content estimation relies on the AFR calculated using the cylinder air charge estimation and issued fuel amount, the ethanol estimation will erroneously compensate for the air charge estimation error and/or fuel injector error. Robust ethanol estimation with estimation of fuel injection error is provided in [6, 7] for flex-fuel direct injection (DI) engines equipped with in-cylinder pressure sensors. In this chapter, no fuel injector fault is assumed. The air charge estimation, on the other hand, depends on the mass air flow through the throttle body. Hence, a MAF sensor error results in steady-state ethanol content estimation error with high sensitivity. The high sensitivity problem has been discussed in section 2.8.

If the ethanol content or the stoichiometric AFR is known, the EGO sensor reading may be used in another adaptation against MAF sensor drift/bias in the same manner as used in ethanol content estimation. In other words, the calculated AFR can be used to update a parameter in the air charge estimation with respect to the fixed stoichiometric AFR. The use of EGO-based fuel feedback compensation to adapt the feedforward fuel compensation in response to errors in the inlet air sensing is now a common practice [14] referred as air charge adaptation. It is necessary to switch between two adaptations namely, the ethanol adaptation and the air charge adaptation, to avoid misclassifying ethanol content variations as sensor drifts or component aging. An appropriate switching logic using the tank refill trigger and relevant process characteristics should be devised for that purpose. However, this scheme may cause unobservable biases in estimations because every estimation is dependent on the true value of other estimations to guarantee convergence to its actual value. Convergence of estimations to actual values is important even though there are no true or reference values to which all estimations can be reset, once a vehicle leaves the factory or undergoes a major maintenance event unless the vehicle operates with known fuel. The estimation bias during regular field operation will be briefly discussed in section 5.2.

This chapter focuses on the cylinder air flow estimation under MAF sensor drift or bias using an intake manifold absolute pressure (MAP) sensor in order to prevent severe misestimation of ethanol content in flex fuel vehicles. The estimation scheme is independent of the exhaust gas oxygen sensor measurement which is used for ethanol content update via the closed loop regulation of stoichiometric condition. Therefore, the switching between this compensation of MAF sensor drift and the ethanol content estimation is not necessary and the associated estimation bias problem can be avoided. Simulations are performed to demonstrate the air flow estimation with compensation of MAF sensor drift using a MAP sensor realizing robust ethanol content estimation in flex fuel vehicles.

5.2 Switching Estimation Scenarios

Fig. 5.1 illustrates a simulated example of ethanol estimation with different estimator gains under the same operating scenarios. In the simulation, the fast estimation used the estimator gain $\gamma_e = 5000$ selected in section 2.6.2 while the slow estimation used $\gamma_e = 500$. The actual ethanol content changed from 10% to 85% and several throttle step changes were applied during the ethanol content change. No MAF sensor error was introduced in the simulation. This example illustrates the following problem associated with slow ethanol estimation. If the car has stopped (engine turned off) at the 60th sec or after 1/2 min of

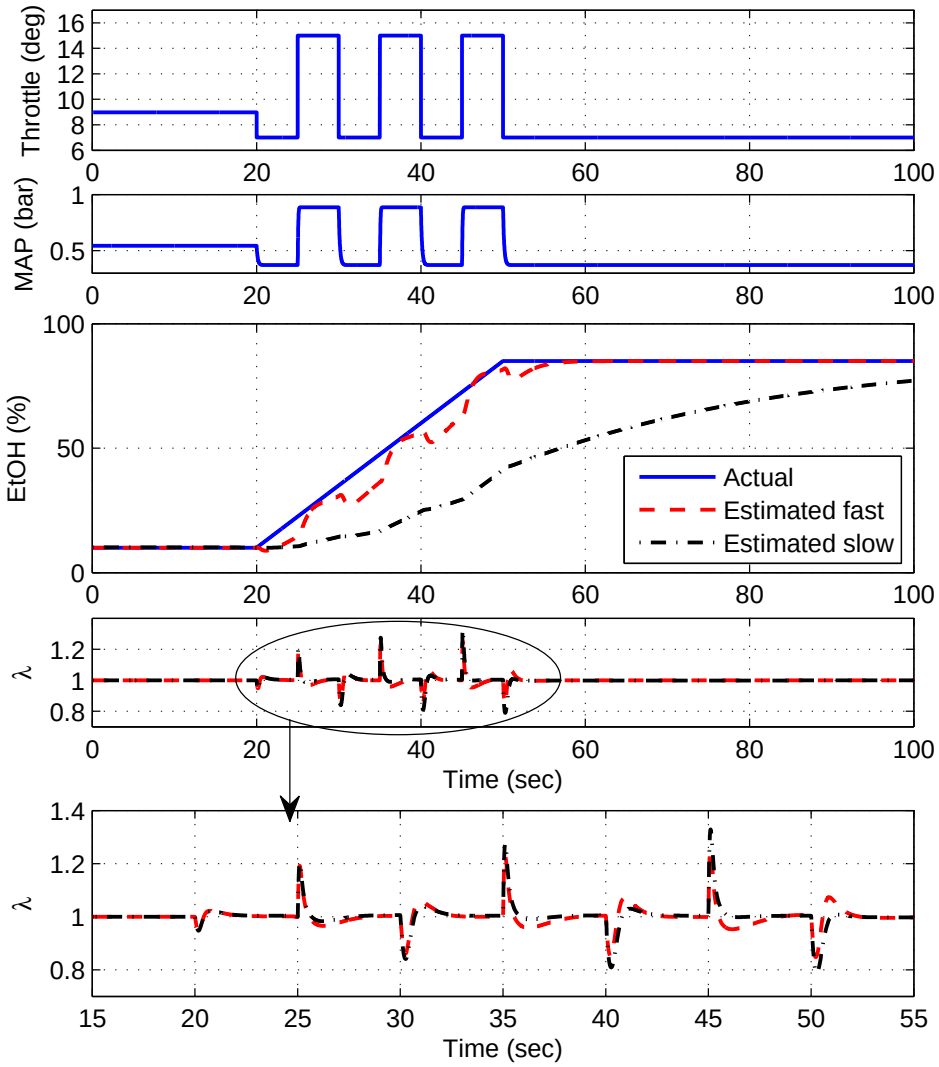

Figure 5.1 Simulated example of fast and slow ethanol estimations

running after refueling, the slow ethanol estimation would have had stopped with an E50 instead of E85 value. An example of such a stop immediately after refueling is fueling stations at a rest stop. Cold start with assumed E50 instead of the accurate E85 could have been a problem.

Fig. 5.2 shows a simulated example of conventional switching estimations of ethanol content and MAF sensor drift. In the simulation, the actual fuel changes between E20 and E60 are exaggerated to show qualitatively what would happen after many refueling. We also assume that the MAF sensor error fraction f_{ea} in section 2.8 drifts from 0 to -0.2. The switching variable α_e in Fig. 2.1 changed properly between 0 and 1, where $\alpha_e = 1$ selected the ethanol content estimation and $\alpha_e = 0$ the MAF sensor error fraction (or bias)

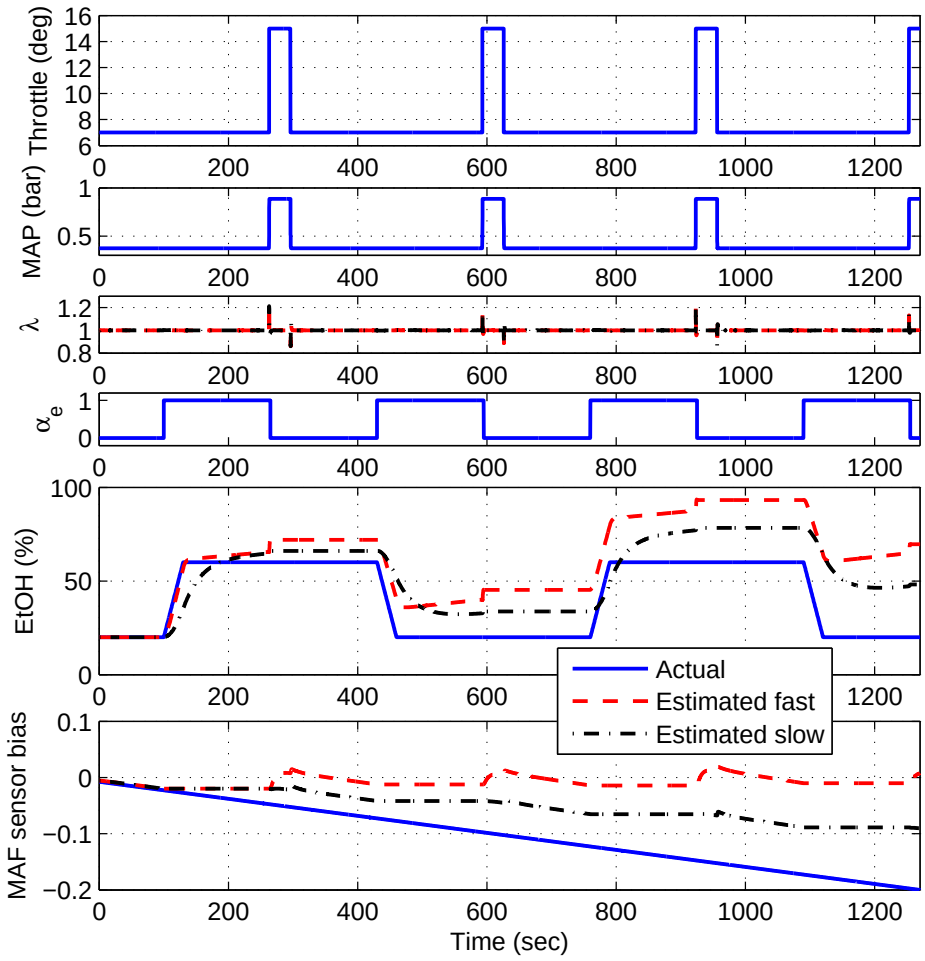

Figure 5.2 Simulated example of switching estimations of ethanol and MAF sensor drift with fast and slow ethanol estimations

estimation, respectively. Again, fast and slow ethanol estimations were simulated with the same operating scenarios. Let us first look at the estimation results in Fig. 5.2 associated with slow ethanol estimation. The MAF sensor drift occurring during the ethanol estimation periods is unobservable and it is incorrectly allocated in the ethanol estimation, hence the accuracy of the ethanol estimation is reduced proportionally to the duration of the estimation period.

As a solution, one would think that fast ethanol estimation is necessary to avoid the above problems by shortening the period of ethanol content estimation. However, speeding up the ethanol estimation introduces another problem from the strong interaction between throttle-induced λ excursions and ethanol estimation. This interaction is clearly shown in the ethanol estimation plot in Fig. 5.1 associated with fast ethanol estimation: the ethanol estimation shows distinguishable transient responses caused by throttle changes (or λ ex-

cursions). In the second example in Fig. 5.2, the estimation results associated with fast ethanol estimation is even poorer because the transient responses induced by the throttle changes were not accounted for at the transition moments from ethanol content estimation to MAF sensor drift estimation.

The solution to this problem would be a more comprehensive criterion for switching ethanol estimation on and off. The new switching criterion would involve monitoring throttle variability and switching between the two estimations only when steady-state driving has been achieved. This solution is practically equivalent with having a slow ethanol estimation with a longer ethanol estimation period where the MAF sensor drifts are unobservable and mis-allocated in estimated ethanol.

We propose a cylinder air flow estimation scheme independent of the ethanol estimation in the following sequel, where the MAF sensor drift is estimated using additional manifold absolute pressure measurements.

5.3 Speed-Density Method

In order to avoid problems in the switching adaptation discussed in section 5.2, the cylinder air flow should be estimated and account for the MAF sensor drift, independently of λ measurement. For this purpose, an intake manifold pressure sensor may be utilized. Using a manifold absolute pressure (MAP) sensor may be suitable in the sense that the associated cost is low. A conventional method from which the cylinder air flow can be calculated using MAP is the *speed-density* method:

$$W_{a,cyl} = \eta_v \frac{n_e}{2} V_d \frac{p_m}{RT_m}, \tag{5.1}$$

where p_m denotes the manifold absolute pressure, η_v is the volumetric efficiency, n_e is the engine speed (in rps) and V_d is the total displaced cylinder volume. Since η_v bears relatively high uncertainty, estimating cylinder air flow only using the MAP measurement via this equation is not a good idea. Therefore, we will still use the MAF sensor measurement and the drift will be compensated by the MAP measurement via the speed density equation. Note that any error fraction in MAP results in the same amount of error fraction in cylinder air flow from the nominal speed-density equation:

$$\frac{\delta W_{a,cyl}}{W_{a,cyl}} = \frac{\delta p_m}{p_m}, \tag{5.2}$$

where nominal speed-density equation assumes that the volumetric efficiency, η_v is independent of MAP, p_m, i.e., not a function of p_m, which is not strictly true in some real engines though. Therefore, the potential ethanol estimation error during MAP drift may not be worse than the ethanol estimation error during MAF drift. Moreover, MAP sensor accuracy is usually much better than MAF sensor accuracy [12, 13]. This fact justifies the idea of using MAP sensor to correct MAF sensor drift.

5.4 High Gain Observer for Input Estimation

The purpose of this section is to review the input estimation algorithm that will be used in subsequent sections for correcting MAF sensor drifts. Stotsky and Kolmanovsky have applied the following high gain observer technique to cylinder air charge estimation using a manifold pressure sensor [57]. Their work serves as a basis for the compensation of MAF sensor drift in this chapter.

We consider an input estimation problem arising from a first-order dynamic system:

$$\dot{z} = y + x, \tag{5.3}$$

where the signals z and y are measured, but x is a unknown time-varying input which has to be estimated on line. A high gain observer is defined in terms of auxiliary variables ε and v such that the estimation of x is given by

$$\hat{x} = \gamma z - v, \tag{5.4}$$

where

$$\varepsilon \triangleq \hat{x} - x = \gamma z - v - x \tag{5.5}$$

and v satisfies

$$\dot{v} = -\gamma v + \gamma y + \gamma^2 z. \tag{5.6}$$

Here γ is a positive observer gain. Evaluating the derivative of v along the solutions of system equation (5.5) one obtains

$$\dot{\varepsilon} = -\gamma\varepsilon - \dot{x}. \tag{5.7}$$

Assume now that $\dot{x}$ is bounded, i.e., that there exists a positive constant b_1 such that $\sup_t \|\dot{x}(t)\| \leq b_1$. Multiplying (5.7) by 2ε, and using an estimate $\|2\dot{x}\varepsilon\| \leq \dot{x}^2/\gamma + \gamma\varepsilon^2$ it

follows that $d\varepsilon^2/dt \leq -\gamma\varepsilon^2 + b_1^2/\gamma$ and the following transient bound for the estimation error is obtained,

$$\|\varepsilon(t)\| \leq \sqrt{\varepsilon(0)^2 e^{-\gamma t} + \frac{b_1^2}{\gamma^2}}. \tag{5.8}$$

Transient bound (5.8) implies that the upper bound on the estimation error for any $t > 0$ can be made arbitrarily small by increasing the design parameter $\gamma > 0$. Note that if one defines $\hat{z} = v/\gamma$, then (5.6) reduces to $\dot{\hat{z}} = -\gamma(\hat{z} - z) + y$. Thus $\hat{z}$ can be viewed as an estimate of z, provided $\gamma > 0$ is sufficiently large.

The same result can be obtained by filtering both sides of (5.3) with a low pass filter [57].

5.5 Estimation of Flow through the Throttle

5.5.1 MAF Sensor Dynamics Including Drift

The MAF sensor dynamics can be described by a first order lag [27]:

$$\dot{\overline{W}}_\theta = -\frac{1}{\tau_{MAF}}(\overline{W}_\theta - W_\theta), \tag{5.9}$$

where τ_{MAF} is the MAF sensor time constant, W_θ is the actual flow through the throttle, and $\overline{W}_\theta$ is the measured flow through the throttle by the MAF sensor.

The MAF sensor dynamics with drift can be modeled through a biased sensor gain:

$$\dot{W}_{\theta,n} = -\frac{1}{\tau_{MAF}}(W_{\theta,n} - W_\theta), \tag{5.10}$$

$$\overline{W}_\theta = (1 + C)W_{\theta,n}, \tag{5.11}$$

where $W_{\theta,n}$ is the mass air flow through the throttle body of the nominal system and C is a parameter that affects the MAF sensor gain.

The MAF sensor dynamics is then expressed as:

$$\dot{\overline{W}}_\theta = -\frac{1}{\tau_{MAF}}\left(\overline{W}_\theta - (1 + C)W_\theta\right). \tag{5.12}$$

5.5.2 Throttle Flow Estimation

To estimate the input, W_θ, the high gain observer previously discussed is utilized. Equation (5.12) is exactly (5.3) with $z = \overline{W}_\theta$, $y = -(1/\tau_{MAF})\overline{W}_\theta$ and $x = (1/\tau_{MAF})(1+C)W_\theta$. Thus, we apply the input observer, (5.6) and (5.4), to (5.12):

$$\dot{v}_f = -\gamma_f v_f - \frac{\gamma_f}{\tau_{MAF}}\overline{W}_\theta + \gamma_f^2 \overline{W}_\theta, \tag{5.13}$$

$$\widehat{W}_C = \tau_{MAF}(\gamma_f \overline{W}_\theta - v_f), \tag{5.14}$$

where W_C is defined as

$$W_C \triangleq (1+C)W_\theta, \tag{5.15}$$

$\widehat{W}_C$ is the estimation of W_C and γ_f is an observer gain. If we know the sensor drift C, from the adaptation in section 5.7, we can estimate W_θ:

$$\widehat{W}_\theta = \widehat{W}_C/(1+C), \tag{5.16}$$

where $\widehat{W}_\theta$ is the estimation of W_θ.

5.6 Estimation of Engine Cylinder Flow

This section restates the same observer design as discussed in [57], which utilizes an intake manifold absolute pressure (MAP) sensor to estimate the engine cylinder flow. The same observer can be effectively utilized to compensate for the volumetric efficiency variation caused by ethanol content variation in gasoline-ethanol blended fuel, regardless whether the variation is indeed large or not.

5.6.1 Manifold Filling Dynamics

The intake manifold filling dynamics is modeled as an isothermal intake manifold pressure model:

$$\dot{p}_m = \frac{RT_m}{V_m}(W_\theta - W_{a,cyl}). \tag{5.17}$$

A conventional technique for estimating the cylinder flow into a spark ignition (SI) engine involves a *speed-density* equation (5.1). The volumetric efficiency bears uncertainty and it may be calibrated by the engine dynamometer test. In any case, the cylinder air flow can

be viewed as a sum of nominal cylinder flow and an uncertainty term:

$$W_{a,cyl} = W_{cyl,n} + \Delta W_{a,cyl}, \tag{5.18}$$

with the nominal cylinder flow $W_{cyl,n}$ expressed as a function of MAP, p_m, engine speed, n_e, and possibly ethanol content in the fuel blend, e:

$$W_{cyl,n} = \mathscr{W}_{cyl,n}(p_m, n_e, e). \tag{5.19}$$

The intake manifold filling dynamics, (5.17), then becomes:

$$\dot{p}_m = \frac{RT_m}{V_m}(W_\theta - W_{cyl,n}) - \frac{RT_m}{V_m}\Delta W_{a,cyl}. \tag{5.20}$$

5.6.2 Cylinder Flow Estimation

Equation (5.20) is exactly the same as (5.3) with $z = p_m$, $y = \frac{RT_m}{V_m}(W_\theta - W_{cyl,n})$, $x = -\frac{RT_m}{V_m}\Delta W_{a,cyl}$. By applying the high gain observer, (5.6) and (5.4), to (5.20), the following input observer is obtained:

$$\dot{v} = -\gamma v + \gamma\frac{RT_m}{V_m}(W_\theta - W_{cyl,n}) + \gamma^2 p_m, \tag{5.21}$$

$$\widehat{\Delta W}_{a,cyl} = \frac{V_m}{RT_m}(v - \gamma p_m), \tag{5.22}$$

where $\widehat{\Delta W}_{a,cyl}$ is the estimation of $\Delta W_{a,cyl}$ and γ is an observer gain. The cylinder flow estimation is then expressed as:

$$\widehat{W}_{a,cyl} = W_{cyl,n} + (v - \gamma p_m)\frac{V_m}{RT_m}, \tag{5.23}$$

$$\dot{v} = -\gamma\frac{RT_m}{V_m}(\widehat{W}_{a,cyl} - W_\theta). \tag{5.24}$$

The intake manifold absolute pressure sensor is fast but may give noisy signals. A low pass filter can be utilized to filter out such noise. The isothermal intake manifold pressure model, (5.17), is used to avoid an excessive phase lag. Based on (5.17), a low pass filter can then be developed if W_θ and W_{cyl} are known:

$$\dot{\hat{p}}_m = \frac{RT_m}{V_m}(W_\theta - W_{a,cyl}) + \gamma_p(\bar{p}_m - \hat{p}_m), \tag{5.25}$$

where $\hat{p}_m$ is the estimated intake manifold absolute pressure and $\bar{p}_m$ is the measured pressure by the intake manifold absolute pressure sensor. Observers (5.24), (5.23) and (5.25) are combined to yield one observer scheme. In (5.24) and (5.23), the manifold absolute pressure, p_m, is replaced by the filtered manifold absolute pressure, $\hat{p}_m$. In (5.25), the cylinder flow, $W_{a,cyl}$, is replaced by the estimated cylinder flow, $\widehat{W}_{a,cyl}$. The combined observer is then summarized as:

$$\dot{v} = -\gamma\frac{RT_m}{V_m}(\widehat{W}_{a,cyl} - W_\theta). \tag{5.26}$$

$$\widehat{W}_{a,cyl} = \mathscr{W}_{cyl,n}(\hat{p}_m, n_e, e) + (v - \gamma\hat{p}_m)\frac{V_m}{RT_m}, \tag{5.27}$$

$$\dot{\hat{p}}_m = \frac{RT_m}{V_m}(W_\theta - \widehat{W}_{a,cyl}) + \gamma_p(\bar{p}_m - \hat{p}_m). \tag{5.28}$$

5.7 MAF Sensor Drift Adaptation

The drift parameter C needs to be known to obtain the estimation of the throttle flow, $\widehat{W}_\theta$, in (5.16). If we can estimate the cylinder flow, $W_{a,cyl}$, independently of the MAF measurement, the throttle flow, W_θ, can be estimated using (5.17) with MAP measurement. Equation (5.17) is exactly the same as (5.3) with $z = p_m$, $y = -\frac{RT_m}{V_m}W_{a,cyl}$ and $x = \frac{RT_m}{V_m}W_\theta$. Thus, we may apply the input observer, (5.6) and (5.4), to (5.17). The nominal cylinder flow equation, (5.19), may approximate the original speed-density equation (5.1) very well in a limited region of operating conditions. We then use the nominal cylinder flow in applying the input observer:

$$\dot{v}_n = -\gamma_n v_n - \gamma_n\frac{RT_m}{V_m}W_{cyl,n} + \gamma_n^2 p_m, \tag{5.29}$$

$$\widehat{W}_{\theta,\mathscr{W}} = \frac{V_m}{RT_m}(\gamma_n p_m - v_n). \tag{5.30}$$

Introducing a switching variable, α_s, the following drift parameter adaptation can be utilized:

$$\dot{\widehat{C}} = \gamma_C(\widehat{W}_C - (1+\widehat{C})\widehat{W}_{\theta,\mathscr{W}})\alpha_s, \tag{5.31}$$

where α_s is 1 in a limited region of operating conditions where the nominal cylinder flow equation is very good to approximate the original speed-density equation and is 0 elsewhere.

5.8 Combined Air Charge Adaptation Scheme

The observers discussed so far are combined to yield one observer scheme for cylinder air flow estimation. The throttle flow observer, (5.13), (5.14) and (5.16), the cylinder flow and manifold absolute pressure observer, (5.26), (5.27), (5.28) and the MAF sensor drift parameter observer, (5.29), (5.30) and (5.31), are combined replacing actual variables by estimated variables:

$$\dot{v}_f = -\gamma_f v_f - \frac{\gamma_f}{\tau_{MAF}}\overline{W}_\theta + \gamma_f^2 \overline{W}_\theta, \tag{5.32}$$

$$\widehat{W}_C = \tau_{MAF}(\gamma_f \overline{W}_\theta - v_f), \tag{5.33}$$

$$\widehat{W}_\theta = \widehat{W}_C/(1+\widehat{C}), \tag{5.34}$$

$$\dot{v} = -\gamma \frac{RT_m}{V_m}(\widehat{W}_{a,cyl} - \widehat{W}_\theta), \tag{5.35}$$

$$\widehat{W}_{a,cyl} = \widehat{W}_{cyl,n} + (v - \gamma \hat{p}_m)\frac{V_m}{RT_m}, \tag{5.36}$$

$$\dot{\hat{p}}_m = \frac{RT_m}{V_m}(\widehat{W}_\theta - \widehat{W}_{a,cyl}) + \gamma_p(\bar{p}_m - \hat{p}_m), \tag{5.37}$$

$$\widehat{W}_{cyl,n} = \mathscr{W}_{cyl,n}(\hat{p}_m, n_e, e), \tag{5.38}$$

$$\dot{v}_n = -\gamma_n v_n - \gamma_n \frac{RT_m}{V_m}\widehat{W}_{cyl,n} + \gamma_n^2 \hat{p}_m, \tag{5.39}$$

$$\widehat{W}_{\theta,\mathscr{W}} = \frac{V_m}{RT_m}(\gamma_n \hat{p}_m - v_n), \tag{5.40}$$

$$\dot{\widehat{C}} = \gamma_C(\widehat{W}_C - (1+\widehat{C})\widehat{W}_{\theta,\mathscr{W}})\alpha_s. \tag{5.41}$$

5.9 Steady State Analysis

The proposed 5th order observer uses MAP, MAF, n_e and an estimated ethanol content to derive a feedforward fuel calculated, $W_{ff1} = \widehat{W}_{a,cyl}/\widehat{AFR}_s$, that accounts for the MAF sensor drift. The estimated ethanol is still based on (2.5). We omit the stability analysis although this can be achieved using a Lyapunov-like function as in [57] or evaluating closed-loop observer eigenvalues of the linearized system for selection of the 5 available gains. In this section, we evaluate the proposed scheme and the errors it can introduce. Its potential drawbacks are highlighted in order to critically evaluate its potential contributions. For steady-state analysis, we assume that there is no noise in MAP measurement, i.e. $\bar{p}_m = p_m$. The calculation is straightforward by setting all state equations or all state derivatives to zero. In equilibrium computation, the state equation (5.41) is automatically

set to zero if $\alpha_s = 0$. From all state equations other than (5.41), the steady-state results are obtained:

$$W_\theta = W_{a,cyl}, \tag{5.42}$$

$$\overline{W}_\theta = \widehat{W}_C = (1+C)W_\theta = (1+C)W_{a,cyl}, \tag{5.43}$$

$$\hat{p}_m = p_m, \tag{5.44}$$

$$\widehat{W}_{a,cyl} = \widehat{W}_\theta = \widehat{W}_C/(1+\widehat{C}) = \overline{W}_\theta/(1+\widehat{C}) = \frac{1+C}{1+\widehat{C}}W_\theta = \frac{1+C}{1+\widehat{C}}W_{a,cyl}, \tag{5.45}$$

$$\widehat{W}_{\theta,\not W} = \widehat{W}_{cyl,n} = W_{cyl,n}. \tag{5.46}$$

The steady-state estimation errors are then:

$$\widetilde{W}_{a,cyl} = \widetilde{W}_\theta = \frac{\widehat{C}-C}{1+\widehat{C}}W_{a,cyl} = -\frac{\widetilde{C}}{1+\widehat{C}}W_{a,cyl}, \tag{5.47}$$

$$\tilde{p}_m = 0, \tag{5.48}$$

where estimation errors are defined as: $\widetilde{W}_{a,cyl} \triangleq W_{a,cyl} - \widehat{W}_{a,cyl}$, $\widetilde{W}_\theta \triangleq W_\theta - \widehat{W}_\theta$, $\widetilde{C} \triangleq C - \widehat{C}$ and $\tilde{p}_m \triangleq p_m - \hat{p}_m$. From (5.47), we can consider three different special cases.

1. If there is no steady-state error in drift parameter estimation ($\widetilde{C} = 0$), there is no error in cylinder air flow estimation in steady state:

$$\widetilde{W}_{a,cyl}\big|_{\widetilde{C}=0} = 0. \tag{5.49}$$

   This is a desirable result because our estimation purpose is to enhance accuracy of cylinder air flow estimation by correcting MAF sensor drift.

2. Even if there is no MAF sensor drift ($C = 0$), the proposed cylinder estimation will rely on the estimated sensor drift with following cylinder air flow estimation error in steady state:

$$\widetilde{W}_{a,cyl}\big|_{C=0} = \frac{\widehat{C}}{1+\widehat{C}}W_{a,cyl}. \tag{5.50}$$

   In this case, if MAF sensor drift compensation fails to estimate the actual value ($C = 0$) correctly, it may cause undesirable cylinder air flow estimation error which would not appear were it not for the drift compensation. Since the drift parameter estimation depends on the accuracy of the nominal cylinder flow expression, (5.19), and is not always activated according to the switching variable α_s, mis-estimation of the drift parameter is not negligible indeed.

3. If there is no MAF sensor drift compensation ($\widehat{C} = 0$), there is the following cylinder air flow estimation error in steady state:

$$\widetilde{W}_{a,cyl}\big|_{\widehat{C}=0} = -CW_{a,cyl}. \tag{5.51}$$

This case corresponds to use of a conventional cylinder flow estimation scheme without any compensation of MAF sensor drift. The estimation error of (5.51) results in amplified error in ethanol content estimation after all, hence motivating our drift compensation scheme discussed so far.

Equation (5.50) shows estimation performance degradation unnecessarily caused by using the estimation algorithm proposed in this chapter if there is actually no MAF sensor drift at all. However, (5.51) shows why the proposed algorithm is worth using if the MAF sensor drift is not actually negligible.

In a region of operating conditions where the nominal cylinder flow equation is a very good approximation of actual cylinder air flow, i.e., $\alpha_s = 1$, the following equilibrium equation holds from (5.41):

$$\widehat{W}_C = (1+\widehat{C})\widehat{W}_{\theta,\mathscr{W}}. \tag{5.52}$$

The following steady-state estimation results are then immediately obtained from (5.45) and (5.46):

$$\widehat{W}_{a,cyl} = \widehat{W}_\theta = W_{cyl,n}, \quad \widehat{C} = C + (1+C)\frac{\Delta W_{a,cyl}}{W_{cyl,n}}. \tag{5.53}$$

Steady-state estimation errors are then:

$$\widetilde{W}_{a,cyl} = \widetilde{W}_\theta = \Delta W_{a,cyl}, \quad \widetilde{C} = -(1+C)\frac{\Delta W_{a,cyl}}{W_{cyl,n}}. \tag{5.54}$$

If a cylinder flow equation perfectly fits to the actual cylinder air flow, i.e. $\Delta W_{a,cyl} = 0$, there will be no errors in cylinder air flow estimation and drift parameter estimation as shown in (5.54), i.e., $\widetilde{W}_{a,cyl} = 0$ and $\widetilde{C} = 0$.

5.10 Simulation

Simulation of cylinder air flow estimation under MAF sensor drift is performed in the configuration of AFR control with ethanol content estimation as shown in Fig. 2.1, where the air charge adaptation is now disconnected from the feedback signal W_{fb} or the λ measurement. Note that a measured intake pressure signal is additionally provided to the air charge

estimation block in Fig. 2.1 in this simulation. We use the same manifold breathing dynamics as provided in [18] and the cylinder block is simulated with a fuel puddle model developed for a port fuel injected (PFI) flex-fuel engine [3]. The puddle compensation block is realized by a transient fuel compensator using the fuel puddle model in [3]. In (5.11), the drift parameter C may actually vary very slowly around zero:

$$\overline{W}_\theta = (1 + C(t))W_{\theta,n},$$

In this simulation, the following first order drift model is utilized to give slow variation of drift parameter, $C(t)$:

$$\dot{W}_z = -\frac{1}{\tau_z}(W_z - W_\theta), \quad C = \bar{C}W_z,$$

where the drift time constant $\tau_z = 60$ sec and the drift gain $\bar{C} = 5.0$ sec/kg are used.

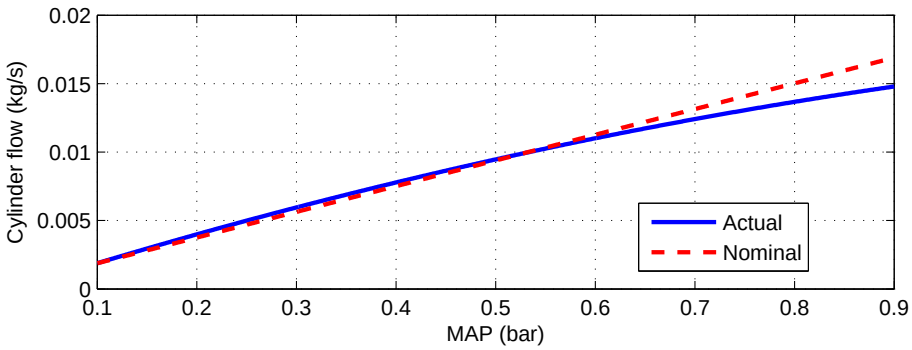

Figure 5.3 Cylinder air flow at 2000 RPM

Fig. 5.3 shows the cylinder air flow versus manifold absolute pressure, p_m, at a fixed engine rotation speed used in the simulation. The solid line is for the actual flow, $W_{a,cyl}$, and is used in the engine simulation, and the dashed line is the nominal flow, $W_{cyl,n}$, modeled by the nominal speed-density equation and used in the observer. This deviation emulates possible uncertainty in speed-density equation. Note that the nominal cylinder flow is close to the actual around $p_m = 0.5$ bar. Therefore, we assume that the known region of operation conditions for good speed-density approximation is around $p_m = 0.5$ bar for simulation.

Parameters and observer gains used in simulation are summarized in Table 5.1. These gains were tuned by looking at eigenvalues of the linearized closed-loop observer system matrix.

Fig. 5.4 shows simulated inputs, the throttle angle and the ethanol content. Throttle is modulated with a sequence of several step changes emulating tip-ins and tip-outs. The ethanol content is changed from zero to 85 % with a ramp profile and then it is changed to

Table 5.1 Parameters and observer gains used in simulation

Parameters	Value	Unit	Gains	Values	Unit
τ_{MAF}	0.02	sec	γ_f	27	sec^{-1}
$\frac{RT_m}{V_m}$	413.28	bar/kg	γ	9	
			γ_p	17	
$\eta_{v,n}\frac{V_d}{V_m}$	0.46554	cycle^{-1}	γ_n	5	
			γ_C	4	

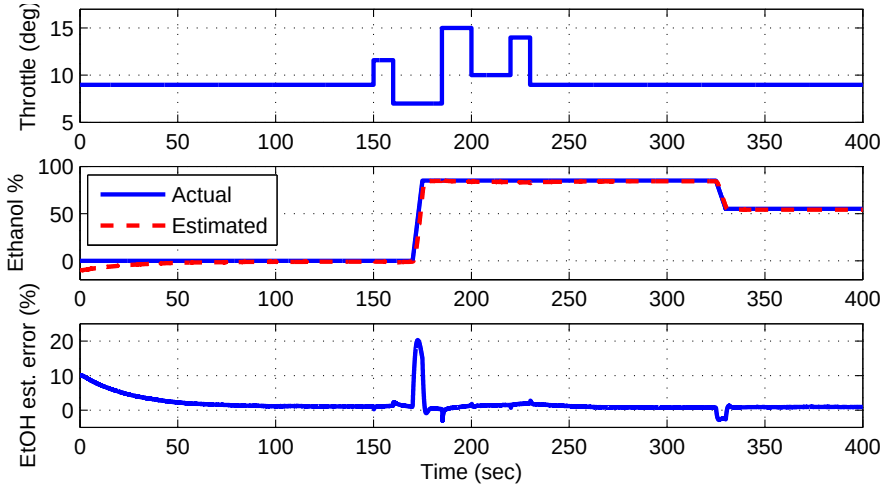

Figure 5.4 Simulated inputs and ethanol estimation error.

55 % later again with a ramp profile. The second plot also depicts the estimated ethanol content which is very sensitive to cylinder air flow estimation error. The third plot shows the ethanol content estimation error. We can observe that the steady-state error is quite allowable actually due to the improved estimation of cylinder air flow. The ethanol content estimation error reduces as time goes by in the first several seconds and this is due to the fact that the estimated drift parameter, $\widehat{C}$, converges closer to the actual as shown in Fig. 5.6.

Fig. 5.5 shows estimation results. MAP measurement is corrupted adding white noise to the simulated actual manifold absolute pressure. We can observe reduced noise level in the filtered pressure signal without much lag in Fig. 5.5(a). Performance of the throttle air flow estimation and the cylinder flow estimation is quite good. Nominally estimated signals, $\widehat{W}_{\theta,\mathscr{W}}$ and $\widehat{W}_{cyl,n}$, show big errors in operating conditions where the nominal speed-density equation suffers from large deviation from the actual.

Fig. 5.6 shows the drift parameter estimation and the switching variable α_s which changes according to operating conditions. Note that steady-state error in drift parame-

ter estimation remains even if α_s is set to 1 because the (nominal) modeled cylinder flow through the speed density equation differs from the actual cylinder air flow equation. The switching for this simulation is designed at 2000 engine rpm as:

$$\bar{\alpha}_s(t) = \begin{cases} 1 & \text{if } 0.4\,\text{bar} \leq \hat{p}_m < 0.6\,\text{bar} \\ 0 & \text{otherwise} \end{cases}, \tag{5.55}$$

$$\alpha_s(t) = \begin{cases} 1 & \text{if } \bar{\alpha}_s(\tau) = 1, \forall \tau \in [t-0.5, t] \\ 0 & \text{otherwise} \end{cases}, \tag{5.56}$$

to avoid chattering. Fig. 5.7(a) shows the λ output and Fig. 5.7(b) shows the controlled fuel injection results. The air-to-fuel ratio is regulated around stoichiometry. And the PI feedback signal enables the ethanol content estimation. We can observe that the total fuel injection and feedforward fuel injection increase in the interval of ethanol content change. Again, the ethanol content estimation is always possible as long as the feedback control is activated regardless of MAF sensor drift and uncertainty in speed-density equation. Nevertheless, the accuracy of the ethanol estimation is still degraded if an exact MAF drift compensation is not possible due to significant error in the speed density model with degradation of cylinder air flow estimation.

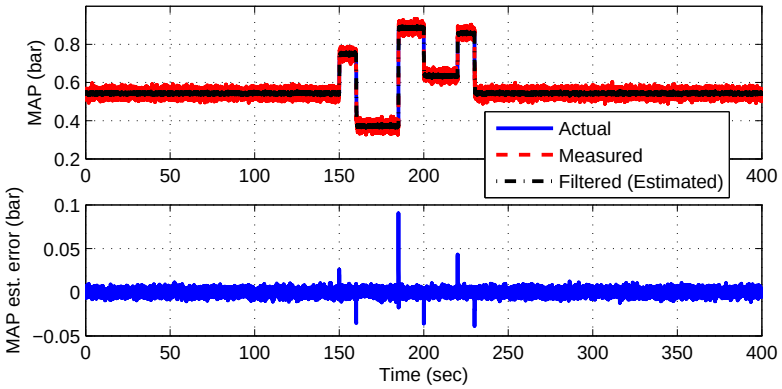

(a) MAP

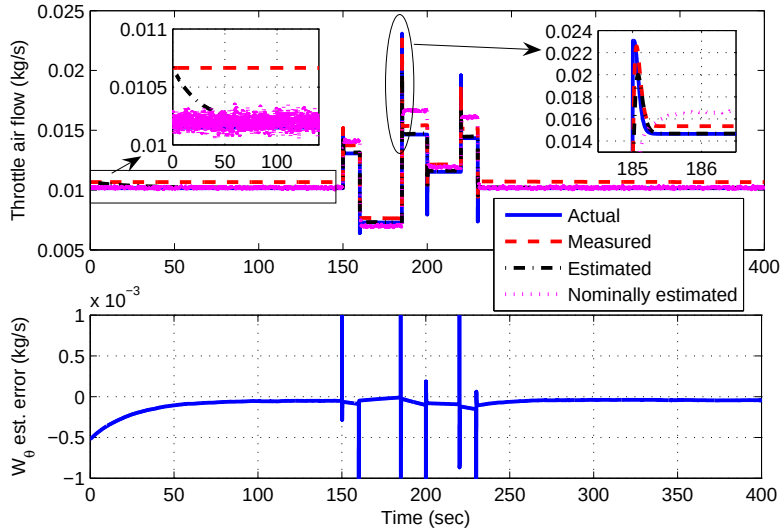

(b) throttle flow

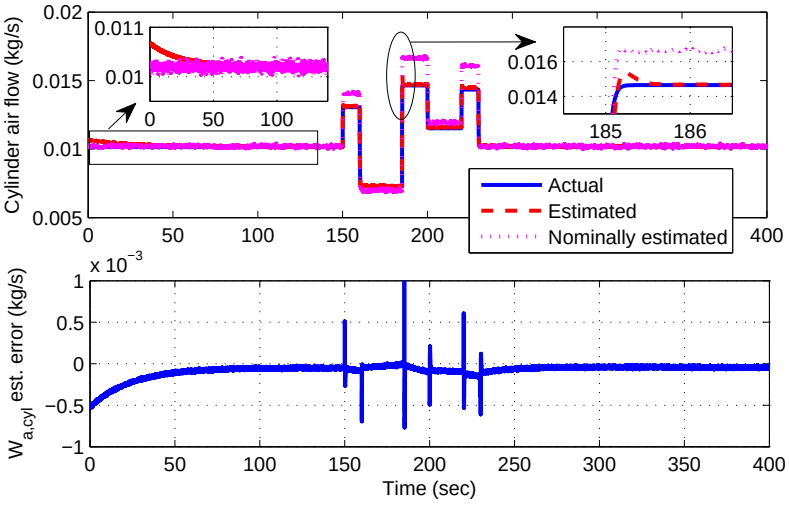

(c) cylinder air flow

Figure 5.5 Estimation result

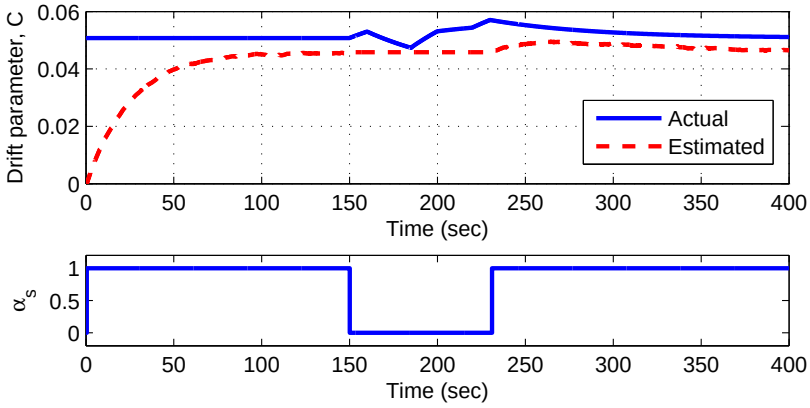

Figure 5.6 Drift estimation

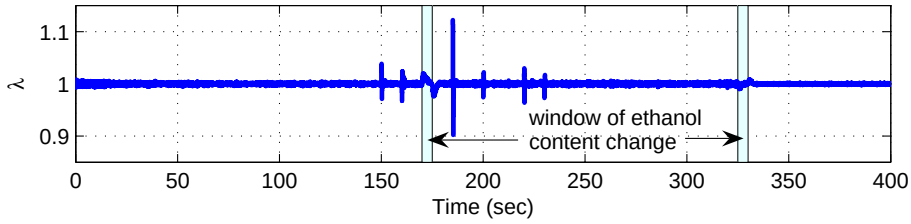

(a) simulated λ

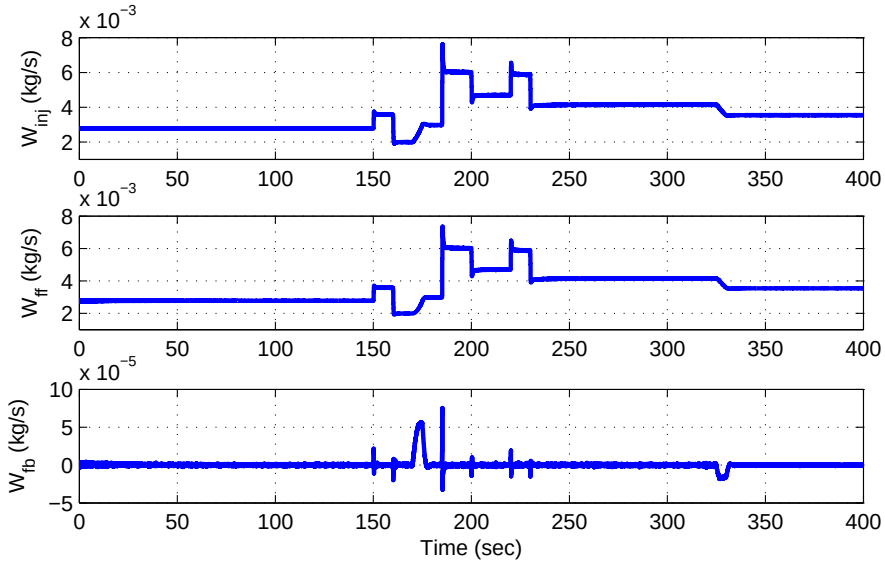

(b) simulated fuel injection

Figure 5.7 Simulated λ and fuel injection

5.11 Conclusion

In this chapter, a cylinder air flow estimation scheme that accounts for mass air flow sensor drift or bias is developed in order to avoid severe mis-estimation of ethanol content in flex fuel vehicles. The high sensitivity of the AFR-based ethanol content estimation to MAF sensor error suggests the need for robust compensation of the error and hence accurate estimation of cylinder air flow. First, we discuss the consequences, such as possible estimation biases resulting from switching between ethanol and cylinder air flow estimations using an EGO sensor. To obtain a more reliable cylinder air flow estimation by compensating for the MAF sensor drift, the intake manifold pressure sensor signal is utilized together with the speed density principle at selected operating regions. The proposed algorithm inevitably involves switching on the correction of MAF sensor drift at operating regions where there is high confidence that the speed density model has high accuracy. However, if an accurate reference engine map is available, the estimation bias problem can be alleviated in contrast to the switching adaptation case using the λ (EGO) sensor. Simulation is performed to demonstrate the air flow estimation with the compensation of MAF sensor drift using an intake manifold pressure sensor. In the simulation, the effect of the air flow estimation on the ethanol content estimation in flex fuel vehicles is shown with a realistic assumption of engine modeling accuracy.

Chapter 6

Fuel System Fault Tolerant Ethanol Content Estimation in Direct Injection Engines

6.1 Introduction

It is a common practice to estimate ethanol content based on the stoichiometric air-to-fuel ratio (SAFR). This ratio is identified through the closed-loop air/fuel regulation that is achieved by using the exhaust gas oxygen (EGO) sensor. SAFR-based ethanol estimation, however, is sensitive to fuel injector drifts [59], which occur as a result of typical deterioration over the life-time of the fuel system.

Due to the large ethanol estimation error associated with injector drift, the existing strategy in FFVs compensates for the drift by switching between the ethanol estimation and the fuel drift estimation. Specifically, the ethanol content estimation is generally triggered by the detection of a refueling event. Once the ethanol estimation reaches a steady-state value (does not change appreciably) or after a pre-determined period, the estimation for fuel injector drifts starts. This switching strategy of estimating two unknown variables, ethanol content and fuel injector drifts, uses information derived from the common exhaust gas oxygen (EGO) sensor and is prone to unobservable estimation biases [4].

An independent ethanol content estimation of the SAFR-based estimation by using the in-cylinder pressure measurements in direct injection (DI) engines was shown to be insensitive to the fuel injector drifts [6]. The use of cylinder pressure sensors for closed-loop combustion control might become more widespread in the future [37, 49, 66]. Therefore, its application to ethanol estimation and fuel system on-board diagnosis could demonstrate additional benefits of in-cylinder pressure sensing. This estimation scheme exploits the principle of charge cooling when fuel is directly injected into the cylinder once the valves are closed. As the ethanol content increases in the fuel, the charge cooling observed by

lower cylinder pressure should also increase because the latent heat of vaporization (LHV) is higher in ethanol than in gasoline. More specifically, the LHV-based detection feature (r) that quantifies the ethanol content in the fuel [43] is calculated from the in-cylinder pressure measurements of two consecutive cycles with the following different fuel injection modes:

- Single injection (Si) mode: All the commanded fuel is injected during the intake stroke; thus, even if the fuel is rich in ethanol, the charge cooling observed by cylinder pressure should be minimal.
- Split injection (Sp) mode: A fraction of the commanded fuel is injected during the intake stroke, and the rest is injected during the compression stroke after intake valve is closed. The fuel that is injected during the compression stroke contributes most of the cylinder charge cooling that is proportional to the ethanol content, and an associated pressure drop could be observed.

By comparing the cylinder pressure from the two modes, the charge cooling effect can be differentiated from the other thermo-physical phenomena and their effects on cylinder pressure evolution. The LHV detection feature is the quantity of this comparison.

The LHV-based detection feature provides an independent indication of the fuel ethanol content in addition to the SAFR-based detection feature under fuel injector drifts, and thus improves the robustness of SAFR-based ethanol detection strategy. However, as presented in [6], the correlation between the LHV-based detection feature and the fuel ethanol content cannot be perfectly modeled and it exhibits various errors at various operating conditions. Therefore, the methodology proposed in this chapter employs the LHV-based detection feature to correct the SAFR ethanol content estimation in the operation region where certain confidence levels and accuracies are satisfied. Due to the enhanced ethanol content estimation, more reliable injector fault detection is realized since the estimation of injector drift relies on accurate estimation of the ethanol content of the fuel. We demonstrate the applicability of the methodology via a simulation with slightly exaggerated injector drift occurring immediately after a refueling event that changes the ethanol content of the fuel. The simulation uses a realistic cycle-to-cycle variability and modeling error for the LHV-estimation. Therefore, the simulation is a good demonstration of the feasibility and potential benefits of the proposed algorithm. The integrated estimation algorithm is also validated with an engine dynamometer test.

6.2 LHV-Based Ethanol Estimation

A fault-tolerant ethanol estimation needs to account for drifts in the mass air flow sensor and the injectors. As the MAF sensor drifts can be corrected through [4], we only address the estimation of ethanol content and fuel injector drifts. Therefore, we need an extra equation which is independent from the λ regulation to account for both unknown ethanol content e and fuel amount W_f. The LHV-based ethanol detection feature in [43] calculated by the in-cylinder pressure measurements is utilized to provide this additional information in this chapter. The feature at the stoichiometric condition, r_s, should be then monotonic at a fixed known $W_{a,cyl}$ with respect to the change of the ethanol content e to solve e by inversion. The experimental data do not show the desirable monotonicity, introducing inevitable ethanol calculation errors. The monotone detection feature model is obtained by monotone regression of experimental data, where the ethanol content calculation error should be minimized.

Data have been collected from the experiments at near-stoichiometry on a 2.0L turbocharged spark ignition direct injection (SIDI) variable valve timing (VVT) engine equipped with Kistler 6125B in-cylinder pressure sensors as in [6]. Table 6.1 summarizes the nominal conditions for the experiments.

Table 6.1 Nominal experiment conditions

Description	Value
Relative AFR (λ)	1
Split injection ratio (Sp mode)	50/50 (%)
Start of 1st injection	105 CAdeg bBDC
End of 2nd injection (Sp mode)	40 CAdeg aBDC
Spark timing	MBT map for E0

At each nominal set point with different engine speed, load and ethanol content, the ethanol content and detection feature measurement data are averaged. The averaged data are regarded as the steady state data, as we are only interested in the steady state ethanol estimation error.

6.2.1 Affine Regression

At each engine speed and load, we want to build a suitable monotone regression model which maps the ethanol content e to the detection feature r_s and find the coefficients in the regression model by using the averaged data. The affine regression is utilized in this chapter. A higher order monotone function can be derived using [47] if more data with more set points are available. The following regression model is considered here:

$$r_s = r_s^{regr}(N, W_a, e) = a_1(N, W_a) + a_2(N, W_a)e, \tag{6.1}$$

where N and W_a denote the engine speed and the load, respectively. At each speed and load corresponding to an experimental set point, the coefficients a_1 and a_2 are resolved by the least squares fit using the averaged ethanol content and detection feature data. Since minimization of the ethanol calculation error is desirable, the standard least squares regression is actually applied to the inverse regression model of (6.1):

$$e^{regr}(N, W_a, r_s) = b_1(N, W_a) + b_2(N, W_a)r_s, \tag{6.2}$$

where $b_1 \triangleq -a_1/a_2$ and $b_2 \triangleq 1/a_2$. Once the coefficients a_1 and a_2 corresponding to several experimental set points are identified, those coefficient values provide a lookup table so that a_1 and a_2 at arbitrary speed and load can be determined by interpolation. On the other hand, the averaged detection feature at arbitrary operating condition, i.e., arbitrary speed, load and ethanol content can be calculated by multi-dimensional interpolation using the experimental data. Let us denote this interpolated feature by $r_s^{intp}(N, W_a, e)$. The steady state ethanol content estimate $\hat{e}_{ss,LHV}$ is then calculated by inverting (6.1):

$$\hat{e}_{ss,LHV}(N, W_a, e) = \frac{r_s^{intp}(N, W_a, e) - a_1(N, W_a)}{a_2(N, W_a)}. \tag{6.3}$$

Therefore, the steady state ethanol content estimation error under the LHV-based estimation $\tilde{e}_{ss,LHV} \triangleq e - \hat{e}_{ss,LHV}$ is expressed as:

$$\tilde{e}_{ss,LHV}(N, W_a, e) = e - \frac{r_s^{intp}(N, W_a, e) - a_1(N, W_a)}{a_2(N, W_a)}. \tag{6.4}$$

Fig. 6.1 shows the steady state ethanol content estimation $\hat{e}_{ss,LHV}$ at several loads for two different engine speeds. From the figure it is clear that the steady state LHV estimation performance could provide satisfactory accuracy only at certain limited speed and load conditions. At these operating points the LHV estimation could be used judiciously to

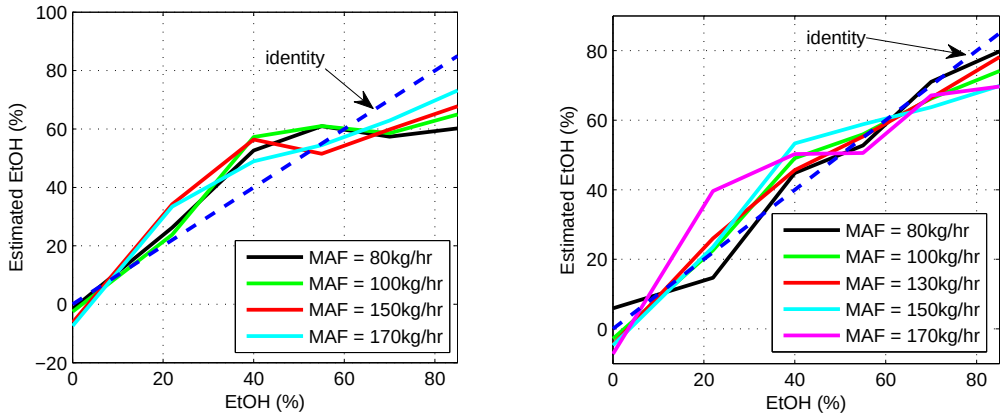

(a) engine speed of 2000 RPM (b) engine speed of 2500 RPM

Figure 6.1 The steady state ethanol content estimate $\hat{e}_{ss,LHV}$ vs. the actual ethanol content.

reduce large ethanol estimation errors due to unaccounted injector drifts.

6.2.2 Availability of LHV-Based Estimation

When the ethanol content estimation using the LHV-based detection feature is available, the fuel amount can also be estimated due to the stoichiometry constraint even under injector drifts. This simultaneous LHV-based estimation of both ethanol content and fuel injector drifts then depends on reliability of LHV-based ethanol estimation. However, there are certain operating conditions that such reliability is relatively degraded as shown in Fig. 6.1 and more reliable estimation depends on longer duration of nearly fixed operating conditions to avoid undesirable transient responses. It is also desirable that the period of activated alternative injection modes (Si and Sp) to obtain the LHV-based detection feature is minimized as the split injection mode sacrifices chance to enhance volumetric efficiency by charge cooling while the valves are closed at the second injection, although the activation/deactivation of the alternative injection mode is omitted in the following sequel. Therefore, the simultaneous estimation of ethanol content and fuel injector drifts is not achieved directly from the LHV-based estimation considering the occasional availability of the LHV-based estimation. We show below a design of the integrated SAFR and LHV-based estimations under fuel injector drifts that takes into account the LHV modeling error identified in this section.

6.3 Integrated Estimation Algorithm

The integration of the LHV and SAFR estimations relies on the λ feedback control loop regulating the fuel amount to match the stoichiometric level of the inducted cylinder air. Hence both estimations and hence their integration depends and affects the λ controller which is discussed below.

6.3.1 Relative Air-to-Fuel Ratio Controller

The relative air-to-fuel ratio (RAFR) controller is composed of feedforward and feedback:

$$W_{inj} = W_{ff} + W_{fb}, \tag{6.5}$$

where W_{inj} is the injector command, i.e., issued fuel flow, W_{ff} the feedforward command and W_{fb} the feedback command. The feedforward command is calculated to realize stoichiometric condition based on the estimated cylinder air flow and the fuel type considering the fuel injector shift as well:

$$W_{ff} = \frac{\widehat{W}_{a,cyl}}{\widehat{AFR}_s} \cdot \frac{1}{1+\hat{f}_{ef}}, \tag{6.6}$$

where $\widehat{W}_{a,cyl}$ denotes the estimated fresh air flow into the cylinder, $\widehat{AFR}_s$ the estimated stoichiometric air-to-fuel ratio (SAFR) depending on the estimated fuel ethanol content $\hat{e}$, i.e., $\widehat{AFR}_s = AFR_s(\hat{e})$, $\hat{f}_{ef}$ the estimated fuel injector shift, where the actual injector shift f_{ef} expresses how much mass fraction of issued fuel is additionally injected into the cylinder:

$$W_f = (1+f_{ef})W_{inj}, \tag{6.7}$$

where W_f denotes the actually injected fuel flow. The feedback controller is a proportional and integral (PI) controller:

$$W_{fb} = W_{fb,P} + W_{fb,I}, \tag{6.8}$$

where

$$W_{fb,P} = k_P(\bar{\lambda} - 1), \tag{6.9}$$

$$\dot{W}_{fb,I} = k_I(\bar{\lambda} - 1), \tag{6.10}$$

where k_P and k_I are the proportional and integral control gains, respectively and, $\bar{\lambda}$ is the measured λ.

6.3.2 Fuel Ethanol Content and Injector Shift Estimator

The fuel ethanol content e and the fuel injector shift f_{ef} are estimated by integrating the RAFR feedback control signal W_{fb}. However, both estimations cannot be simultaneously performed by commonly using the feedback signal W_{fb}, or the RAFR measurements $\bar{\lambda}$ [4]. Since the ethanol content change only happens during a certain period after refueling event, the estimation periods for ethanol content update and injector shift update could be divided using a switching signal which detects the ethanol content change period. The switching signal is denoted by α_e in this chapter. Enabling of α_e, i.e., setting $\alpha_e = 1$ happens at the refueling event or a bit later. Disabling of α_e, i.e., setting $\alpha_e = 0$ should happen after the ethanol content in the injected fuel has settled to a new value. An algorithm for enabling/disabling of α_e could be formulated along with the algorithms in this chapter. However, it is assumed that a robust algorithm for the switching signal α_e is provided *a priori* independent of the algorithms in this chapter. The ethanol content and fuel injector shift estimators are then expressed as:

$$\dot{\hat{e}} = \alpha_e L_e W_{fb}, \tag{6.11}$$

$$\dot{\hat{f}}_{ef} = (1 - \alpha_e) L_{inj} W_{fb}, \tag{6.12}$$

where L_e and L_{inj} are ethanol content and fuel injector shift estimator gains, respectively. Note that $\hat{e}$ and $\hat{f}_{ef}$ depends on each other. Therefore, as refueling events happen again and again, there could be biases in $\hat{e}$ and $\hat{f}_{ef}$ with respect to their actual values by any transient responses at switching, i.e., at the instant of changing α_e, and by the fuel injector drifts [4]. In order to prevent from too much estimation errors, the estimation should be reset with a more reliable value. In the following sections, the algorithms for the resetting will be proposed.

6.3.3 LHV-Based Ethanol Estimator

The steady state estimation of ethanol content using the LHV-based detection feature at the stoichiometric condition is insensitive to the fuel injection error as the injection command is not used in detection feature calculation in section 6.2, while that of the SAFR-based estimation is very sensitive to the fuel injection error as explained in section 2.8. Hence, if the

model (6.1) is sufficiently accurate in a region of operating conditions, a reliable estimation of fuel ethanol content is possible in that limited operation region by the LHV-based estimation. Therefore, the LHV-based ethanol content estimation could be used as a resetting value of the SAFR-based ethanol content estimation. The LHV-based ethanol estimator is given by:

$$\dot{\hat{e}}_{LHV} = L_{LHV}(\bar{r} - \hat{r}_s), \tag{6.13}$$

where L_{LHV} is the estimator gain, $\bar{r}$ the measured feature calculated by the in-cylinder pressure measurements, $\hat{r}_s$ the estimated detection feature from the regression model (6.1):

$$\hat{r}_s = r_s^{regr}(\overline{N}, \widehat{W}_{a,cyl}, \hat{e}_{LHV}), \tag{6.14}$$

where $\overline{N}$ denotes the measured engine speed and $\widehat{W}_{a,cyl}$ the estimated load or the estimated fresh air flow into the cylinder [4].

6.3.4 LHV-Based Estimation Reliability Examiner

Since the steady state LHV-based ethanol content estimate $\hat{e}_{ss,LHV}$ is accurate in limited operating conditions, the assessment of reliability on the LHV-based ethanol content estimate $\hat{e}_{LHV}$ should be performed by checking the history of operating conditions. First, let $\alpha_{op}(t)$ denote a flag indicating whether the operating conditions satisfy a certain level of reliability of the steady state estimation $\hat{e}_{ss,LHV}$ or not. For example, α_{op} can be designed as:

$$\alpha_{op} = \begin{cases} 1 & \text{if } \overline{N} \in [1900, 2100]\,\text{RPM and } \widehat{W}_{a,cyl} \in [170, 190]\,\text{kg/hr}, \\ & \text{or if } \overline{N} \in [2400, 2600]\,\text{RPM and } \widehat{W}_{a,cyl} \in [70, 140]\,\text{kg/hr}, \\ 0 & \text{otherwise}, \end{cases} \tag{6.15}$$

based on the estimation accuracy established offline in section 6.4. Second, let us define the following flag at time t, which tracks the recent history of α_{op}:

$$\alpha_{op,hist}(t) = \begin{cases} 1 & \text{if } \alpha_{op}(\tau) = 1, \forall \tau \in [t - t_{LHV}, t], \\ 0 & \text{otherwise}, \end{cases} \tag{6.16}$$

where t_{LHV} is a tuning parameter. Third, let $\alpha_{LHV}(t)$ denote a flag indicating whether the LHV-based ethanol content estimate $\hat{e}_{LHV}$ at time t is reliable or not. Since the LHV-based ethanol estimate $\hat{e}_{LHV}$ exhibits a dynamic response as it is filtered by (6.13), the flag α_{LHV}

depends on the history of α_{op} and is designed as:

$$\alpha_{LHV}(t) = (1 - \bar{\alpha}_e(t))\alpha_{op,hist}(t), \tag{6.17}$$

$$\bar{\alpha}_e(t) = \begin{cases} 1 & \text{if } \exists\tau \text{ such that } t \in [\tau, \tau + t_e] \text{ and } \alpha_e(\tau) = 1 \\ 0 & \text{otherwise} \end{cases}, \tag{6.18}$$

where $\alpha_e(t)$ is the flag associated with the switching between the ethanol estimation (6.11) and the fuel injector drift estimation (6.12) evaluated at time t and t_e is another tuning parameter. Larger value of t_{LHV} sets longer time span to allow longer transient period in $\hat{e}_{LHV}$ before enabling α_{LHV}, i.e., $\alpha_{LHV} = 1$. The parameter t_e is tuned so that the flag α_{LHV} is disabled ($\alpha_{LHV} = 0$) until the transient response of the LHV-based ethanol content estimation induced by the actual ethanol content change but not by the operating condition changes is removed.

6.3.5 Fault Detection

In normal steady state, the ethanol content estimate $\hat{e}$ and the LHV-based ethanol content estimate $\hat{e}_{LHV}$ should be sufficiently close. Therefore, the following ethanol content fault detection residual is defined:

$$s_e \triangleq \alpha_{LHV} \mid \hat{e} - \hat{e}_{LHV} \mid, \tag{6.19}$$

where $|\cdot|$ denotes the absolute value, and α_{LHV} is multiplied in order to take the transient responses into account. If the residual s_e is greater than a certain threshold, a fault should be triggered. Therefore, the fault trigger signal β_{flt} is designed as:

$$\beta_{flt} = \begin{cases} 1 & \text{if } s_e > e_{thld}, \\ 0 & \text{otherwise}, \end{cases} \tag{6.20}$$

where e_{thld} denotes a pre-determined threshold value. Once the fault trigger is enabled, the ethanol estimate $\hat{e}$ is gradually reset to $\hat{e}_{LHV}$, and then the fault trigger β_{flt} would eventually be set to zero again. This fault can be actually better understood and quantified as the fault flag α_{flt} which explicitly inspects the estimated fuel injector drift:

$$\alpha_{flt} = \begin{cases} 0 & \text{if } \hat{f}_{ef} \in [f_{ef,l}, f_{ef,h}], \\ 1 & \text{otherwise}, \end{cases} \tag{6.21}$$

where $[f_{ef,l}, f_{ef,h}]$ is the pre-determined range of allowable fuel injector drift. The fault flag α_{flt} could be displayed as a warning signal on the driver's front panel to inform that the maintenance service is required. Note that α_{flt} could be enabled with the normal function of the estimator (6.11) and (6.12) without ever triggering the resetting event.

6.3.6 Resetting

Immediately after the fault trigger β_{flt} is enabled, the LHV-based ethanol content estimate $\hat{e}_{LHV}$ is registered at a memory buffer and resetting of the ethanol content estimation $\hat{e}$ to $\hat{e}_{LHV}$ in the buffer is executed. If the estimated ethanol content is instantly reset to a new value calculated by the LHV-based estimation (6.13), the feedforward control signal (6.6) is abruptly reset as well, hence causing discontinuous RAFR control signal and undesirable transient response in λ. Therefore, the instant resetting of the ethanol content estimate requires resetting of the RAFR controller state so that the discontinuity in control signal is prevented. There could be still other control logic parts, however, which depend on the ethanol content estimate and could possibly show undesirable responses by the instant resetting. By this reason, we use gradual resetting of $\hat{e}$ to $\hat{e}_{LHV}$ in the buffer, which takes some time period starting at the moment of rising edge of β_{flt}, allowing all the control algorithms using the ethanol content estimate unchanged.

Fig. 6.2 shows the block diagram of the integrated algorithm proposed in this section.

6.4 Fault Detection Residual Threshold

Let $|\tilde{e}|^{max}_{ss,LHV}(N, W_a)$ denote the maximum absolute steady state ethanol content estimation error at the engine speed N and the load W_a under the LHV-based estimation:

$$|\tilde{e}|^{max}_{ss,LHV}(N, W_a) \triangleq \max_{e\in[0,0.85]} \mid \tilde{e}_{ss,LHV}(N, W_a, e) \mid, \tag{6.22}$$

where $\tilde{e}_{ss} \triangleq e - \hat{e}_{ss}$ denotes the ethanol content error in the steady state, with $\hat{e}_{ss}$ denoting the estimate of the ethanol content e in the steady state.

Lemma 1 *If the steady state fault detection residual $s_{e,ss}$ is greater than $2|\tilde{e}|^{max}_{ss,LHV}$, the steady state ethanol estimation performance is worse than that of the LHV-based estimation, i.e.,*

$$s_{e,ss} > 2|\tilde{e}|^{max}_{ss,LHV} \Rightarrow |\tilde{e}_{ss}| > |\tilde{e}_{ss,LHV}|. \tag{6.23}$$

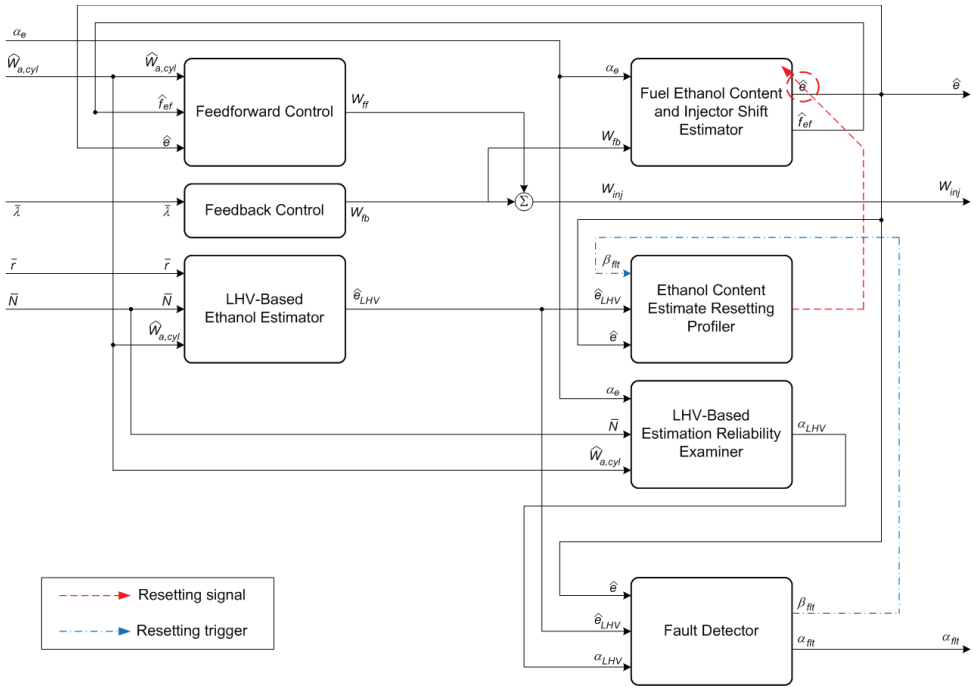

Figure 6.2 Block diagram of the integrated estimation algorithm.

Proof: By the definition of the fault detection residual s_e in (6.19), the following inequality holds in the steady state:

$$s_{e,ss} \leq \mid \hat{e}_{ss} - \hat{e}_{ss,LHV} \mid . \tag{6.24}$$

Applying the triangle inequality to the right side of (6.24),

$$\begin{aligned} \mid \hat{e}_{ss} - \hat{e}_{ss,LHV} \mid &= \mid \tilde{e}_{ss} - \tilde{e}_{ss,LHV} \mid \\ &\leq |\tilde{e}_{ss}| + |\tilde{e}_{ss,LHV}| \\ &= |\tilde{e}_{ss}| - |\tilde{e}_{ss,LHV}| + 2|\tilde{e}_{ss,LHV}| \\ &\leq |\tilde{e}_{ss}| - |\tilde{e}_{ss,LHV}| + 2|\tilde{e}|^{max}_{ss,LHV}. \end{aligned} \tag{6.25}$$

From (6.24) and (6.25),

$$|\tilde{e}_{ss}| - |\tilde{e}_{ss,LHV}| \geq s_{e,ss} - 2|\tilde{e}|^{max}_{ss,LHV}. \tag{6.26}$$

Therefore, if $s_{e,ss} > 2|\tilde{e}|^{max}_{ss,LHV}$, $|\tilde{e}_{ss}| - |\tilde{e}_{ss,LHV}| > 0$. ■

According to Lemma 1, the fault detection residual threshold e_{thld} should be specified within the upper bound $2|\tilde{e}|^{max}_{ss,LHV}$ as reaching the condition such that $s_{e,ss} > 2|\tilde{e}|^{max}_{ss,LHV}$

always results in worse steady state estimation performance than resetting the ethanol estimate by the LHV-based estimate.

If $\alpha_{LHV} = 1$ in the steady state, i.e., the LHV-based estimation is reliable in the steady state, since $\mid \tilde{e}_{ss} - \tilde{e}_{ss,LHV} \mid \leq e_{thld}$, the following inequality holds:

$$|\tilde{e}_{ss}| \leq |\tilde{e}_{ss,LHV}| + e_{thld}. \tag{6.27}$$

There are special considerations for choosing the fault detection residual threshold e_{thld}. On one hand a large value of fault detection residual threshold e_{thld} may increase the steady state estimation error $|\tilde{e}_{ss}|$ by delaying resetting even if the LHV estimation is deemed accurate enough and within reliable steady-state conditions when $\alpha_{LHV} = 1$ from (6.11)-(6.17).

On the other hand, a small value of e_{thld} may frequently cause additional estimation error by resetting. The additional error occurs due to the occasional large LHV estimation error. Hence, we need to allow resetting only if the two ethanol estimates (the current and the LHV) are alarmingly apart. As an extreme case, if $e_{thld} = 0$, then we will get $\tilde{e}_{ss} = \tilde{e}_{ss,LHV}$ when $\alpha_{LHV} = 1$. In this case, if the estimation error without resetting was actually zero, there is loss of estimation accuracy as $\tilde{e}_{ss,LHV}$. By the inequality on the steady state estimation error (6.27), the following bound regardless of the actual ethanol content e holds if $\alpha_{LHV} = 1$:

$$|\tilde{e}_{ss}| \leq |\tilde{e}|^{max}_{ss,LHV}(N, W_a) + e_{thld}(N, W_a). \tag{6.28}$$

Let us impose a universal bound on the inequality (6.28), as we want the steady state estimation error to be within certain bound regardless of the operating conditions:

$$|\tilde{e}_{ss}| \leq |\tilde{e}|^{max}_{ss,LHV}(N, W_a) + e_{thld}(N, W_a) \leq |\tilde{e}|^{bnd}_{ss}, \tag{6.29}$$

where the universal bound $|\tilde{e}|^{bnd}_{ss}$ is a tuning parameter. From (6.29) and the upper bound of e_{thld} derived from Lemma 1, $e_{thld} \geq 0$ is constrained with the upper bound:

$$e_{thld} \leq \min\left(|\tilde{e}|^{bnd}_{ss} - |\tilde{e}|^{max}_{ss,LHV}(N, W_a), 2|\tilde{e}|^{max}_{ss,LHV}(N, W_a)\right). \tag{6.30}$$

6.4.1 Probabilistic Reliability Examiner

The ethanol content estimation (6.11) provides the SAFR-based estimation if switching to the fuel injector shift estimation is always off, i.e., $\alpha_e \equiv 1$, which solely depends on the λ measurements without resetting by the LHV-based estimation. Let $\hat{e}_{SAFR}$ denote this SAFR-based estimation and $\hat{e}_{ss,SAFR}$ its steady state estimate. It is desirable that if

$\mid \hat{e}_{ss,SAFR} - \hat{e}_{ss,LHV} \mid$ is bounded by the residual threshold e_{thld}, a better steady state estimation is obtained by the SAFR-based estimation than by the LHV-based estimation more often. In other words, we want to find e_{thld} bounded by (6.30) such that the following conditional probability is maximized at each load and speed:

$$\begin{aligned} & P\left(\left(|\tilde{e}_{ss,SAFR}| \leq |\tilde{e}_{ss,LHV}|\right) \,\middle|\, \left(\mid \hat{e}_{ss,SAFR} - \hat{e}_{ss,LHV} \mid \leq e_{thld}\right) \right) \\ =& \frac{P\left(|\tilde{e}_{ss,SAFR}| \leq |\tilde{e}_{ss,LHV}|, \mid \hat{e}_{ss,SAFR} - \hat{e}_{ss,LHV} \mid \leq e_{thld}\right)}{P(\mid \hat{e}_{ss,SAFR} - \hat{e}_{ss,LHV} \mid \leq e_{thld})}. \end{aligned} \tag{6.31}$$

It is difficult to perform the double integration over the domain $\{(e, \tilde{e}_{ss,SAFR}) : e \in [0, 0.85], \tilde{e}_{ss,SAFR} \in (-\infty, \infty)\}$ which is required to evaluate the conditional probability (6.31). Instead, a geometric approximation is applied to evaluate (6.31) using discrete data points utilized in the detection feature regression. Although the details of approximation are not shown here, the approximated conditional probability is finally expressed as a function of the residual threshold e_{thld} at each speed and load, denoted as $l_p(N, W_a; e_{thld})$. By maximizing l_p at the given speed and load, within the threshold bound (6.30), the optimal threshold e^*_{thld} is then obtained. The optimal threshold is actually solely determined by $e^*_{thld} = \min(|\tilde{e}|^{bnd}_{ss} - |\tilde{e}|^{max}_{ss,LHV}, 2|\tilde{e}|^{max}_{ss,LHV})$ since l_p monotonically increases up to $e_{thld} = 2|\tilde{e}|^{max}_{ss,LHV}$ as shown in Fig. 6.3. However, the conditional probability evaluated at e^*_{thld}, l^*_p, is utilized in designing the LHV-based estimation reliability examiner, as larger value of l^*_p is required for more confidence on the LHV-based estimation reliability. Given a specific operating condition, the flag α_{op} should satisfy:

$$\alpha_{op} = \begin{cases} 1 & \text{if } l^*_p \geq l_{p,thld}, \\ 0 & \text{otherwise,} \end{cases} \tag{6.32}$$

where the probability threshold $l_{p,thld}$ is a tuning parameter defining the confidence level necessary for designing (6.15).

Fig. 6.3 shows the conditional probability l_p versus the residual threshold e_{thld} at two different operating conditions. With the universal bound $|\tilde{e}|^{bnd}_{ss} = 0.20$, the vertical dash dot line corresponds to $e_{thld} = |\tilde{e}|^{bnd}_{ss} - |\tilde{e}|^{max}_{ss,LHV}$ derived from the universal bound $|\tilde{e}|^{bnd}_{ss}$ and the vertical dash line corresponds to $e_{thld} = 2|\tilde{e}|^{max}_{ss,LHV}$ derived from Lemma 1.

Table 6.2 summarizes the computed residual threshold e^*_{thld}, the conditional probability l^*_p and the reliability flag α_{op} at different operating conditions corresponding to averaged data points collected from the experiment, with the tuning parameters $|\tilde{e}|^{bnd}_{ss} = 0.20$ and $l_{p,thld} = 0.70$. The discriminator α_{op} in (6.15) could be designed using Table 6.2. In the particular engine, it is possible to bound the ethanol estimation error by 20% and be 70%

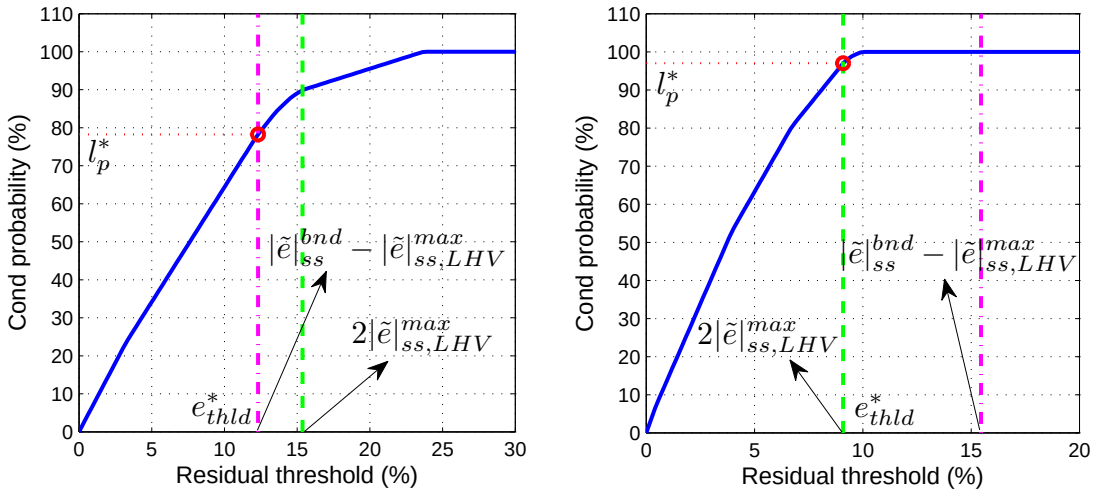

(a) engine speed 2000 RPM and MAF 176.2 kg/hr (b) engine speed 2500 RPM and MAF 127.1 kg/hr

Figure 6.3 The conditional probability l_p vs. the residual threshold e_{thld}.

confident that the standard SAFR estimation will improve using the developed integrated LHV estimation. The resetting event allows us simultaneously to check the expected injector shift and issue an injector maintenance alert if the drift exceeds some specified limits.

6.5 Simulation

Simulation of the proposed algorithm was performed with the turbo-charged SIDI VVT engine model in [34]. Since the fuel injector drifts and the estimation biases are the phenomena of very large time scale, an exaggerated engine operating scenario was simulated with fast ethanol changes and injector drifts within a compressed time window.

Step changes in the throttle input and the engine speed input were simulated as in Fig. 6.4(a) to create a dynamic environment emulating real engine operation. Fig. 6.4(b) shows the simulated load change induced by the throttle and speed inputs. A 5% bias in the mass air flow (MAF) sensor was actually introduced and the compensation algorithm in [4] was utilized for accurate cylinder air flow estimation so that we can concentrate on the ethanol estimation under the challenging scenario of injector drifts.

Fig. 6.5 shows the simulated estimation results. The actual ethanol content was simulated to change from 0 to 0.5 and the actual injector drift was simulated to change from 0 to 0.2 while large amount of drift is introduced during the ethanol estimation period when the drift estimation is off ($\alpha_e = 1$) in order to cause good amount of estimation errors

Table 6.2 Residual threshold and LHV-based estimation reliability tuning matrix with $|\tilde{e}|_{ss}^{bnd} = 0.20$ and $l_{p,thld} = 0.70$.

Engine speed of 1500 RPM

MAF (kg/hr)	62.5	79.7	99.6
e^*_{thld} (%)	9.5	8.2	9.0
l^*_p (%)	47.5	43.8	46.3
α_{op}	0	0	0

Engine speed of 2000 RPM

MAF (kg/hr)	84.1	103.6	152.8	176.3
e^*_{thld} (%)	1.3	4.3	6.4	12.3
l^*_p (%)	6.3	20.5	29.2	78.3
α_{op}	0	0	0	1

Engine speed of 2500 RPM

MAF (kg/hr)	82.3	106.2	127.1	150.2	167.8
e^*_{thld} (%)	11.8	10.7	9.1	8.2	6.8
l^*_p (%)	90.8	71.8	97.0	51.7	33.2
α_{op}	1	1	1	0	0

in short time. After the ethanol estimate is reset as the LHV-based estimation is determined to be reliable, the injector drift estimation converges close to the actual value as the ethanol estimate is more accurate than before by resetting. For the gradual resetting of the ethanol content estimate, a quintic polynomial profile in time was utilized with 15 seconds of resetting period.

Fig. 6.6 shows the simulated absolute ethanol content estimation error and the simulated fault detection residual. Resetting occurs as the fault detection residual s_e in (6.19) becomes greater than the pre-determined threshold when the estimation difference is sufficiently large with $\alpha_{LHV} = 1$.

Fig. 6.7 shows the system flags. First the refueling flag $\alpha_e = 1$ initiates the SAFR ethanol estimation algorithm (6.5)-(6.11) which stops at the 160th second. Due to the large injector shift (introduced unrealistically fast here for demonstration purposes) the difference between the estimated ethanol and the LHV-prediction $|\hat{e} - \hat{e}_{LHV}|$ grows beyond the

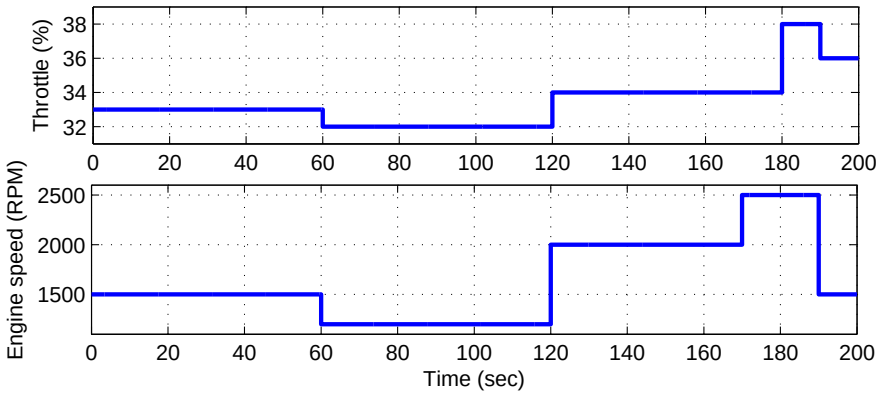

(a) simulated throttle and engine speed

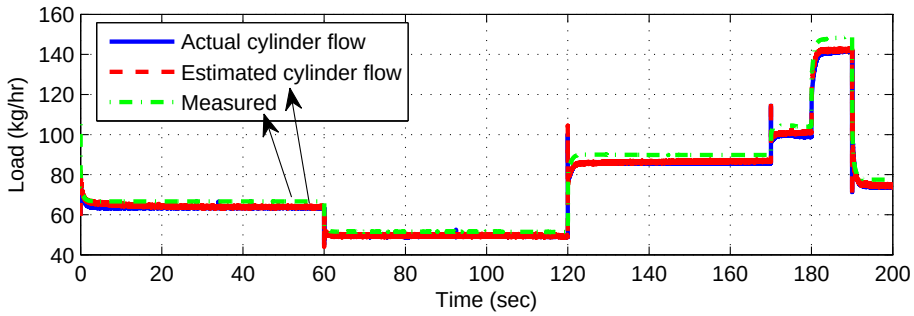

(b) simulated load

Figure 6.4 Simulated throttle and speed inputs and induced load.

ethanol fault detection threshold $e_{thld} = 20\%$ as early as the 142nd second, but the resetting flag β_{flt} is triggered much later. The resetting flag β_{flt} turns on at the 175th second when, in addition to the large difference between the two ethanol estimations $\hat{e}$ and the $\hat{e}_{LHV}$, the engine operates under conditions with high confidence levels for the accuracy of the LHV estimation $\hat{e}_{LHV}$. Indeed at the 170th second the engine speed is raised to 2500 rpm and the concurrent load satisfies the reliability examiner flag α_{op} in (6.15) as calculated by Table 6.2. After 5 seconds any possible transient effects can be neglected and the reliability history is long enough to trigger the ethanol detection fault flag β_{flt}.

The injector fault is reported ($\alpha_{flt} = 1$) at around 188 sec as the estimated injector drift $\hat{f}_{ef}$ from (6.5)-(6.12) using the reset value of the ethanol content estimate grows out of the allowable range, $[-0.15, 0.15]$ in this simulation. Note that the actual injector fault has occurred much earlier as the actual drift is out of the allowable range as early as the 155th second also shown in Fig. 6.5. Were it not for resetting based on the proposed algorithm, even this late report and possible maintenance alert would not be possible as large ethanol estimation errors would continue to accumulate causing potentially annoying startability

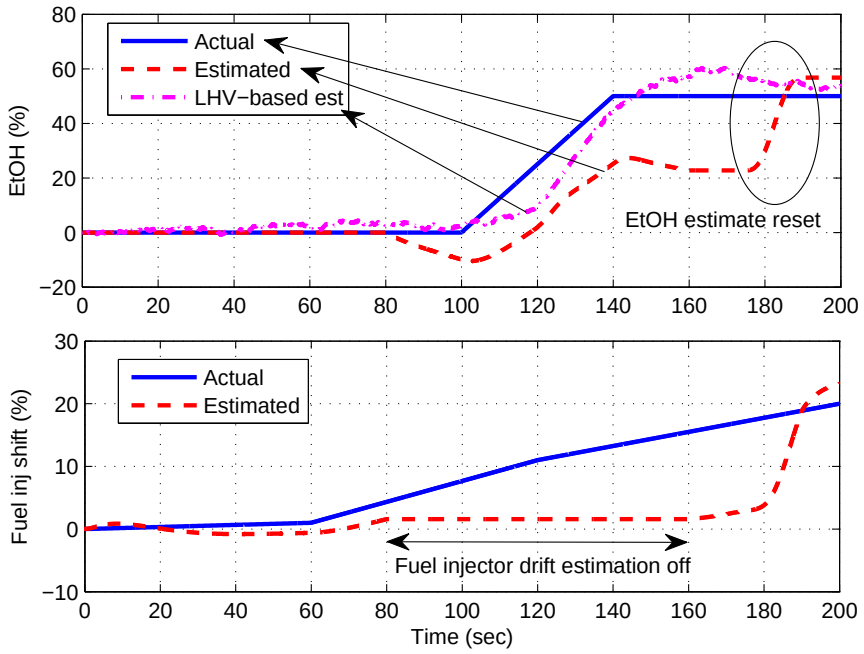

Figure 6.5 Simulated ethanol content and fuel injector drift estimations.

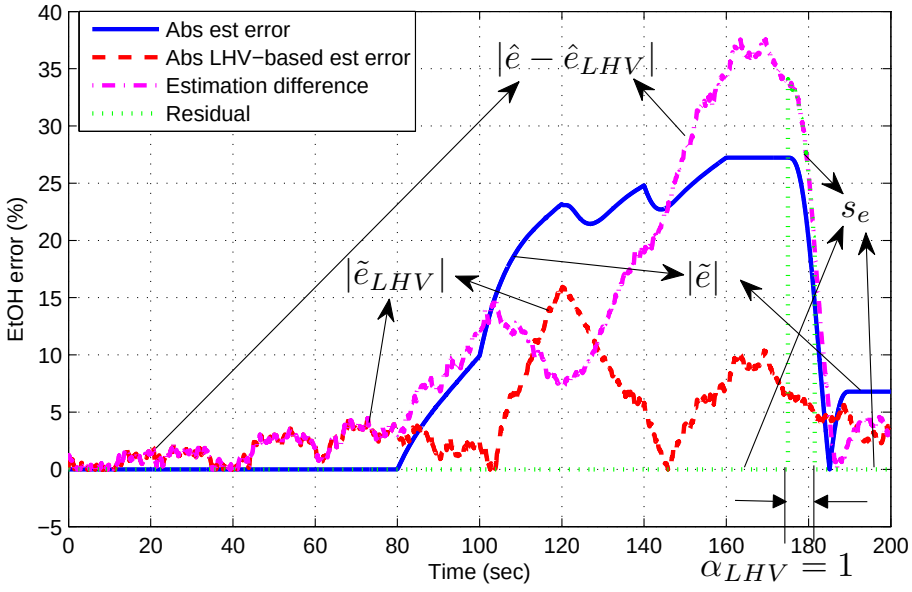

Figure 6.6 Simulated ethanol estimation error and fault detection residual.

problems in addition to engine miscalibration.

Fig. 6.8 shows the simulated detection feature and λ. Although the actual feature $\bar{r}$ in (6.13) from [43] shows large cycle-to-cycle variability, the estimated feature based on the regression model is relatively clean and the variability is filtered out in the LHV-based

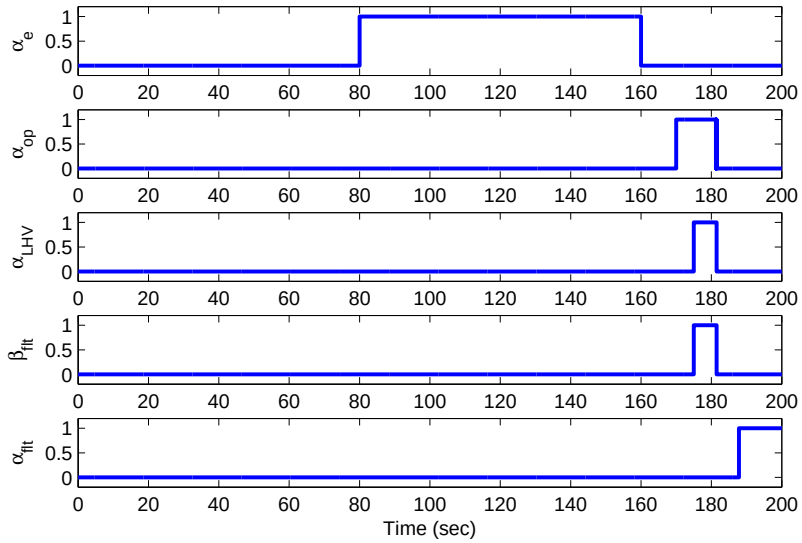

Figure 6.7 Simulated system flags.

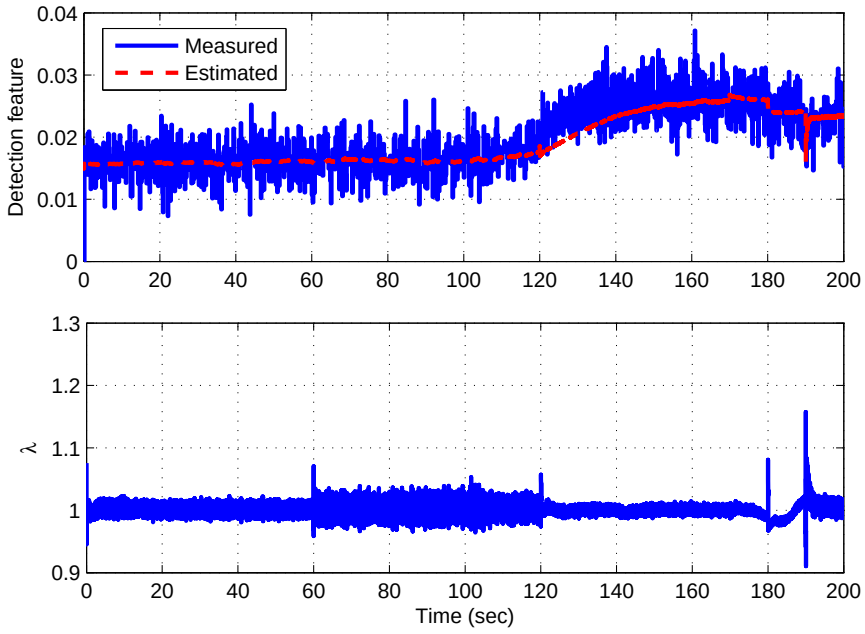

Figure 6.8 Simulated detection feature and RAFR.

ethanol content estimate in Fig. 6.5 as the dynamic or filtered inversion is used as in (6.13). Overall, the RAFR, λ, is well-regulated at unity, i.e., the stoichiometric condition even during the switching periods of the ethanol estimators at the 175th second, followed by the switching to the fuel injector estimation and simultaneous throttle transients. We do not

attempt to paint a rosy picture in this simulation by highlighting the fact that there is a remaining 7% ethanol error and an associated error in the fuel injector drift estimation at the end of the simulated scenario. As it has been highlighted before, the error arises from the mismatch between the model and the observed LHV based ethanol estimation indicated in (6.4) and shown in Fig. 6.1. Note again that the remaining 7% error in the proposed ethanol estimation scheme should be compared to the 28% error observed without the proposed integrated method.

6.6 Experimental Verification

The proposed integrated algorithm was also experimentally validated by an engine dynamometer test.

6.6.1 Experimental Setup

For the experiment, an optimized turbo-charged SIDI VVT flex-fuel engine was used, which is the most updated prototype and different from the engine associated with the previous sections. The detection feature model (6.1) was reparameterized and the residual threshold and other parameters were retuned as well, accordingly. Table 6.3 summarizes the specifications of the optimized engine.

Table 6.3 Specifications for the optimized FFV engine

Description	Value
Engine displacement	2.0 L
Compression Ratio	10.7:1
Fuel pump	HDP5 – 4-lobe cam driven, 1.1 cc/rev
Fuel rail	66 cc, 200 bar
Intake CAM open duration	264 CAdeg

The experimental setup at the engine dynamometer, as illustrated in Fig. 6.9, consists of the latest Bosch MED17.3.2 ECU for engine controls, ETAS ES1000 VME for rapid prototyping, and A&D Redline CAS II System for real-time combustion analysis. The ETAS ES1000 VME rapid prototyping system communicates with the ECU and computer

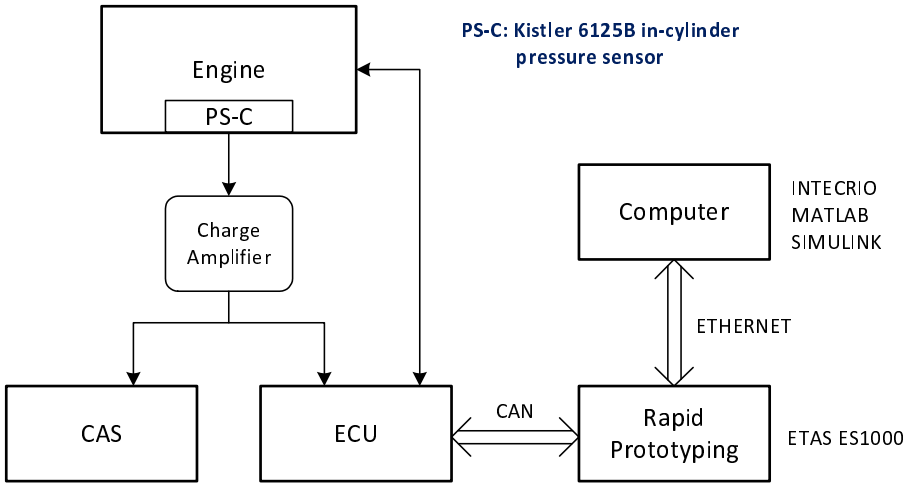

Figure 6.9 Experimental setup at the engine dynamometer.

via CAN and Ethernet respectively.

With the cylinder pressure sensing capability integrated, the Bosch MED17.3.2. ECU is able to acquire the cylinder pressure measurements and conduct real-time calculation of various key combustion features such as the crank angle at 50% mass fraction burn and indicated mean effective pressure. In this study, Kistler 6125B cylinder pressure sensors are installed in each cylinder, whose outputs are converted into voltage signals via an external charge amplifier for the ECU and CAS system.

The rapid prototyping environment in Fig. 6.10 is set up to verify and validate new control and diagnostic functions under target operation conditions on a PC or experimentation system. The proposed virtual prototyping environment includes the following software and hardware components.

- INTECRIO: an open environment that enables the integration of AUTOSAR software components as well as MATLAB®/Simulink® and ASCET models plus C code modules,
- ASCET software components: ASCET-MD for modeling and design, ASCET-SE for software engineering, ASCET-RP for rapid prototyping,
- MATLAB®/Simulink® with Real-Time Workshop® and Embedded Coder,
- ES1000 VME boards and housing: scalable rapid prototyping module that combines real-time calculation power with all relevant ECU bus interfaces, real-time analog and digital I/O to connect sensors and actuators, as well as customizable rapid prototyping boards.

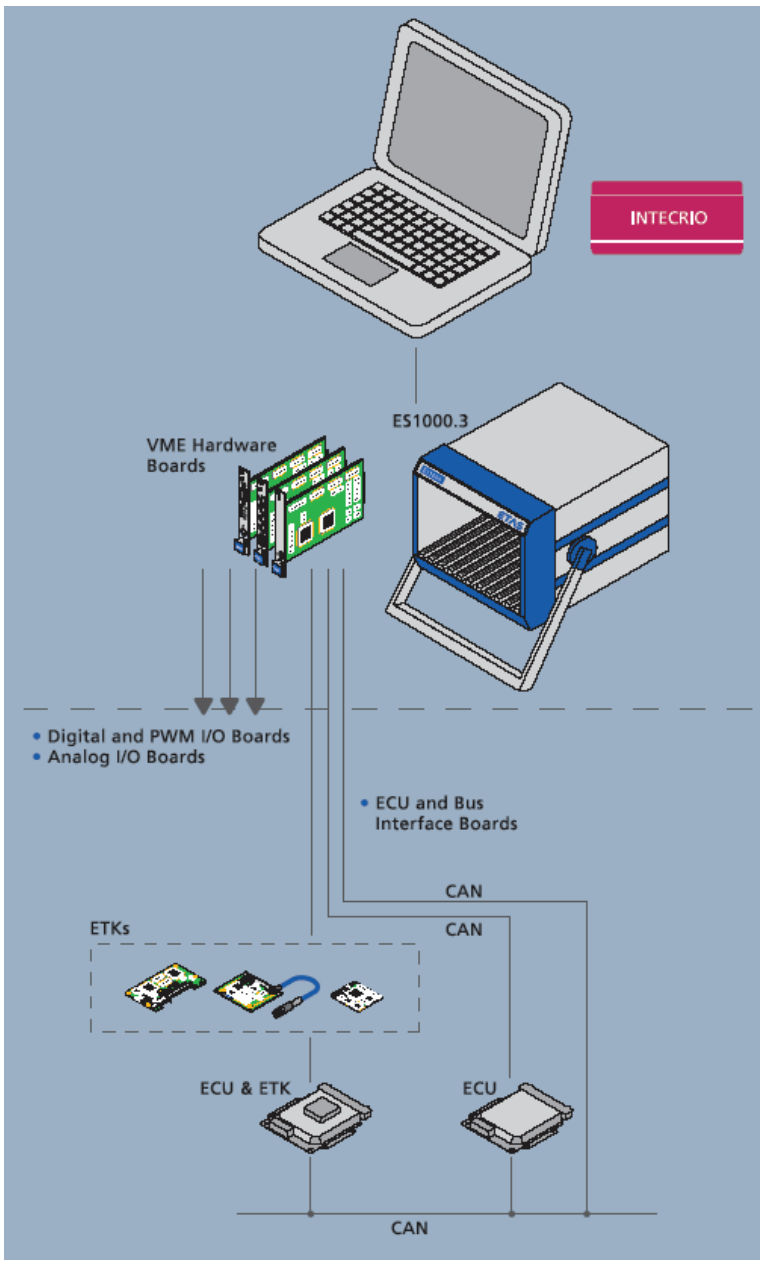

Figure 6.10 Proposed rapid prototyping scheme with ES1000 VME [22].

In the integrated algorithm test, the RAFR controller (6.5)-(6.10) and the ethanol content and injector shift estimator, (6.11) and (6.12), were implemented in the ECU as they are conventional algorithms in FFVs, while the other parts were implemented through the rapid prototyping. The measured LHV detection feature $\bar{r}$ was calculated in the ECU using the in-cylinder pressure measurements and provided to the rapid prototyping for the LHV-based ethanol content estimation (6.13).

6.6.2 Test Results

The actual fuel of E55 was used and the ethanol content estimation based on SAFR was set to E43; the LHV-based estimation was set to E0 at the beginning of the test to show the performance of convergence of each estimation and to emulate the refueling event as shown in the first plot of Fig. 6.11. A 10% fuel injector error was fictitiously introduced at the very beginning of the test to emulate the fuel injector drifts, which would happen with very long time period in real operation. The test was performed at the fixed speed and load, 1500 RPM and 57 kg/hr mass air flow, and no mass air flow sensor error was considered.

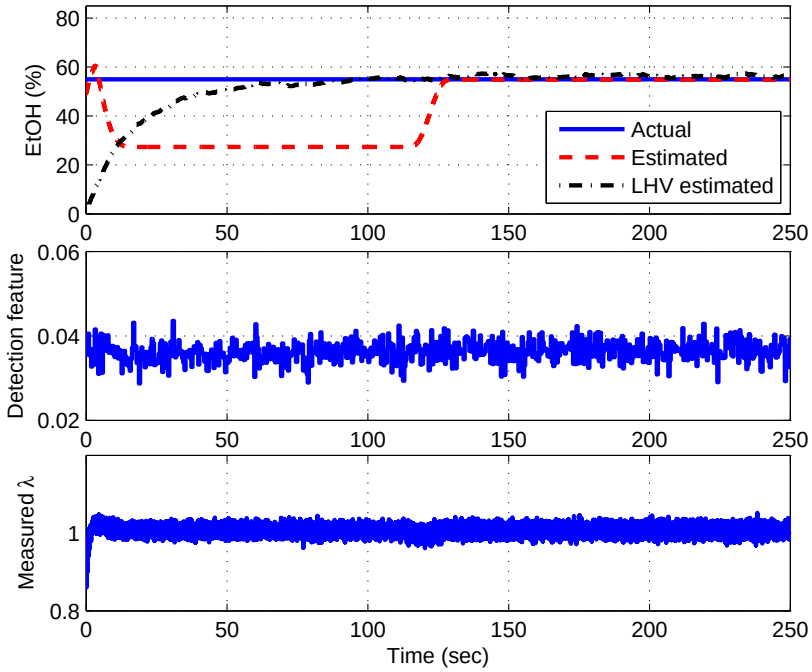

Figure 6.11 Experimental results of the ethanol content estimation and RAFR control.

Fig. 6.11 shows the ethanol content estimation, the measured LHV-based detection feature and the measured λ, and Fig. 6.12 shows the system flags during the test. During the period of the ethanol content estimation ($\alpha_e = 1$), the ethanol estimate deviates from the actual value, 55%, due to the injector error, and it remains fixed before the ethanol estimate reset at around 120th second while the ethanol content estimation is off ($\alpha_e = 0$). The reliability flag α_{LHV} is switched on at around 120th second as $\bar{\alpha}_e$ is switched off at the moment and α_{op} is always on. The flag $\bar{\alpha}_e$ was tuned to switch off with $t_e = 100$ sec as the LHV-based estimation was much slower than the SAFR-based estimation to filter out the cycle-to-cycle variability in the measured detection feature in the second plot of

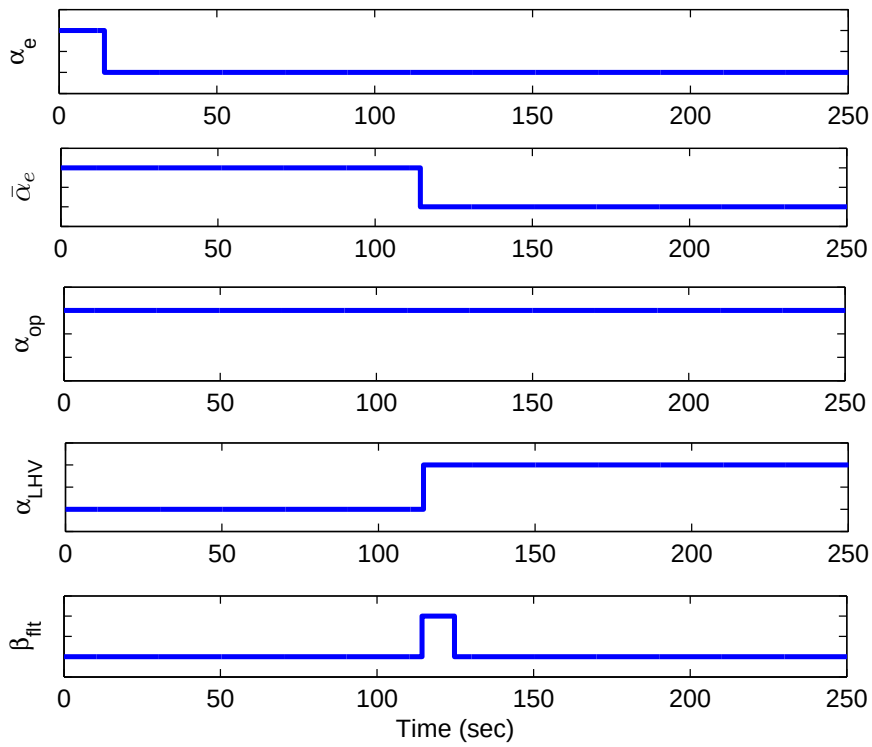

Figure 6.12 System flags during the experiment of the integrated algorithm.

Fig. 6.11. The fault trigger β_{flt} is triggered at around the 120th sec as α_{LHV} is switched on and the difference between the ethanol content estimate and the LHV-based ethanol content estimate is quite large at that moment. The resetting of the ethanol estimate is performed during 120-130 seconds starting with the trigger of β_{flt} with the quintic polynomial profile in time. The measured λ in the third plot of Fig. 6.11 is well-regulated at the stoichiometric condition as the feedforward control is smooth with the smooth transition of the ethanol content prediction.

6.7 Conclusion

In this chapter, a robust methodology for estimating fuel ethanol content in a flex-fuel SIDI engine under fuel injector drifts is proposed. The LHV-based ethanol detection feature, indicating the charge cooling effects of the fuel injected during the compression stroke, is calculated using the differences in cylinder pressure measurements under single and split injection modes. The proposed approach enables the use of the LHV-based detection feature in an appropriate confined operation regime where strict monotonicity with the ethanol

content is observed. A large difference between the ethanol estimation and the LHV-based ethanol estimation is monitored. This difference is used to correct estimation errors and to trigger an injector fault detection flag. Criteria for setting the residual threshold and assessing the reliability of the LHV-based estimation to trigger the resetting event are developed as well. Verification of the algorithm and the fault detection performance are demonstrated both by simulation with a validated engine model under a simplified operating scenario with fuel injector drifts and by a dynamometer test in which the algorithm is implemented in the engine control unit (ECU) and the rapid prototyping.

Chapter 7
Conclusions and Future Work

7.1 Conclusions

This section summarizes the work completed in this research.

Chapter 2 presented a simple AFR-based ethanol estimation law using the exhaust gas oxygen sensor and the closed-loop AFR regulation of SI engines. The characteristics of the algorithm including sensitivity were quantified via simulations. Two main issues in the ethanol content estimation were then elucidated:

1. Transient AFR response constrains the ethanol content estimation gain, resulting in slow adaptation.
2. The AFR-based ethanol content estimation is very sensitive to mass air flow sensor error and/or fuel injection error.

In chapter 3, we introduced a fuel puddle model of a gasoline-ethanol blended fuel for PFI engines in FFVs. The model is utilized to design a transient fuel compensator which eliminates transient AFR excursions caused by throttle modulation and in turn enables fast fuel adaptation. The model is divided into two parts: a droplet evaporation model to generate the wall-impacting portion of the injected fuel and a single puddle vaporization model. To capture the characteristics of the physical vaporization process, a multi-component fuel model parameterized by the ethanol content is utilized. To verify the validity of the model, model simulation results were compared with the experimental data provided in [10] for E0, E22 and E85.

In chapter 4, a transient fuel compensator using the proposed fuel puddle model was formulated. An appropriate approximation was used to invert the nonlinear model and design a TFC accordingly. The approximation was demonstrated with a TFC simulation. The transient fuel compensator realizes better AFR control since faster control action is obtained by the feedforward command which cancels the fuel puddle dynamics. Consequently, faster ethanol content estimation is also realized since ethanol estimator gain could be increased.

The increase is possible because the TFC reduces transient λ responses caused by throttle change. This performance enhancement in AFR control and ethanol estimation was demonstrated by simulations. Robustness in AFR control and ethanol content estimation was also demonstrated by simulation with the model error in the fuel puddle observer used in TFC.

In chapter 5, we formulated a cylinder air flow estimation scheme which is redundant to MAF-based estimation. The scheme is able to compensate for the MAF sensor drifts through the use of manifold absolute pressure (MAP) measurements. More reliable ethanol content estimation is realized because cylinder air flow estimation is enhanced via the MAF-MAP fused cylinder air flow estimation.

In chapter 6, we presented an ethanol estimation scheme which is robust to fuel injector drifts in direct injection engines and is based on the cylinder charge cooling during high ethanol contents. To achieve robust ethanol content estimation, the LHV-based detection feature quantified by in-cylinder pressure measurements under specially designed fuel injection sequences was used together with the conventional SAFR-based method. The integrated estimation algorithm is validated both by simulation and an engine dynamometer test with the algorithm implemented in the engine control unit (ECU) and the rapid prototyping.

7.2 Future Work

In this section we propose potential future directions related to the work completed in this dissertation. The LHV-based ethanol content estimation in chapter 6 utilizes a regression model of the experimentally obtained detection feature data calculated by in-cylinder pressure measurements. The data were collected at certain chosen settings of injection, valve and spark timings. It is not clear how a broader range of timings may affect in-cylinder pressures during cylinder charge cooling processes and hence detection features. Therefore, to thoroughly understand the charge cooling processes associated with different operating conditions and fuel ethanol contents, it is desirable to develop a physics-based model. A physics-based model may lead to optimal settings of injection, valve and spark timings for ethanol detection purposes. Such a model could also reduce calibration efforts in wide operating conditions. Although rigorous efforts to model the charge cooling processes based on physics principles were presented in [44], the model could not be fully validated. Difficulties in modeling the charge cooling processes arise from the lack of information on internal states other than in-cylinder pressure measurements while the pressure drop cor-

responding to charge cooling is a relatively tiny phenomenon compared with in-cylinder pressure changes caused by engine strokes and heat exchange processes through walls. Therefore, experiments are needed to quantify certain states associated with fuel spray vaporization and potential wall wetting and puddle vaporization during the charge cooling. Such experiments would allow investigation of the cylinder charge cooling processes in detail and consequently lead to the development of a physics-based model.

Even though ethanol has generally received the most attention among biofuels in the United States, there are other renewable alternative fuels under consideration: bioalcohols such as methanol and butanol, hydrogen and (non-fossil) natural gas. Developing a fuel adaptation methodology that can account for various impacts of the fuel properties of other non-fossil fuels and consequently obtain the optimal vehicle performance should be a valuable work.

There are research efforts in identifying fuel compositions in biodiesel applications to realize clean and efficient utilization of fuels [52, 53]. Thus, potential future work could be to extend the methodology developed in our research to the biodiesel applications. Since lean combustion takes place in normal operating conditions of diesel-biodiesel engines, EGO measurements should be utilized in a manner different from our method as in [52, 53] and the charge cooling features should account for different operating conditions and fuel properties.

Finally, another potential research area is control of a dual fuel engine. Dual fuel injection (DI and PFI) SI engines were introduced to improve engine performance at high load and speed. Combustion characteristics of a dual fuel injection SI engine under different combinations of DI and PFI with gasoline and ethanol are presented in [65]. The concept of a dual fuel highly efficient internal combustion engine is presented in [46]. In the dual fuel mixed ignition engine, the spark ignition mode is used at lower loads with ethanol injection, while the compression ignition mode is used at higher and full loads with injection of diesel and ethanol. This strategy offers an opportunity to improve the thermal efficiency of an engine for lower loads and to more effectively control engine combustion better than is possible for dual fueling of a compression ignition engine. The dual fuel mixed ignition engine could also be used at very low temperatures due to its easy start in the SI mode. To practically realize this idea, many control problems should be resolved such as control of injection timing and pressure, operation of the turbocharger, EGR valve, and ignition timing for the SI mode.

Appendices

Appendix A

LHV-Based Ethanol Detection Feature

This appendix provides supplementary information on calculation of the LHV-based ethanol detection feature, r, introduced in section 6.1, and experimental data used in section 6.2.

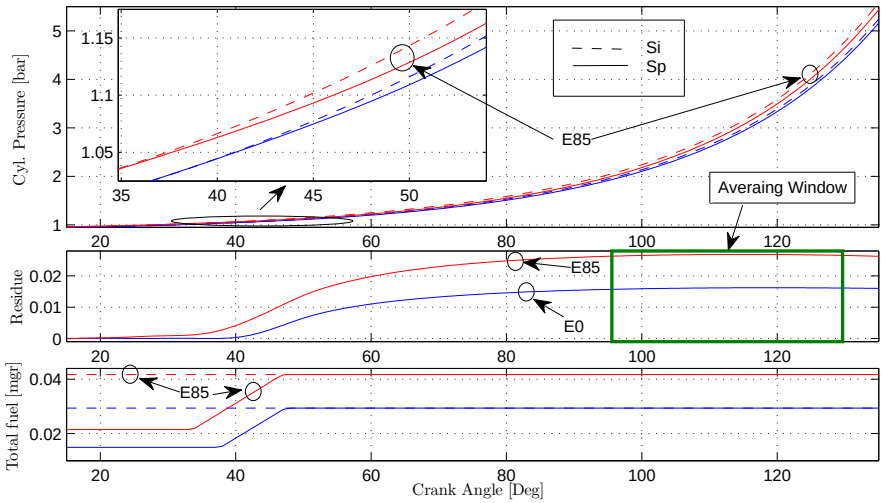

Figure A.1 Cylinder pressure and residue evolutions during the compression stroke. (2 consecutive engine cycles regarded as 1 synchronized cycle)

Fig. A.1 shows the cylinder pressure evolutions during the compression stroke under Si and Sp injection modes. The third plot in Fig. A.1 shows the total amount of injected fuel, where it increases at around 40 CADeg under the Sp mode as half of the stoichiometric amount is injected after all the valves are closed. By the charge cooling effect, the cylinder pressures under the Sp mode are lower than those under the Si mode for the same engine operating conditions. This pressure drop is quantified by the following residue at an instance:

$$Rsd(k) = \ln(p_0^{Si}(k)/p_0^{Sp}(k)), \tag{A.1}$$

where p_0^{Si}, p_0^{Sp} are corrected cylinder pressures [43] under Si and Sp injection modes, and k denotes a step in time or crank angle. Even though the cylinder pressures under different modes are obtained in different cycles, we regard them as synchronized quantities in time. The second plot in Fig. A.1 shows the evolution of the residue, *Rsd*, which quantifies the pressure gap under different injection modes appeared in the first plot. Finally, the LHV-based detection feature, r, is obtained by averaging *Rsd* over the interval of several steps near the end of compression where the instantaneous residue is usually maximized corresponding to the rectangle in the second plot in Fig. A.1:

$$r = \frac{\sum_{k=k_1}^{k_2} Rsd(k)}{k_2 - k_1 + 1}. \tag{A.2}$$

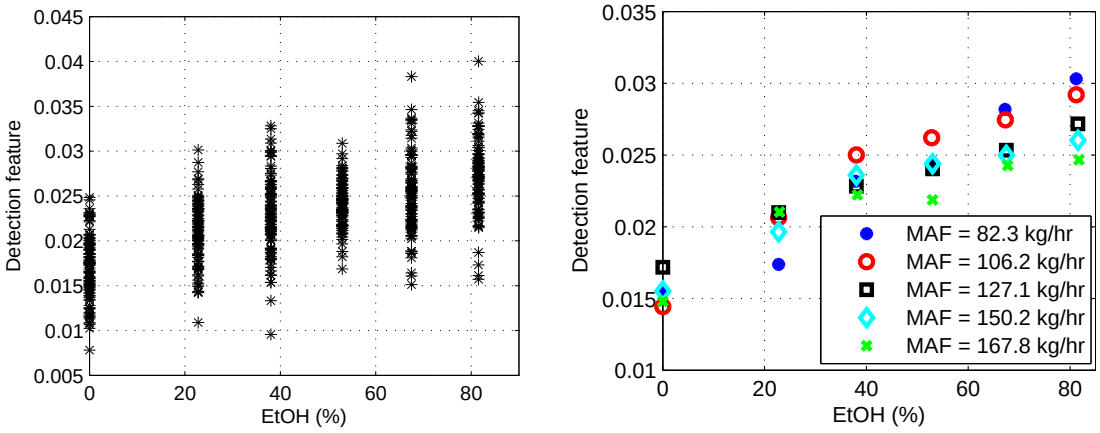

(a) raw data for averaged MAF 127.1 kg/hr

(b) averaged data

Figure A.2 Experimental data obtained at the engine speed of 2500 RPM.

Fig. A.2 shows the LHV-based detection feature data at the engine speed of 2500 RPM from the experiments described in section 6.2. The detection features in Fig. A.2(a) obtained at mass air flow of 127.1 kg/hr are raw data corresponding to the calculation (A.2) which shows high cycle-to-cycle variability, while those in Fig. A.2(b) are averaged data which are regarded as steady-state values and used for the regression (6.1). The high cycle-to-cycle variability in Fig. A.2(a) is filtered online via the estimator (6.13) and delays reaching the steady state in Fig. A.2(b). Indeed, the operating condition history examiner (6.16) takes account for the delay from the filtering and the tuning of t_{LHV} in (6.16) relies on the estimator gain tuning of L_{LHV} in (6.13).

Appendix B
Variables and Parameters

Some variables in Table B.1 have multiple definitions throughout this dissertation. Each definition is clarified in each corresponding section for such variables.

Table B.1 List of all parameters and their values, if constant

Parameter	Definition	Value (if constant)
α_e	flag for switching on ethanol adaptation	
α_{flt}	fuel injector fault flag	
α_{LHV}	LHV-based estimation reliability flag	
α_{op}	flag on operating condition check	
α_s	switching signal on MAF sensor drift adaptation	
β_{flt}	fault trigger	
γ	tuning constant in droplet evaporation model	0.80
γ_e	stoichiometric air-to-fuel ratio estimation gain, kg^{-1}	
δ_{th}	fuel film thickness, m	3.0×10^{-3}
ε_{AFR_s}	estimation error in stoichiometric air-to-fuel ratio	
η_d	tuning constant in droplet evaporation model	0.31
η_p	tuning constant in single puddle vaporization model	0.75
η_v	volumetric efficiency	
θ	throttle angle, deg	
λ	ratio of actual AFR to stoichiometric AFR	
ν_A	kinematic viscosity of air, m^2/s	
ρ	density of fuel mixture, kg/m^3	
ρ_A	density of air, kg/m^3	
ρ_{eth}	density of ethanol, kg/m^3	789
ρ_{gsl}	density of gasoline, kg/m^3	747
σ	tuning constant in single puddle vaporization model	0.60

Parameter	Definition	Value (if constant)
τ	vaporization time constant of fuel puddle, sec	0.3
τ_d	transport and induction-to-power delay, sec	0.2
τ_{DA}	time constant of airborne droplet number decay, sec	8.0×10^{-5}
τ_{MAF}	MAF sensor time constant, sec	
τ_{PI}	PI control gain, sec	
τ_s	time constant of the exhaust gas oxygen sensor lag, sec	0.07
AFR	air-to-fuel ratio	
AFR_s	stoichiometric air-to-fuel ratio	
B_d	transfer number in droplet evaporation model	
B_p	transfer number in single puddle vaporization model	
C	correction factor in single puddle vaporization model	
D	diffusion coefficient, m^2/s	
d_d	droplet diameter, m	
d_d^0	initial droplet diameter, m	6.0×10^{-5}
d_{in}	port diameter, m	0.045
D_p	diffusion coefficient in single puddle vaporization model, m^2/s	
e	ethanol volume fraction in gasoline-ethanol fuel blend	
ECT	engine coolant temperature, K	
ECT^0	tuning constant for apparent temperature, K	290
e_m	ethanol mass fraction in gasoline-ethanol fuel blend	
e_{thld}	ethanol content estimation residual threshold	
$f_{d,i}$	mass fraction of a fuel component in a droplet	
f_{ea}	MAF sensor error fraction	
f_{ef}	fuel injection error fraction	
$f_{g,i}$	mass fraction of a fuel component in gasoline	
f_i	mass fraction of a fuel component in gasoline-ethanol fuel blend	
$f_{p,i}$	mass fraction of a fuel component in fuel puddle at IVO	
k_{PI}	PI control gain, kg/s^2	
L_e	ethanol content estimator gain, kg^{-1}	
L_{inj}	fuel injector shift estimator gain, kg^{-1}	
l_p	approximated conditional probability	
MAF	mass air flow, kg/s,	
M_{air}	molecular weight of air, g/mol	28.97

Parameter	Definition	Value (if constant)
m_{air}	cylinder air charge, kg	
m_{fb}	feedback fuel injection, kg	
$m_{f,cyl}$	cylinder fuel charge, kg	
m_{ff}	feedforward fuel injection, kg	
M_i	molecular weight of a fuel component, g/mol	
m_{inj}	fuel injection, kg	
N	engine rotation speed, RPM	
p_m	intake manifold absolute pressure, bar	
PP_{air}	partial pressure of air, bar	
r	LHV-based ethanol detection feature	
R	gas constant, kJ/kg K	
r_s	LHV-based ethanol detection feature at stoichiometry	
Re	Reynolds number	
Rsd	instantaneous LHV-based ethanol detection residue	
Sc	Schmidt number	
Sh	Sherwood number	
T_{app}	apparent temperature, K	
T_m	manifold temperature, K	
V_d	total displace cylinder volume, m^3	
V_m	intake manifold volume, m^3	
VP_i	normal vapor pressure of a fuel component, bar	
W_θ	air flow rate through the throttle, kg/s	
W_a	air flow rate or load, kg/hr	
$W_{a,cyl}$	cylinder air flow, kg/s	
W_f	cylinder fuel flow, kg/s	
W_{fb}	feedback fuel injection rate, kg/s	
W_{ff}	feedforward fuel injection rate, kg/s	
W_{ff1}	uncompensated feedforward fuel injection rate, kg/s	
W_{inj}	fuel injection rate, kg/s	
X	wall impacting factor of injected fuel	
X_i	wall impacting factor of a fuel component from injected fuel	

Bibliography

[1] A. K. Agarwal, "Biofuels (alcohols and biodiesel) applications as fuels for internal combustion engines," *Progress in Energy and Combustion Science*, vol. 33, pp. 233–271, 2007.

[2] K. Ahn, A. G. Stefanopoulou, and M. Jankovic, "Estimation of ethanol content in flex-fuel vehicles using an exhaust gas oxygen sensor: Model, tuning and sensitivity," in *ASME 1st Annual Dynamic Systems and Control Conference*, Ann Arbor, Michigan, USA, Oct. 20–22, 2008.

[3] K. Ahn, A. G. Stefanopoulou, and M. Jankovic, "Fuel puddle model and AFR compensator for gasoline-ethanol blends in flex-fuel engines," in *Proceedings of IEEE Vehicle Power and Propulsion (VPP) Conference*, Dearborn, Michigan, USA, Sep. 7–11, 2009.

[4] K. Ahn, A. G. Stefanopoulou, and M. Jankovic, "Tolerant ethanol estimation in flex-fuel vehicles during MAF sensor drifts," in *Proceedings of ASME 2nd Annual Dynamic Systems and Control Conference*, Hollywood, California, USA, Oct. 12–14, 2009.

[5] K. Ahn, A. G. Stefanopoulou, and M. Jankovic, "Puddle dynamics and air-to-fuel ratio comensation for gasoline-ethanol blends in flex-fuel engines," *IEEE Trans. Control Syst. Technol.*, vol. 18, no. 6, pp. 1241–1253, 2010.

[6] K. Ahn, A. G. Stefanopoulou, L. Jiang, and H. Yilmaz, "Ethanol content estimation in flex fuel direct injection engines using in-cylinder pressure measurements," *SAE paper 2010-01-0166*.

[7] K. Ahn, A. G. Stefanopoulou, L. Jiang, and H. Yilmaz, "Ethanol content estimation in flex fuel direct injection engines with fault detection under fuel injector drifts," in *Proceedings of IFAC Symposium Advances in Automotive Control (AAC)*, Munich, Germany, Jul. 12–14, 2010.

[8] C. F. Aquino, "Transient a/f control characteristics of the 5 liter central fuel injection engine," *SAE paper 810494*.

[9] J. Barata, "Modeling of biofuel droplets dispersion and evaporation," *Renewable Energy*, vol. 33, pp. 769–779, 2008.

[10] J. J. Batteh and E. W. Curtis, "Modeling transient fuel effects with alternative fuels," *SAE paper 2005-01-1127*.

[11] J. J. Batteh, E. W. Curtis, and M. Fried, "Analytical assessment of simplified transient fuel tests for vehicle transient fuel compensation," *SAE paper 2005-01-3894*.

[12] *HFM2-Air Mass Meter*, Bosch.

[13] *MAP Sensor Technical Specifications*, Bosch.

[14] *Automotive Handbook*, 5th ed., Bosch, 2000.

[15] N. D. Brinkman, "Ethanol fuel – a single-cylinder engine study of efficiency and exhaust emissions," *SAE paper 810345*.

[16] L. Bromberg, D. R. Cohn, and J. B. Heywood, "Optimized fuel management system for direct injection ethanol enhancement of gasoline engines," U.S. Patent 7 225 787 B2, Jun. 5, 2007.

[17] J. S. Cowart, W. E. Boruta, J. D. Dalton, R. F. Dona, F. L. Rivard II, R. S. Furby, J. A. Piontkowski, R. E. Seiter, and R. M. Takai, "Powertrain development of the 1996 Ford flexible fuel Taurus," *SAE paper 952751*.

[18] P. R. Crossley and J. A. Cook, "A nonlinear engine model for drivetrain system development," *IEE International Conference, Control '91*, vol. 2, pp. 921–925, Mar. 1991.

[19] E. W. Curtis, C. F. Aquino, D. K. Trumpy, and G. C. Davis, "A new port and cylinder wall wetting model to predict transient air/fuel excursions in a port fuel injected engines," *SAE paper 961186*.

[20] E. W. Curtis, S. Russ, C. Aquino, G. Lavoie, and N. Trigui, "The effects of injector targetting and fuel volatility on fuel dynamics in a PFI engine during warm-up," *SAE paper 982519*.

[21] R. C. Delgado, A. S. Araujo, and V. J. Fernandes Jr., "Properties of brazilian gasoline mixed with hydrated ethanol for flex-fuel technology," *Fuel Processing Technology*, vol. 88, no. 4, pp. 365–368, 2007.

[22] *Manual for INTECRIO*, ETAS, Inc.

[23] M. A. Franchek, P. J. Buehler, and I. Makki, "Intake air path diagnostics for internal combustion engines," *J. Dyn. Sys., Meas., Control*, vol. 129, pp. 32–40.

[24] R. L. Furey, "Volatility characteristics of gasoline-alcohol and gasoline-ether fuel blends," *SAE paper 852116*.

[25] R. L. Furey and K. L. Perry, "Vapor pressures of mixtures of gasolines and gasoline-alcohol blends," *SAE paper 861557*.

[26] M. L. Greenfield, G. A. Lavoie, C. S. Smith, and E. W. Curtis, "Macroscopic model of the D86 fuel volatility procedure," *SAE paper 982724*.

[27] J. Grizzle, J. Cook, and W. Milam, "Improved cylinder air charge estimation for transient air fuel ratio control," *American Control Conference, 1994*, vol. 2, pp. 1568–1573, 1994.

[28] L. Guzzella and C. H. Onder, *Introduction to Modeling and Control of Internal Combustion Engine Systems*. Springer, 2004.

[29] F. P. Incropera and D. P. DeWitt, *Fundamentals of Heat and Mass Transfer*, 5th ed. John Wiley & Sons, 2002.

[30] R. Isermann, "Process fault detection based on modeling and estimation methods–a survey," *Automatica*, vol. 20, no. 4, pp. 387 – 404, 1984.

[31] R. Isermann, "Model-based fault-detection and diagnosis - status and applications," *Annual Reviews in Control*, vol. 29, no. 1, pp. 71 – 85, 2005.

[32] M. Jankovic, S. Magner, D. Hagner, and Y. Wang, "Multi-input transient fuel control with auto-calibration," in *Proceedings of the 2007 American Control Conference*.

[33] L. Jiang, H. Yilmaz, M. Christie, K. Ahn, and A. Stefanopoulou, "Optimally controlled flexible fuel vehicle," in *10th Stuttgart International Symposium*, 2010.

[34] L. Jiang, J. Vanier, H. Yilmaz, and A. Stefanopoulou, "Parameterization and simulation for a turbocharged spark ignition direct injection engine with variable valve timing," *SAE paper 2009-01-0680*, 2009.

[35] K. Kar, T. Last, C. Haywood, and R. Raine, "Measurement of vapor pressures and enthalpies of vaporization of gasoline and ethanol blends and their effects on mixture preparation in an SI engines," *SAE paper 2008-01-0317*.

[36] Y.-W. Kim, G. Rizzoni, and V. I. Utkin, "Developing a fault tolerant power-train control system by integrating design of control and diagnostics," *Int. J. Robust Nonlinear Control*, vol. 11, pp. 1095–1114.

[37] S. Leonhardt, N. Müller, and R. Isermann, "Methods for engine supervision and control based on cylinder pressure information," *IEEE/ASME Transactions on Mechatronics*, vol. 4, no. 3, pp. 235 –245, Sep. 1999.

[38] M. Locatelli, C. H. Onder, and H. P. Geering, "An easily tunable wall-wetting model for PFI engines," *SAE paper 2004-01-1461*.

[39] M. Locatelli, E. Alfieri, C. H. Onder, and H. P. Geering, "Identification of the relevant parameters of the wall-wetting system by extended Kalman filtering," *Control Engineering Practice*, vol. 14, no. 3, pp. 235–241, 2006.

[40] P. J. Maloney, "An event-based transient fuel compensator with physically based parameters," *SAE paper 1999-01-0553*.

[41] H. Melgaard, E. Hendricks, and H. Madsen, "Continuous identification of a four-stroke SI engine," in *Proceedings of the 1990 American Control Conference*, May 1990, pp. 1876–1881.

[42] K. Nakata, S. Utsumi, A. Ota, K. Kawatake, T. Kawai, and T. Tsunooka, "The effect of ethanol fuel on a spark ignition engine," *SAE paper 2006-01-3380*.

[43] N. Oliverio, A. Stefanopoulou, L. Jiang, and H. Yilmaz, "Ethanol detection in flex-fuel direct injection engines using in-cylinder pressure measurements," *SAE paper 2009-01-0657*.

[44] N. H. Oliverio, L. Jiang, H. Yilmaz, and A. G. Stefanopoulou, "Modeling the effect of fuel ethanol concentration on cylinder pressure evolution in direct-injection flex-fuel engines," in *Proceedings of the 2009 American Control Conference*, 2009.

[45] Orbital Engine Co., "A literature review based assessment on the impacts of a 20% ethanol gasoline fuel blend on the Australian vehicle fleet," *Report to Environment Australia*, Nov. 2002.

[46] G. Pawlak, "The concept of a dual fuel highly efficient internal combustion engine," *SAE paper 2010-01-1480*.

[47] J. O. Ramsay, "Estimating smooth monotone functions," *Journal of the Royal Statistical Society. Series B*, vol. 60, no. 2, pp. 365 – 375, 1998.

[48] M. S. Rocha and J. R. Simões-Moreira, "A simple impedance method for determining ethanol and regular gasoline mixtures mass contents," *Fuel*, vol. 84, pp. 447–452, 2005.

[49] M. C. Sellnau, F. A. Matekunas, P. A. Battiston, C.-F. Chang, and D. R. Lancaster, "Cylinder-pressure-based engine control using pressure-ratio-management and low-cost non-intrusive cylinder pressure sensors," *SAE paper 2000-01-0932*.

[50] J. Senda, T. Higaki, Y. Sagane, H. Fujimoto, Y. Takagi, and M. Adachi, "Modeling and measurement on evaporation process of multicomponent fuels," *SAE paper 2000-01-0280*.

[51] W. A. Sirignano, *Fluid Dynamics and Transport of Droplets and Sprays*. Cambridge University Press, 1999.

[52] D. B. Snyder, G. H. Adi, M. P. Bunce, C. A. Satkoski, and G. M. Shaver, "Steady-state biodiesel blend estimation via a wideband oxygen sensor," *Journal of Dynamic Systems, Measurement, and Control*, vol. 131, no. 4, p. 041012, 2009.

[53] D. B. Snyder, G. H. Adi, M. P. Bunce, C. A. Satkoski, and G. M. Shaver, "Fuel blend fraction estimation for fuel-flexible combustion control: Uncertainty analysis," *Control Engineering Practice*, vol. 18, no. 4, pp. 418 – 432, 2010.

[54] J. S. Souder and J. K. Hedrick, "Adaptive sliding mode control of air-fuel ratio in internal combustion engines," *International Journal of Robust and Nonlinear Control*, vol. 14, no. 6, pp. 525–541, 2004.

[55] D. B. Spalding, *Combustion and Mass Transfer*. London: Pergamon Press, 1979.

[56] A. Stodart, J. Maher, L. Greger, and J. Carlsson, "Fuel system development to improve cold start performance of a flexible fuel vehicle," *SAE paper 982532*.

[57] A. Stotsky and I. Kolmanovsky, "Application of input estimation techniques to charge estimation and control in automotive engines," *Control Engineering Practice*, vol. 10, no. 12, pp. 1371 – 1383, 2002.

[58] C. F. Taylor, *Internal Combustion Engine in Theory and Practice*. The MIT Press, 1985, vol. 2, revised edition.

[59] F. Theunissen, "Percent ethanol estimation on sensorless multi-fuel systems; advantages and limitations," *SAE paper 2003-01-3562*.

[60] S. Tonini, M. Gavaises, C. Arcoumanis, A. Theodorakakos, and S. Kometani, "Multi-component fuel vaporization modelling and its effect on spray development in gasoline direct injection engines," *Proc. IMechE*, vol. 221, pp. 1321–1342, 2007.

[61] R. E. Treybal, *Mass-Transfer Operations*, 3rd ed. McGraw-Hill, 1980.

[62] S. S. Wang, Y. Lin, N. H. Resendiz, L. E. Granados, and H. H. Rodriguez, "Ethanol concentration sensor," *SAE paper 2008-01-2452*.

[63] G. F. Yao, S. I. Abdel-Khalik, and S. M. Ghiaasiaan, "An investigation of simple evaporation models used in spray simulations," *Journal of Heat Transfer*, vol. 125, no. 1, pp. 179–182, 2003.

[64] C. L. Yaws, *Yaws' Handbook of Thermodynamic and Physical Properties of Chemical Compounds*. Knover, 2003.

[65] G. Zhu, T. Stuecken, H. Schock, X. Yang, D. L. S. Hung, and A. Fedewa, "Combustion characteristics of a single-cylinder engine equipped with gasoline and ethanol dual-fuel systems," *SAE paper 2008-01-1767*.

[66] G. G. Zhu, C. F. Daniels, and J. Winkelman, "MBT timing detection and its closed-loop control using in-cylinder pressure signal," *SAE paper 2003-01-3266*.